RESEARCH REPORT

NO VTT-R-01028-09| 15.4.2009

SAFIR2010 SUSI and IMPACT projects

IMPACT Tests: Test Facilities and Application Methods, Part 2

Authors: Kim Calonius (VTT), Ilkka Hakola (VTT), Juha Kuutti (VTT), Hannu Martikainen (VTT), Arja Saarenheimo (VTT), Markku Tuomala (TUT)

Confidentiality: Public

Report's title	
IMPACT Tests: Test Facilities and Application Methods, Part 2	
Customer, contact person, address SAFIR2010 VYR, Jorma Aurela (TEM)	Order reference
Project name Structures under Soft Impact (SUSI)	Project number/Short name 22797
Author(s) Kim Calonius, Ilkka Hakola, Juha Kuutti, Hannu Martikainen, Arja Saarenheimo, Markku Tuomala	Pages 107/
Keywords impact test, missile, reinforced concrete wall, simulation, FEM	Report identification code VTT-R-01028-09

Summary

The IMPACT testing facility has been built to investigate the impact of deformable missiles on concrete structures (Lastunen et al., 2007). The test facility is designed for medium scale tests. The maximum missile weight is 50 to 100 kg depending on the missile velocity which is in the range of 100 to 200 m/s. The IMPACT project is mainly concentrated on the research of soft missile impacts on concrete walls, but several tests have also been carried out using hard steel missiles. The main purpose of the project is to produce data for verifying and developing numerical models and methods. The theoretical work has been carried out within the SUSI project (Calonius et al, 2008) (Saarenheimo et al, 2007) (Saarenheimo et al, 2006).

Post analyses for IMPACT tests of 15 cm thick reinforced concrete walls are reported. Numerical studies are carried out with finite element method using shell elements and also with simplified two degrees of freedom models. Due to uncertainties in measuring the force-time functions for impacting missiles, load functions for analyses are calculated using the Riera method (Riera, 1968) and they are adjusted according to the experimental findings. Parameters for material models used in analyses are based on the available material test data. Basically, all the analyses are carried out using comparable input data. Additionally, some sensitivity studies are carried out and test results are compared with results of different methods.

The numerical modelling of prestressed concrete walls is studied on a general level. Different ways to model the prestressing, especially concerning the finite element method, are demonstrated.

Confidentiality	Public

Espoo 15.4.2009

Signatures	Signatures	Signatures
Written by Kim Calonius Research Scientist	Reviewed by Ari Vepsä Research Scientist	Accepted by Eila Lehmus Technology Manager

VTT Technical Research Centre of Finland
P.O.Box 1000, FI-02044 VTT, Finland

Distribution (customer and VTT)
SAFIR2010 Reference Group 7
SUSI-IMPACT Ad Hoc Group

Preface

This study is a part of the SUSI (Structures under Soft Impact) project carried out in the SAFIR2010 Programme, the Finnish Research Programme on Nuclear Power Plant Safety 2007-2010. This study is funded by the state Nuclear Waste Management Fund (VYR) and Technical Research Centre of Finland (VTT). The interest and contribution of the Ad Hoc group is greatly acknowledged. The contact person in STUK is Mr Pekka Välikangas.

Espoo 15.4.2009

Authors

Contents

1 Introduction

In order to obtain reliable numerical results, the methods and models should be verified against experimental data. The accuracy and capability of numerical methods used in analysing reinforced concrete structures under soft missile impacts are discussed in this report. The test results used in this study are recorded within the IMPACT project. All the calculation work presented is performed within the SUSI project. This report is continuation of a previous report (Calonius et al., 2008). This time, the liquid dispersal and the fire simulation are reported separately.

A flexible experimental platform for intermediate scale impact tests was created and taken in use in 2003 at VTT. The test facilities have been further developed and improved since then. These new facilities are described in this report. Furthermore, all the sensor types that have been used in IMPACT tests are listed and briefly explained.

Post analyses for impact tests of one-way 15 cm thick reinforced concrete walls are reported. Numerical studies were carried out with finite element code Abaqus using shell elements and with simplified two degrees of freedom models. Some numerical simulations were carried out also using another finite element code called LS-DYNA (LS-DYNA, 2003). Due to uncertainties in measuring the force-time functions for impacting missiles, load functions needed in analyses were calculated by using the Riera method (Riera, 1968) and adjusted according to the experimental findings. Parameters for material models used in the analyses are based on the available material test data.

Additionally, some sensitivity studies were conducted by varying the loading function. Sensitivity studies carried out on material parameters and mesh density have been reported earlier (Saarenheimo et al., 2007).

Some results of the one-way slab tests and corresponding analyses with different methods are summarised and compared with each other.

The numerical modelling of prestressed concrete walls is studied on a general level. Different ways to model the prestressing, especially with finite element method, are explained. The tests with two-way 25 cm thick prestressed concrete walls conducted in IMPACT project are not reported. However, the Dywidag type of prestressing with rigid bars that was used in those tests is reviewed. Also, some preliminary finite element simulations are done with different model types and reported.

2 Description of the new impact test facilities at VTT

A flexible experimental platform has been created at VTT for intermediate scale impact tests. The test apparatus consists of two main parts. First, a 13.5 m long pressure accumulator is used to provide the required initial energy for the test. Second, a 12 m long acceleration tube is used to accelerate test missiles to a final velocity of 100 m/s to 200 m/s. The mass of the missile can be up to 100 kg. In the tests, missile impacts on a concrete wall or on a steel force measurement plate. The test facility has been further developed and improved since the first version was taken in use in 2003.

Two versions of the force plate system are shown in Figure 1. The force plates have been supported directly to the back wall using only the back pipes. The 3D missile tests were performed by using heavy steel frame, horizontal beams and three force plates installed in front of the frame, depicted in Figure 1 on the right.

Figure 1. The second model (left) and third model of force plate construction.

Figure 2. Dry (empty) aluminium (Al) pipe missile and wet (water filled) missile.

Tests have been done with a steel piston inside the acceleration tube and the missile installed on the rails at the top of the acceleration tube. An aluminium pipe missile with a diameter of 0.25 m and wall thickness of 5 mm was used in impact tests of slabs with a thickness of 0.15 m (see Figure 2). The aircraft model tests on force plate have been done using a smaller aluminium pipe, with a diameter of 200 mm and wall thickness of 4 mm. At the end of the test series, wings and engines were included in the model (see Figure 3) and also in some tests wings were filled with water in order to study the spreading of fuel (Kuutti, 2007).

Pre-stressed concrete slabs with a thickness of 250 mm were tested using rigid hard steel missiles with a diameter of 150 mm, wall thickness of 10 mm and filled with concrete, shown in Figure 3 on the left.

Figure 3. The rigid steel pipe missile with a diameter of 150 mm (left) and an aeroplane model with wings (right).

The dimensions of the concrete slab in the soft missile tests were: width 2 m, length 2.3 m, support length 2.2 m and thickness 0.15 m. Bending and in some cases also shear reinforcement was applied. The slabs were supported on the vertical edges by the test frame shown in Figure 4 on the left.

The pre-stressed concrete slabs were of the same size except the thickness was 0.25 m. The slab contained bending and in some cases also shear reinforcement. In the new test frame, the slabs are simply supported on all the four edges. The new test frame is shown in Figure 4 on the right.

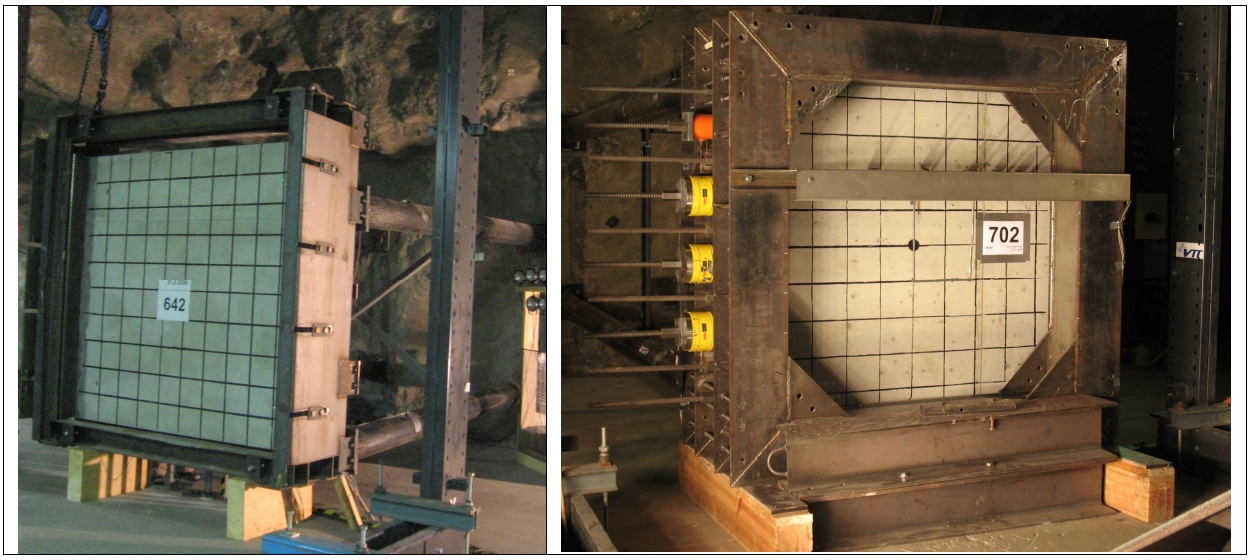

Figure 4. One way support system and test slab in soft missile test (left). Pre-stressed test slab with a thickness of 0.25 m and support system 2 in hard missile test (right).

The missile tests onto force plate in the IMPACT project phase 1 are composed of 7 test series given in Table 1 and of concrete slab tests shown in Table 2.

Table 1. Missile impact tests on force plate.

Missile type	**Launch type**	**Number of tests**
Pre-tests with steel piston	Inside	5
Pre-tests with steel pipe	Inside	5
Thin walled steel pipe, dry, water or light concrete inside	Inside	14
Al. pipe, dry	Inside	3
3D missile	Outside	12

Table 2. Concrete plate tests in the phase 1.

Test type	**Number of tests**
Soft missile on 0.15 m thick plate	12
Hard missile on 0.25 m thick pre-stressed wall	13

Measurements

The data from sensors have been gathered using a sampling frequency of 100 kHz. During the measuring, anti-aliasing filtering and simultaneous sampling were applied. The maximum number of channels used in the tests has been 32. The following sensors have been used in IMPACT tests:

- Force transducers behind the force plate (used also in measuring the post-tension force of Dywidag bars).
- Strain gauges on back pipes to measure reaction forces.
- Strain gauges on supporting frame to control the bending stresses of beams.
- High speed cameras to video collision
- Strain gauges in rebars inside concrete to measure strains of rebars
- Strain gauges on surface of concrete slab to measure strains of concrete
- Deflection transducers to measure horizontal deflections of the slab
- Laser sensors to measure the speed of missile
- Accelerometer at the back of the missile (wired measurements)
- Accelerometers at the back of the concrete wall
- Pressure sensors to measure the air pressure inside the acceleration tube or near the concrete slab

The measuring device and deflection transducers are shown in Figure 5. The transducer is a mechanical sensor, which is placed on the surface of the slab and measures the displacement of the surface as a function of time.

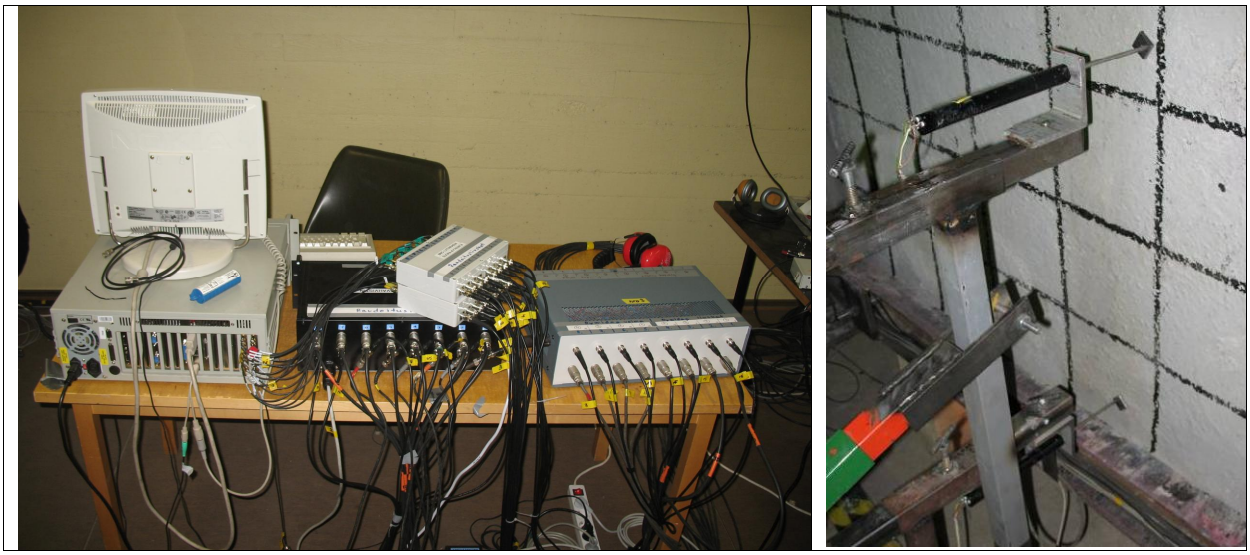

Figure 5. Data collection device (left) and deflection transducers in front of the slab (right).

The high frequency laser sensors are used to measure the velocity of the missile before hitting the target and reaction forces are measured by strain gauges glued on the back pipes (Figure 6). The post-tension force of Dywidag bars and the force-time function due to missile impact is measured by force transducers shown in Figure 7. The strains of rebars and concrete are measured by high capacity strain gauges, which are attached on rebars and on the surface of concrete, see Figure 8.

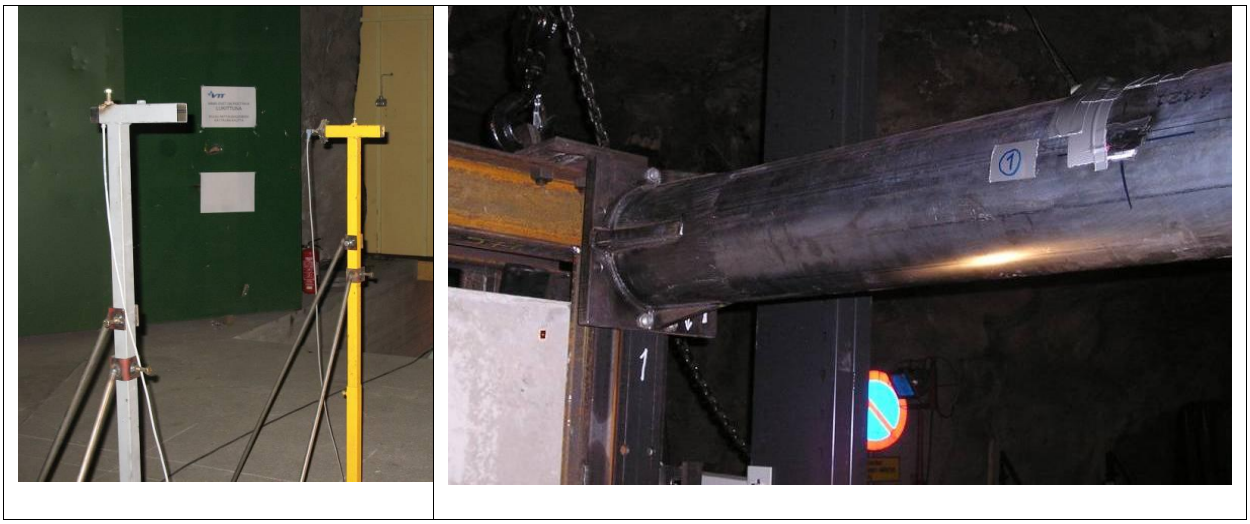

Figure 6. The laser sensors (left) and a strain gauge on the back pipe (right).

Figure 7. The force transducers of Dywidag bars (left) and the force transducers behind the force plate (right).

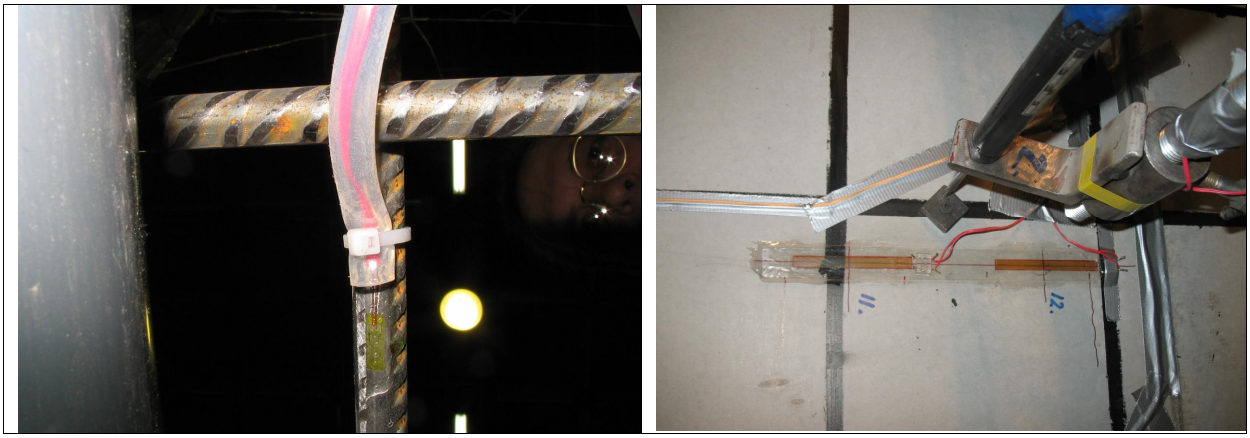

Figure 8. A strain gauge glued on rebar (left) and a strain gauge on the front surface of the slab (right).

3 Studies of impacted slabs by simplified methods

3.1 Two degree of freedom model for shear deformable plate

A two degree of freedom model (TDOF model), e.g. the CEB model of Reference (CEB, 1988), can be used in analysing the overall impact behaviour of concrete slabs, in Figure 9. In this model spring 1 and mass 1 are connected to the global bending deformation and movement of the plate while spring 2 and mass 2 are used in modelling the local shear behaviour in the missile impact area.

The behaviour of element 1 (bending spring) is shown in Figure 9 and the local behaviour connected with the possible formation of a shear cone (shear spring) is shown in Figure 10. The internal force in spring 2 is composed of the contributions due to concrete, r_c, stirrups, r_s, and bending reinforcement, r_b. Concrete behaves elastically until the displacement difference (between the masses) $u_{21}=u_2-u_1$ reaches the value u_{cu}. Stirrups are assumed to break when the difference is $u_{21}=u_{su}$. The ultimate displacement connected to concrete deformation u_{cu} is very small and a large displacement difference is needed to activate a significant bending reinforcement contribution to shear spring force. The bending reinforcement breaks when $u_{21}=u_{bu}$.

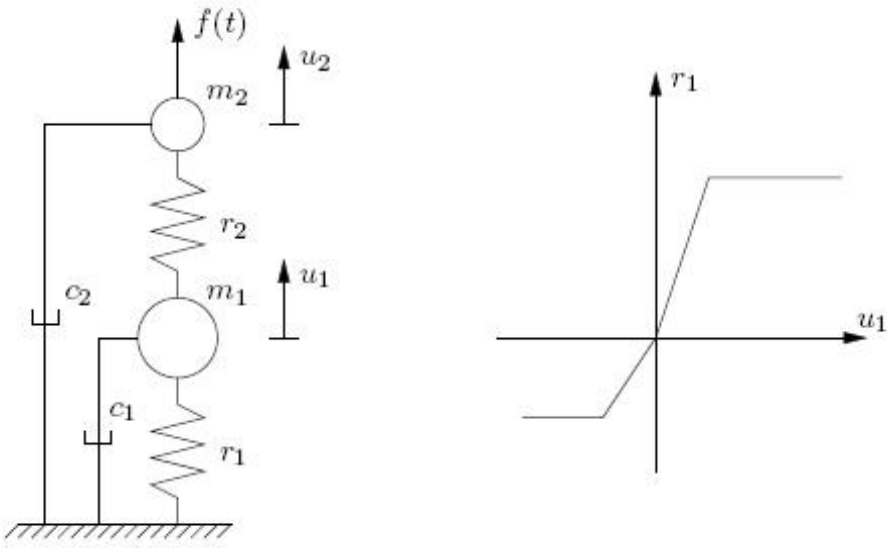

Figure 9. A two degree of freedom (2-dof) impact model.

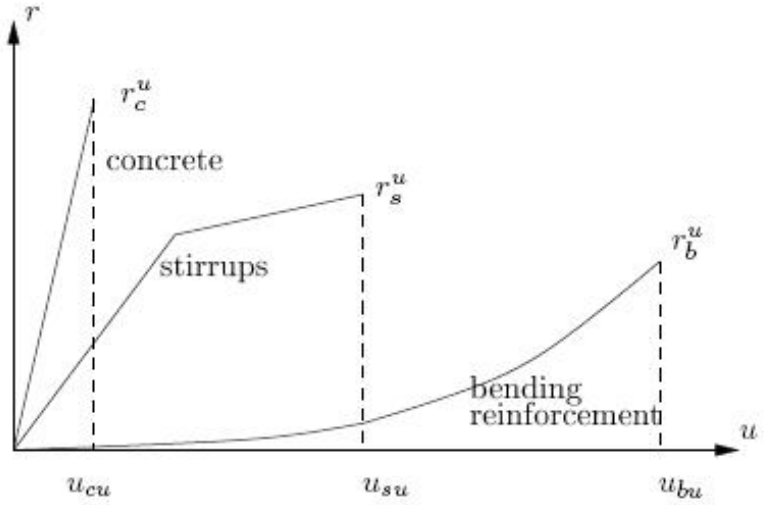

Figure 10. Local shear strength of slab model showing the contributions of concrete, stirrups and bending reinforcement.

3.1.1 Stiffness, strength and effective mass of bending mode

According to Reference [Biggs, 1964, p. 266], the bending rigidity of a cracked cross section can be determined from

$$D = \frac{1}{2} b d^3 \left(\frac{1}{12} + 5.5\rho_s \right) E_c ,$$

where b and d are the width and effective depth of the cross section, $\rho_s = A_s/d$ is the reinforcement ratio and E_c is the modulus of elasticity of concrete. A similar relation is used also in Reference (ASCE, 1980).

Alternatively, in cracked state, when the concrete (in compression) and the reinforcing steel still behave elastically, a bending rigidity coefficient can be determined by assuming a triangular concrete stress distribution over the top compression zone with a depth of x. If d is the effective slab depth (from the top) and the distance from the neutral axis to the bending reinforcement is $d - x$, then one obtains

$$D = \left(d - \frac{x}{3} \right) (d - x) A_s E_c$$

for the bending stiffness per unit width of cross section.

Denoting

$$n = \frac{E_s}{E_c}$$

the horizontal equilibrium equation in the absence of axial load can be written in the form

$$x^2 + 2nA_s x - 2nA_s d = 0,$$

from which

$$x = -nA_s \pm \sqrt{n^2 A_s^2 + 2nA_s d}\,.$$

The relevant root can be written in the form

$$x = d\left[\sqrt{(2 + n\rho_s)n\rho_s} - n\rho_s\right],$$

where

$$\rho_s = \frac{A_s}{d}$$

is the reinforcement ratio.

If the top (*t*) and bottom (*b*) bending reinforcements are different, then the above values for x and D are determined for the loading direction, x_b and D_b, and for the opposite direction, x_t and D_t.

The (elastic) stiffness of the bending spring, number 1, is needed for different plates, boundary conditions and loading cases.

The limit load and effective mass are also needed for the equations of motion of the TDOF system.

One-way slab

For a simply supported one-way slab with a width of b and with a span of l the bending spring stiffness becomes

$$k_b = \frac{48Db}{l^3}.$$

The limit load obtained with a central yield line is

$$R_p = \frac{4m_p b}{l}.$$

The plastic bending moment in a cross section, needed in the above plastic limit load, can be calculated from

$$m_p = \rho_s d^2 f_y \left(1 - \frac{\rho_s f_y}{1.7 f_c}\right),$$

where f_y is the yield stress of steel, f_c is the compression strength of concrete and ρ_s is the reinforcement ratio.

The effective mass calculated with a piecewise linear deflection profile becomes

$$m_e = \frac{1}{3}\rho hlb.$$

Local behaviour

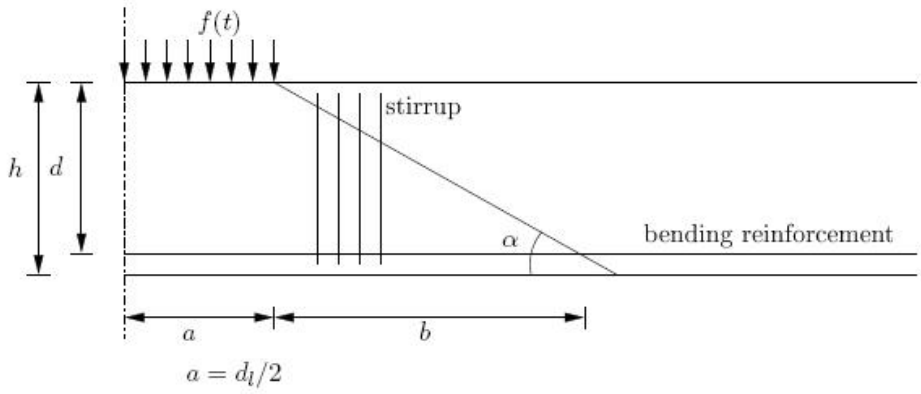

Figure 11. Assumed shear punching cone.

The local resistance of the slab to impact deformation is due do concrete, stirrups and bending reinforcement. The resistive force of concrete alone can be determined by assuming a shear cone with an angle α measured from horizontal plane (see Figure 11). If f_t is the tension strength of concrete, then

$$r_c^u = \pi\left[\left(a + \frac{h}{\tan\alpha}\right)^2 - a^2\right] f_t .$$

The ultimate cone displacement in the concrete deformation mode can be assumed as

$$u_{cu} = \frac{1}{3}\frac{f_t}{E_c} h,$$

where h is the plate thickness. The ultimate resistive force and cone displacement due to stirrups is determined in a similar way, and it yields

$$r_s^u = \pi\left[\left(a + \frac{h}{\tan\alpha}\right)^2 - a^2\right] A_{ss} f_{sy},$$

where A_{ss} is the amount of stirrups [m^2/m^2] and f_{sy} is the yield stress of stirrups. The ultimate elastic displacement due to stirrup deformation is assumed as

$$u_{se} = \frac{1}{3}\frac{f_{sy}}{E_s} h .$$

The ultimate cone displacement due to the deformation of stirrups is assumed as

$$u_{su} = 0.9\varepsilon_{su} h,$$

where ε_{su} is the ultimate stirrup strain.

The contribution of the bending reinforcement to the shear resistance of the punching cone can be assessed by assuming a parabolic deflection mode

$$w(x) = u\left[1-\left(\frac{x}{a}\right)^2\right],$$

where $u = u_{21}$ and $x \in [0, a]$ for the net of bending reinforcement. An average strain in the reinforcement bar due to bending is

$$\varepsilon = \frac{s-a}{a} = \frac{s}{a} - 1,$$

where s is the length of reinforcement bar in the deformed state. The arc length s can be calculated from

$$s = \int_0^a \sqrt{1+\left(\frac{dw}{dx}\right)^2}\, dx = \int_0^a \sqrt{1+\left(\frac{2ux}{a^2}\right)^2}\, dx,$$

and the average strain in reinforcement bar becomes

$$\varepsilon = \frac{1}{2}\left\{\sqrt{1+\left(\frac{4u}{l}\right)^2} + \frac{l}{4u}\ln\left[\frac{4u}{l} + \sqrt{1+\left(\frac{4u}{l}\right)^2}\right]\right\} - 1,$$

where l is the bottom diameter of the shear cone, i.e. the diameter of area where the parabolic deflection mode is assumed,

$$l = 2\left(\frac{h}{\tan\alpha} + a\right).$$

In an isotropically reinforced plate the membrane force per unit length would be

$$t = A_s \sigma(\varepsilon),$$

where A_s is the amount of bending reinforcement.

The total vertical component of this inclined membrane force calculated from a circular line with a radius of *a is*

$$r_b = 2\pi a t \sin\varphi = \pi \sin\varphi l A_s \sigma(\varepsilon),$$

where φ is the angle of inclination of the bent reinforcement bar at a distance of a from the centre point, i.e.

$$\varphi = \frac{dw}{dx}(a) = \arctan\frac{4u}{l}.$$

In the Reference (CEB, 1988), a slightly different formula for the resistive force due to bending reinforcement is introduced and it is

$$r_b = 2\sin\left(\arctan\frac{4u}{l}\right) l A_s \sigma(\varepsilon).$$

Punching shear cone

The volume of the assumed punching cone is

$$V_2 = \frac{\pi}{3}(h + a\tan\alpha)\left(a + \frac{h}{\tan\alpha}\right)^2 - \frac{\pi}{3}a^2 a\tan\alpha$$

or

$$V_2 = \pi h\left[a^2 + \frac{ah}{\tan\alpha} + \frac{1}{3}\left(\frac{h}{\tan\alpha}\right)^2\right].$$

The mass of the assumed punching cone then becomes

$$m_2 = \tilde{\rho}\pi h\left[a^2 + \frac{ah}{\tan\alpha} + \frac{1}{3}\left(\frac{h}{\tan\alpha}\right)^2\right],$$

where $\tilde{\rho}$ is the equivalent density of the reinforced concrete, α is the angle of the punching cone (measured from horizontal plane) and h is the plate thickness.

The mass number 1 in the TDOF model is

$$m_1 = m_e - m_2.$$

Mass and stiffness proportional damping

In Rayleigh damping the damping matrix is assumed to be proportional to the mass matrix and the stiffness matrix in the form

$$\mathbf{C} = \alpha\mathbf{M} + \beta\mathbf{K},$$

where α and β are constants used to control damping.

For an elastic structure, by the superposition method, n independent equations are obtained in the form

$$m_i\ddot{u}_i + c_i\dot{u}_i + k_i u_i = f_i, \quad i = 1,...,n,$$

where m_i, c_i and k_i are the mass, damping and stiffness coefficients and n is the number of degrees of freedom in the system. The damping coefficient for equation i in the considered case of mass and stiffness proportional damping is

$$c_i = \alpha m_i + \beta k_i.$$

Dividing the equation of motion by m_i yields

$$\ddot{u}_i + 2\zeta_i\omega_i\dot{u}_i + \omega_i^2 u_i = h_i, \quad i = 1,...,n,$$

in which $2\zeta_i\omega_i = \alpha + \beta\omega_i^2$, $\omega_i^2 = k_i / m_i$, $h_i = f_i / m_i$ and ω_i is the frequency of the i -th mode.

From the equation

$$2\zeta_i\omega_i\dot{u}_i = \alpha + \beta\omega_i^2$$

the modal damping ratio is obtained as

$$\zeta_i = \frac{\alpha}{2\omega_i} + \beta\frac{\omega_i}{2}.$$

The frequency giving the minimum value for ζ_i is obtained from the condition

$$\frac{d\zeta_i}{d\omega_i} = -\frac{\alpha}{2\omega_i^2} + \beta\frac{1}{2} = 0$$

yielding

$$\beta = \frac{\alpha}{\omega_i^2} \quad \Rightarrow \quad \omega_i = \omega_m = \sqrt{\frac{\alpha}{\beta}}.$$

The corresponding minimum value ζ_m of damping ratio ζ becomes

$$\zeta_m = \frac{\alpha}{2}\sqrt{\frac{\beta}{\alpha}} + \beta\frac{1}{2}\sqrt{\frac{\alpha}{\beta}} = \sqrt{\alpha\beta} \ .$$

From the equations presented above, $\beta = \alpha/\omega_m^2$ and $\zeta_m^2 = \alpha\beta$ and the coefficients needed in computing the damping matrix **C**, are obtained in the form

$$\alpha = \zeta_m\omega_m, \quad \beta = \frac{\zeta_m}{\omega_m}.$$

These values for the coefficients α and β give the required damping ratio ζ_m at the frequency ω_m.

Alternatively, requiring that at two frequencies, $\omega = \omega_a$ and $\omega = \omega_b$, the damping ratios are ζ_a and ζ_b, i.e.

$$\zeta_a = \frac{\alpha}{2\omega_a} + \beta\frac{\omega_a}{2}$$

$$\zeta_b = \frac{\alpha}{2\omega_b} + \beta\frac{\omega_b}{2},$$

gives for the constants α and β

$$\alpha = \frac{2(\zeta_a\omega_b - \zeta_b\omega_a)}{\frac{\omega_b}{\omega_a} - \frac{\omega_a}{\omega_b}}$$

and

$$\beta = \frac{2(\zeta_a\omega_a - \zeta_b\omega_b)}{\omega_a^2 - \omega_b^2}.$$

The damping ratio, ζ, can be plotted as a function of the period of vibration, T,

$$T = \frac{2\pi}{\omega} = \frac{1}{f},$$

where

$$f = \frac{\omega}{2\pi}$$

is the frequency. In damped vibration

$$T_D = \frac{2\pi}{\omega_D},$$

in which

$$\omega_D = \omega\sqrt{1-\zeta^2}.$$

The critical damping for a SDOF model is

$$c_{cr} = 2\sqrt{km},$$

where k and m are the stiffness coefficient and the mass of the model. Damping coefficients for the TDOF model can be defined as, (CEB, 1998)

$$c_1 = \xi_1 2\sqrt{m_e k_b},$$

$$c_2 = \xi_2 2\sqrt{m_2 k_{sc}},$$

where $k_{sc}=r_{cu}/u_{cu}$ and the coefficients are in the ranges, $\xi_1 \in [0.02,...,0.1]$ and $\xi_2 \in [0.005,...,0.01]$.

In the case of a diagonal damping matrix, the equations of motion are

$$m_1\ddot{u}_1 + c_1\dot{u}_1 - r_2 + r_1 = 0,$$

$$m_2\ddot{u}_2 + c_2\dot{u}_2 + r_2 = f,$$

where f is the load, r_1 and r_2 are the internal forces and the damping forces are

$$g_i = c_1\dot{u}_1, \quad g_2 = c_2\dot{u}_2.$$

The above definition of damping, i.e. the use of a diagonal damping matrix, however, means that the damping elements, dashpots, are fixed on the ground.

In Rayleigh damping the damping matrix, **C**, for the TDOF system can be formed as

$$\mathbf{C} = \alpha\mathbf{M} + \beta\mathbf{K} = \begin{bmatrix} C_{11} & C_{12} \\ C_{21} & C_{22} \end{bmatrix} = \begin{bmatrix} \alpha m_1 + \beta(k_1 + k_2) & -\beta k_2 \\ -\beta k_2 & \alpha m_2 + \beta k_2 \end{bmatrix}.$$

In a special case of stiffness proportional damping (see Figure 12) the damping matrix is

$$\mathbf{C} = \begin{bmatrix} c_1 + c_2 & -c_2 \\ -c_2 & c_2 \end{bmatrix} = \beta \begin{bmatrix} k_1 + k_2 & -k_2 \\ -k_2 & k_2 \end{bmatrix},$$

and the equations of motion become

$$m_1\ddot{u}_1 + (c_1 + c_2)\dot{u}_1 - c_2\dot{u}_2 - r_2 + r_1 = 0,$$

$$m_2\ddot{u}_2 - c_2\dot{u}_1 + c_2\dot{u}_2 + r_2 = f.$$

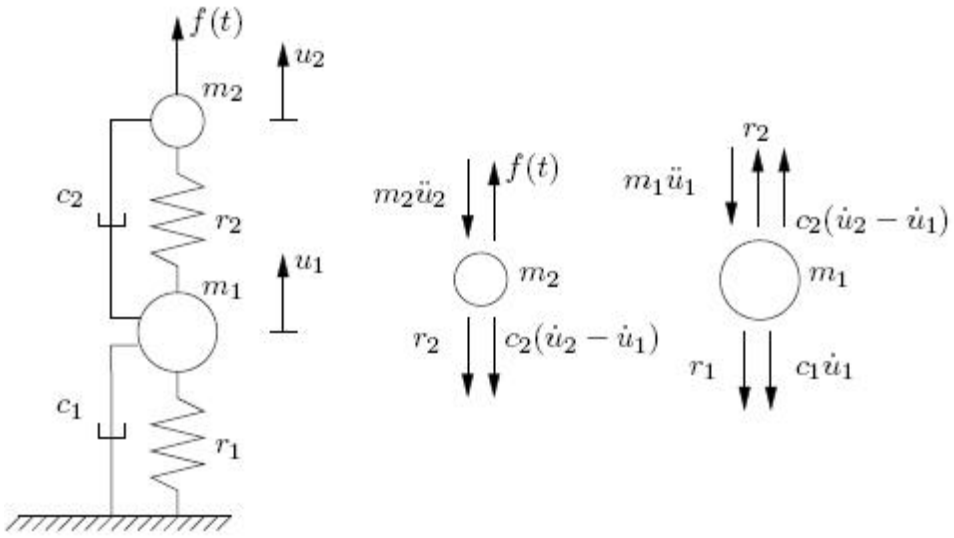

Figure 12. Two degree of freedom model with stiffness proportional damping matrix.

In this case the damping forces are

$$g_1 = (c_1 + c_2)\dot{u}_1 - c_2\dot{u}_2$$

and

$$g_2 = -c_2\dot{u}_1 + c_2\dot{u}_2.$$

Determination of damping

The damping factor ς may be estimated from

$$\varsigma = \frac{\delta}{\sqrt{(2\pi)^2 + \delta^2}},$$

where δ is the logarithmic decrement defined by

$$\delta = \frac{1}{n}\ln\frac{u_i}{u_{i+n}},$$

in which u_i and u_{i+n} are two non-consecutive amplitudes n cycles away. A less accurate formula is

$$\varsigma = \frac{\ln\frac{u_0}{u_1}}{\sqrt{(2\pi)^2 + \left(\ln\frac{u_0}{u_1}\right)^2}}.$$

For small values of ς, the following equality approximately holds;

$$\varsigma = 2\pi\varsigma .$$

From the plot of a deflection-time recording from Test 642, $u_2 / u_3 \approx 5/3$ and

$$\varsigma = \frac{\ln\frac{5}{3}}{\sqrt{(2\pi)^2 + \left(\ln\frac{5}{3}\right)^2}} \approx 0.08 .$$

Similarly, using amplitudes $u_{1+\frac{1}{2}}$ and $u_{2+\frac{1}{2}}$ gives $\varsigma \approx 0.125$ and using amplitudes u_1 and u_2 yields $\varsigma \approx 0.11$. Utilizing the ratio of amplitudes u_2 and u_5 with $n = 3$ (three cycles away), gives $\varsigma \approx 0.085$ for the damping factor.

3.1.2 One-way Slab

In the present projectile impact test series an aluminium missile was shot on a reinforced concrete one-way target plate. The dimensions of the slabs in the test series are: width 2 m, length 2.3 m, support length 2.2 m and thickness 0.15 m. The slab was simply supported on two opposite sides and free on the two other sides, depicted in Figure 13, and reinforced using bars with a diameter of 8 mm and a spacing of 50 mm, in each way and on each face. In the following calculation models, it is assumed that the distance of the centre of rebars from the plate face is 19 mm. The effective plate thickness, d, becomes then 0.15 m - 0.019 m = 0.131 m. The reinforcement ratio is in this case 100 A_s/h = ρ_p = 0.67 %.

Material parameters of concrete are: E_c = 35000 MPa, ν = 0.20, f_c = 58 MPa and f_t = 3.04 MPa (in Test 642). The bending reinforcement area in each direction is A_{s1} = 10.05 cm^2/m and A_{s2} = 10.05 cm^2/m. In some cases, as in Test 673, the shear reinforcement area was A_{ss} = 50 cm^2/m^2.

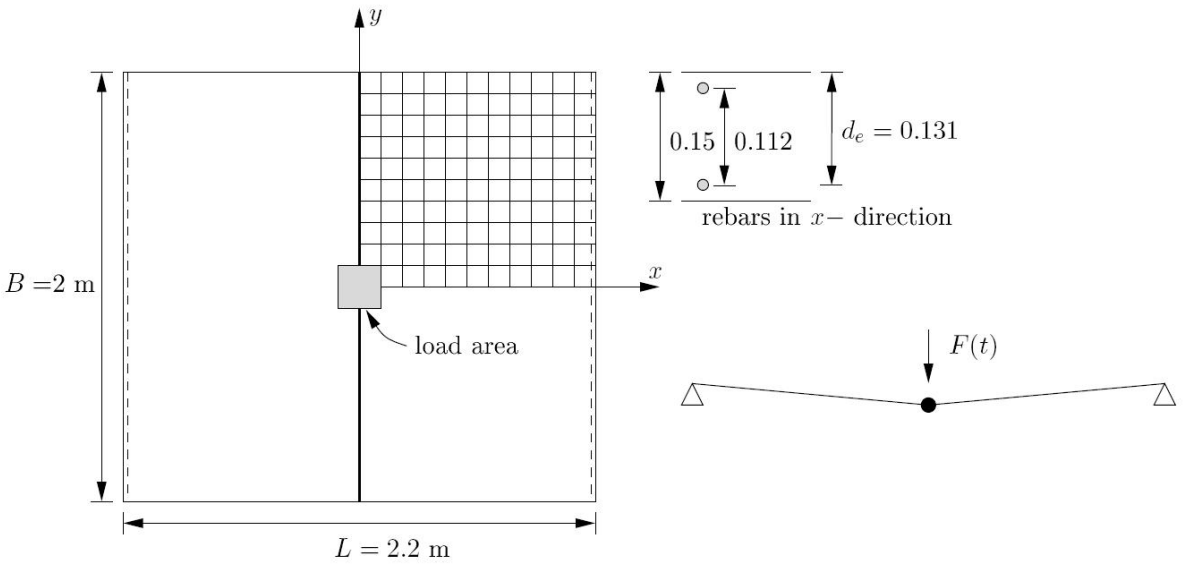

Figure 13. Reinforced concrete one-way slab impacted by a missile.

The effective thickness of the plate is d = 0.131 m, when the distance of the rebars in the x-direction is assumed to be 0.056 m from the middle surface. Assuming f_c = 58 MPa, f_y = 560 MPa (a stress value obtained at 5 % strain value in the stress strain curve used in finite element calculations) the plastic moment capacity becomes

$$m_p = 0.0705 \text{ MNm/m}.$$

Assuming a shear cone angle of 35^0 the masses of the TDOF model become $m_1 = 69$ kg and $m_2 = 491$ kg when the effective mass is 560 kg. The stiffness coefficients of the shear and bending springs are $k_s = 0.22 \cdot 10^{12}$ N/m and $k_b = 0.22 \cdot 10^8$ N/m, respectively.

The plastic limit load by the mechanism with one yield line crossing the plate, in Figure 13, is

$$F_p = 4m_p \frac{B}{L} = 3.636 m_p = 0.256 \text{ MN}.$$

The internal plastic force of the bending spring is thus also

$$R_p = 0.256 \text{ MN}.$$

When calculating the equivalent mass of the SDOF and TDOF models, an effective density of the slab is defined as

$$\rho_e = (1 - 4\rho_p)\rho_c + 4\rho_p \rho_s = (1 - 0.0268)2400 + 0.0268 \cdot 7850 = 2546 \,\text{kg/m}^3$$

where ρ_p = 0.67%=0.0067 is the reinforcement ratio and where ρ_c = 2400 kg/m^3 and ρ_s = 7850 kg/m^3 are the assumed densities of concrete and steel, respectively. The equivalent mass becomes

$$m = \frac{M}{3} = \frac{0.15 \cdot 2.2 \cdot 2.0 \cdot 2546}{3} = 560 \,\text{kg},$$

where M is the mass of the slab.

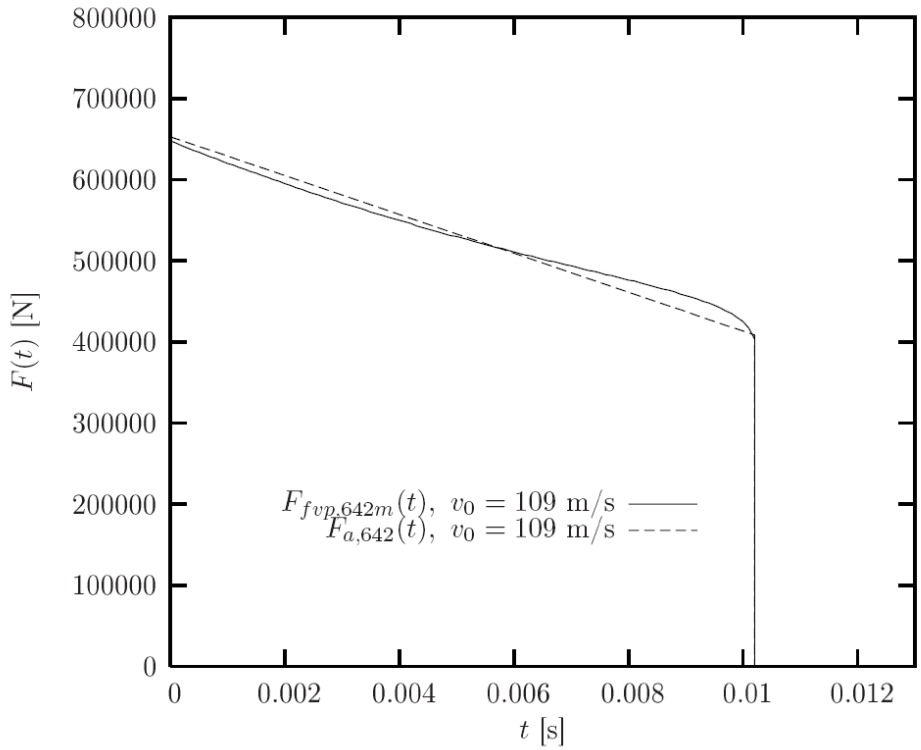

Figure 14. Load function due to dry aluminium missile in Test 642.

The impact load due to an aluminium pipe missile is shown in Figure 14. Curve labelled "$F_{fvp,642m}$" is calculated using the Riera method assuming a folding viscoplastic mechanism in calculating the crushing force, P_c, (Jones, 1989). The Cowper-Symonds viscoplastic power law type strain rate dependency is assumed for aluminium with parameter values q = 4 and D = 6500. The curve "$F_{a,642}$" is a linear approximation of the actual force function to be used in calculations.

The approximate force diminishes from 0.653 MN to 0.4086 MN during a time interval of 0.0102 s. The simplified load function corresponds to that obtained in Test 642 with a dry aluminium missile (excluding the effect of front rail for simplicity). The impulse of the load function is I = 5414 Ns.

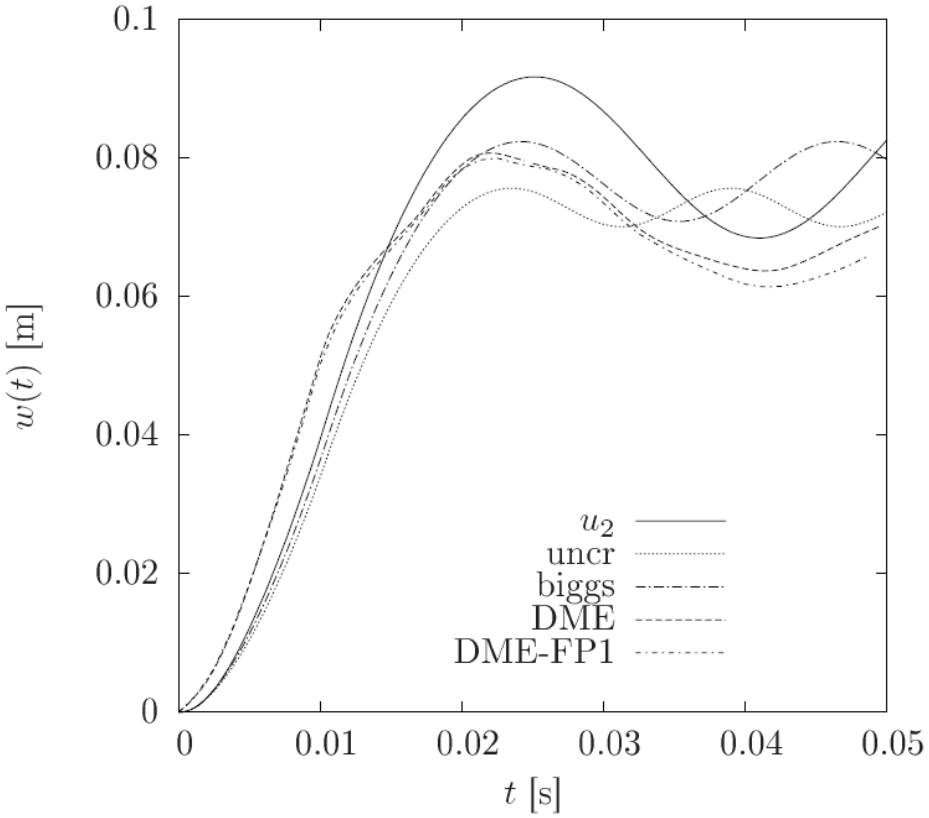

Figure 15. Deflection of 2-dof plate model of Test 642.

Figure 15 shows the deflections calculated with the TDOF model of Test 642 without damping (curve "u_2"). The assumed shear cone angle is 35^0. The solution with the simple TDOF model is compared to the deflection curve "DME" which is computed with Abaqus using a damaged plasticity model for concrete and an elastic plastic strain hardening model for reinforcement. The used plate element mesh is depicted in Figure 13. A layered plate model with a nine point Simpson integration rule is used in the thickness direction. In case "DME-FP1" the support frame (FP1) is modelled with beam elements. The curve with label "uncr" is calculated with a TDOF model (the same as SDOF in this case) using the uncracked bending stiffness of the plate section, while the curve "biggs" is obtained by using the bending rigidity of Reference (Biggs, 1964, Equation (4.1)).

In Figure 16, the deflection of the same TDOF model, when the effect of damping is included, is shown. Figure 17 shows the damping ratio ζ in Test 642 in the case: α=30^o (angle of shear cone), ζ_a=0.1, ζ_b=0.01, f_a=33.08, f_b=13440, α=41.56, β=0.231*10^{-6} (damping coefficients).

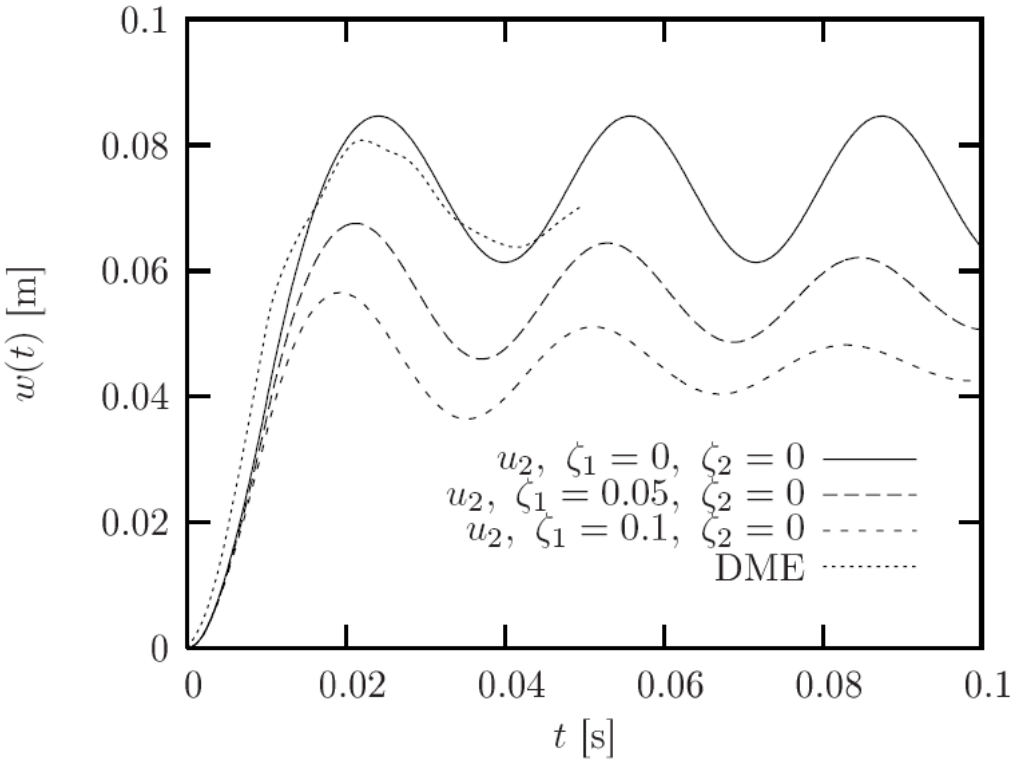

Figure 16. Deflection of TDOF plate model of Test 642 assuming Rayleigh damping with the damping factors given in the figure.

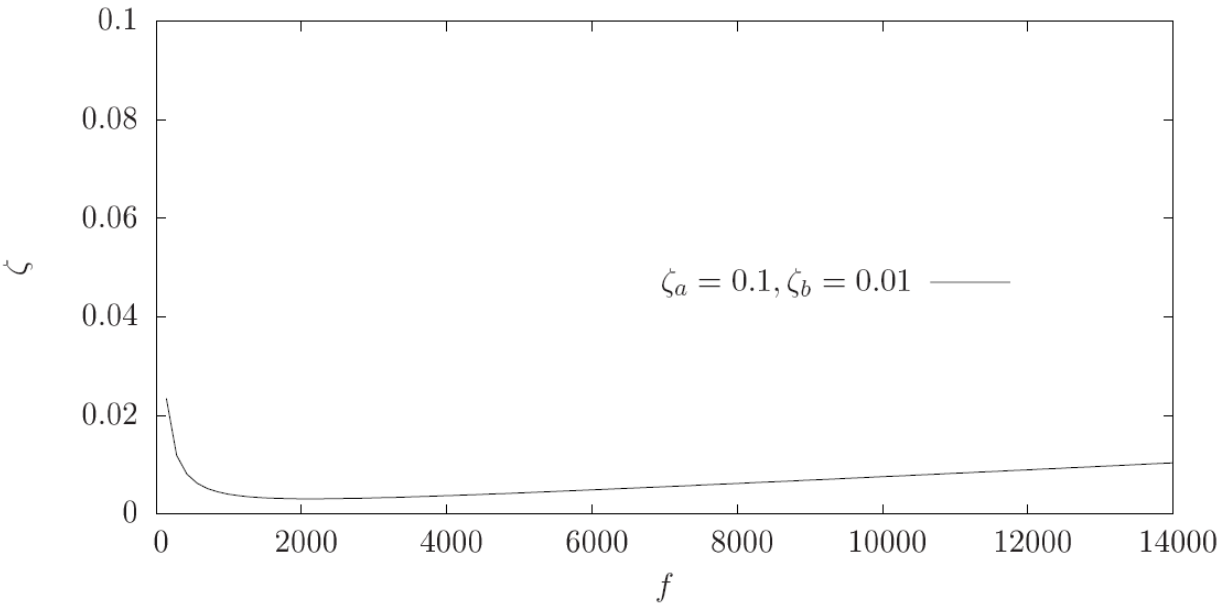

*Figure 17. Damping ratio ζ in Test 642 in the case: α=30^o (angle of shear cone), ζ_a=0.1, ζ_b=0.01, f_a=33.08, f_b=13440, α=41.56, β=0.231*10^{-6} (damping coefficients).*

3.2 Dry aluminium missile tests

Dry aluminium missile tests are analysed by a two degree of freedom (TDOF) model assuming a diagonal damping matrix and alternatively a non-diagonal damping matrix (result option b). In the case of diagonal damping matrix the damping factors for masses 1 and 2 are $\varsigma_1 = 0.05$ and $\varsigma_2 = 0.0025$, while for Rayleigh damping matrix the damping factors are $\varsigma_1 = 0.1$ and $\varsigma_2 = 0.01$.The shear cone angle is varied from 30 to 40 degrees. Solution curves 1, 2, 3, 4 and 5 are connected to shear cone angles (from horizontal plane) of 30, 32.5, 35, 37.5 and 40 degrees, respectively.

Dry aluminium missile Test 642 with impact velocity 109 m/s

Figure 18 shows the deflection of a two degree of freedom plate model (TDOF model) of Test 642 when a diagonal damping matrix has been used. In this test, the impact velocity was v_0 = 109 m/s. Figure 19 shows the corresponding deflection curves calculated by a TDOF model of Test 642 adopting a non-diagonal damping matrix. The forces of TDOF model calculated with α = 30° and assuming diagonal damping are shown in Figure 20. The corresponding results calculated with α = 40° are presented in Figure 21. In these figures, *f* is the impact load history, r_1 and r_2 are the internal forces and g_1 and g_2 are the damping forces. Figure 22, Figure 23 and Figure 24 show the corresponding force histories in Test 642 calculated with a non-diagonal damping matrix and assuming shear cone angles of 30°, 35° and 40°.

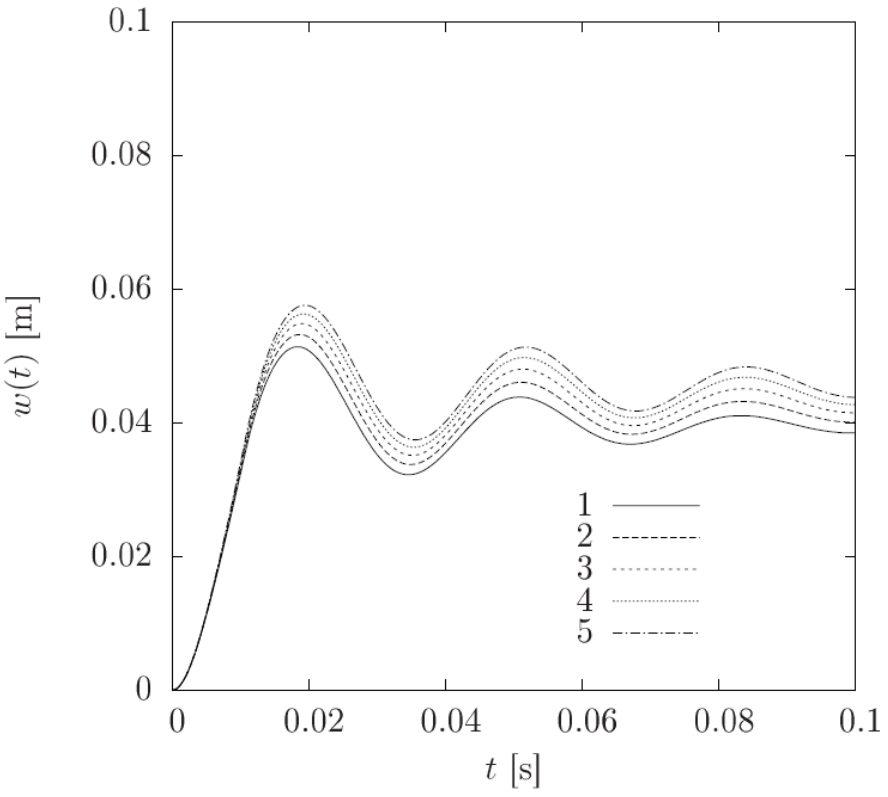

Figure 18. The deflection of TDOF plate model of Test 642 with a diagonal damping matrix and v_0 =109 m/s.

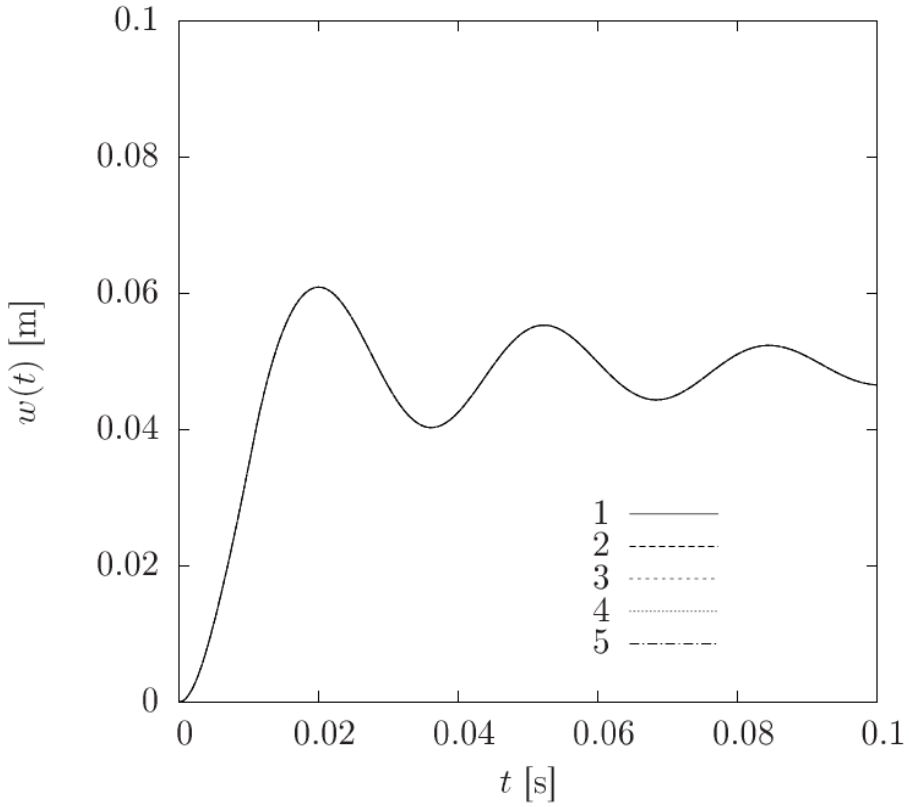

Figure 19. Deflection of TDOF plate model of Test 642 with a non-diagonal damping matrix and v_0 =109 m/s.

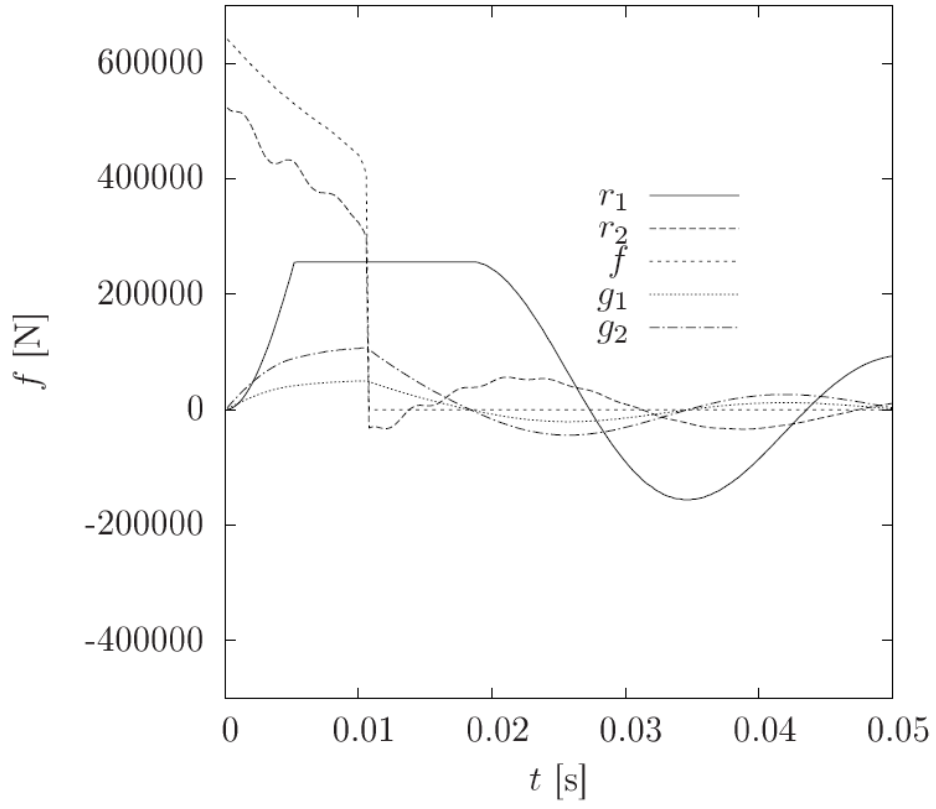

Figure 20. Forces of TDOF plate model of Test 642 with a diagonal damping matrix, v_0=109 m/s and α=30^o

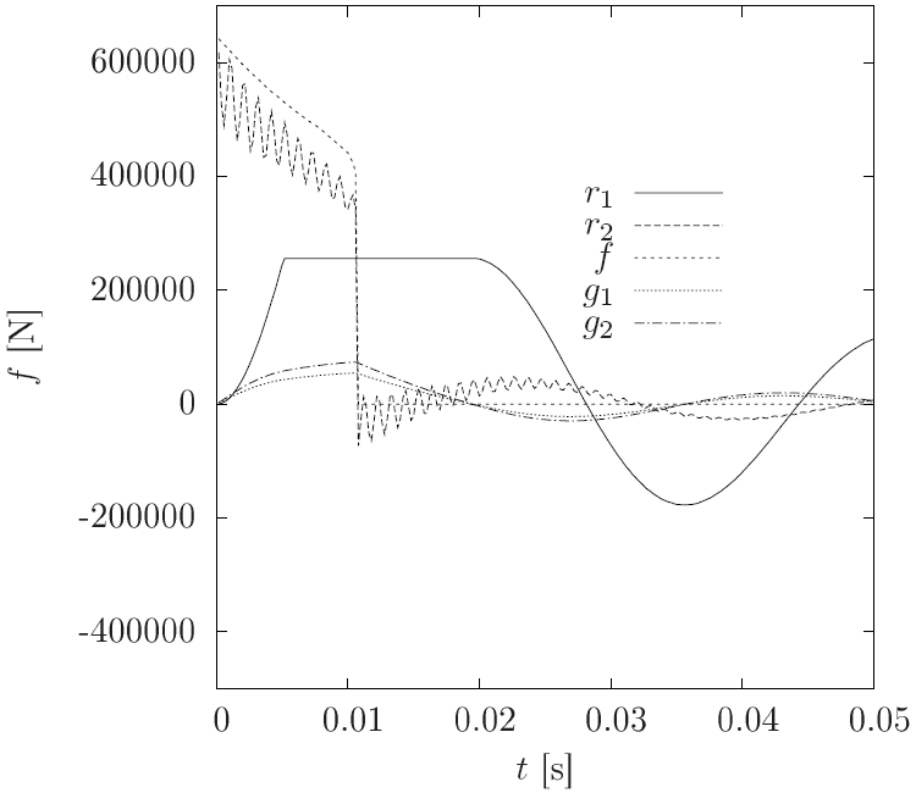

Figure 21. Forces of TDOF plate model of Test 642 with a diagonal damping matrix and v_0=109 m/s, α=40°.

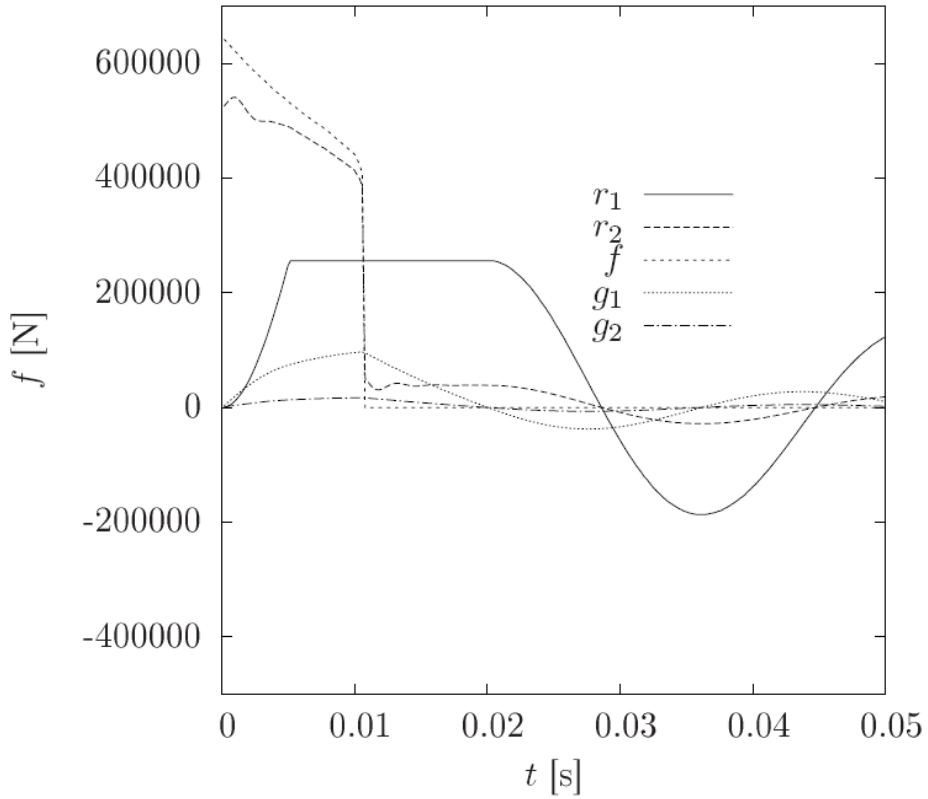

Figure 22. Forces of TDOF plate model of Test 642 with a non-diagonal damping matrix, v_0=109 m/s, α=30°.

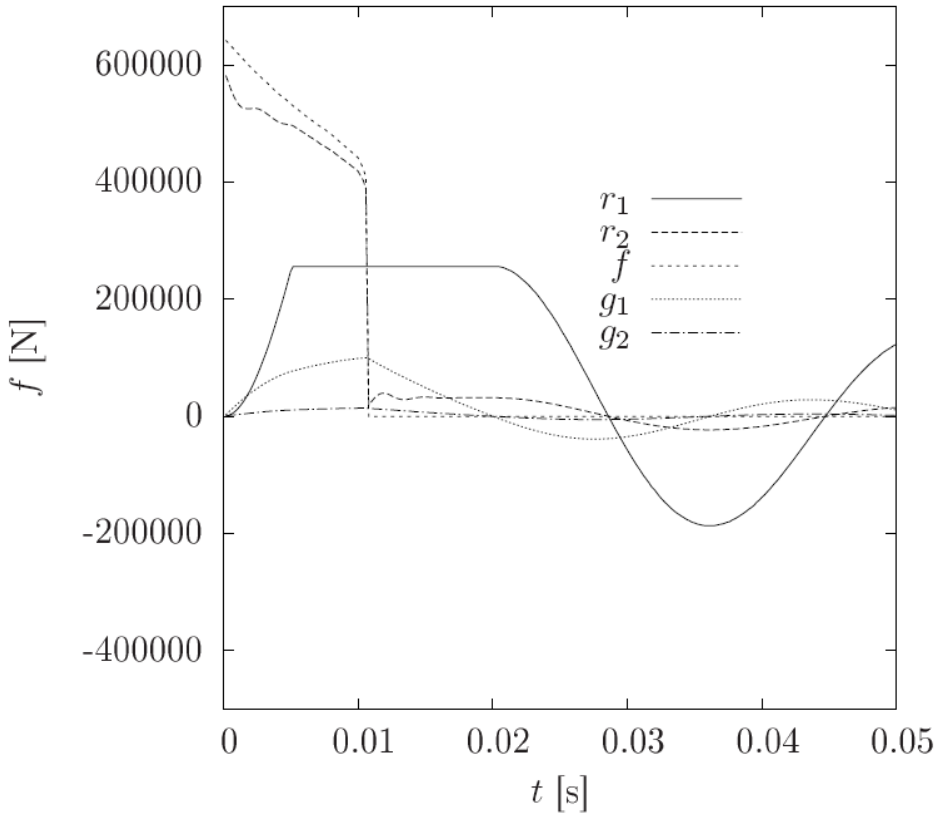

Figure 23. Forces of TDOF plate model of Test 642 with a non-diagonal damping matrix, v_0=109 m/s and α=35^o.

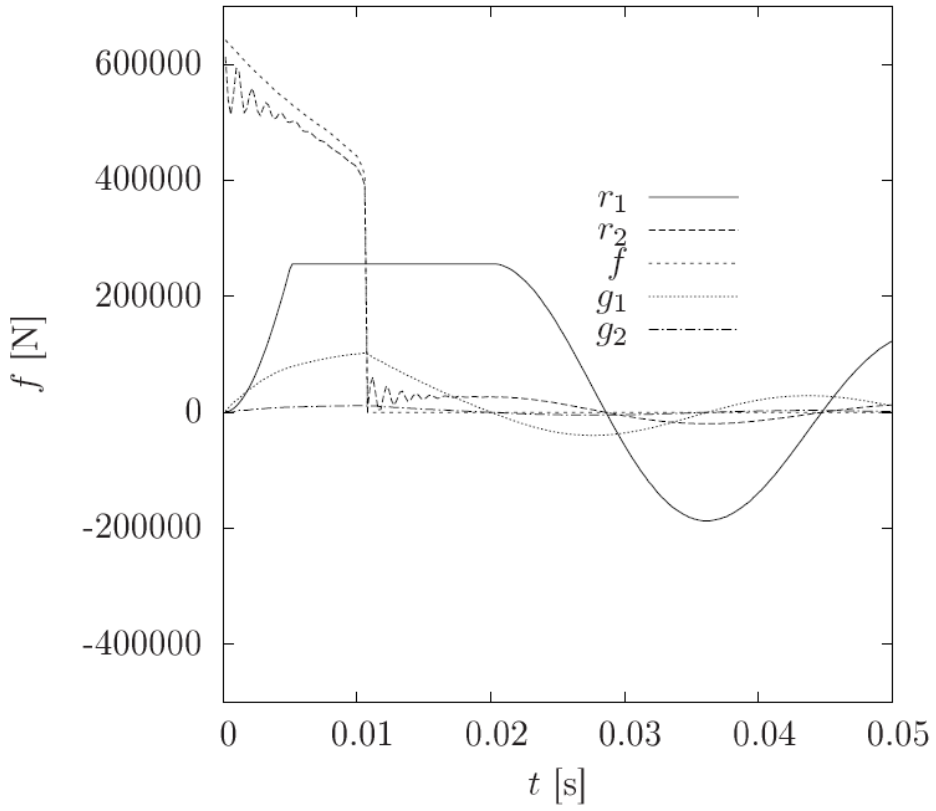

Figure 24. Forces of TDOF plate model of Test 642b with a non-diagonal damping matrix and v_0=109 m/s, α=40^o.

Dry aluminium missile Test 663 with an impact velocity of 129 m/s

Deflections of the TDOF plate model assuming a diagonal damping matrix are shown in Figure 25. The shear cone angle is varied from 30 to 40 degrees. Corresponding results by assuming a non-diagonal damping matrix are presented in Figure 26.

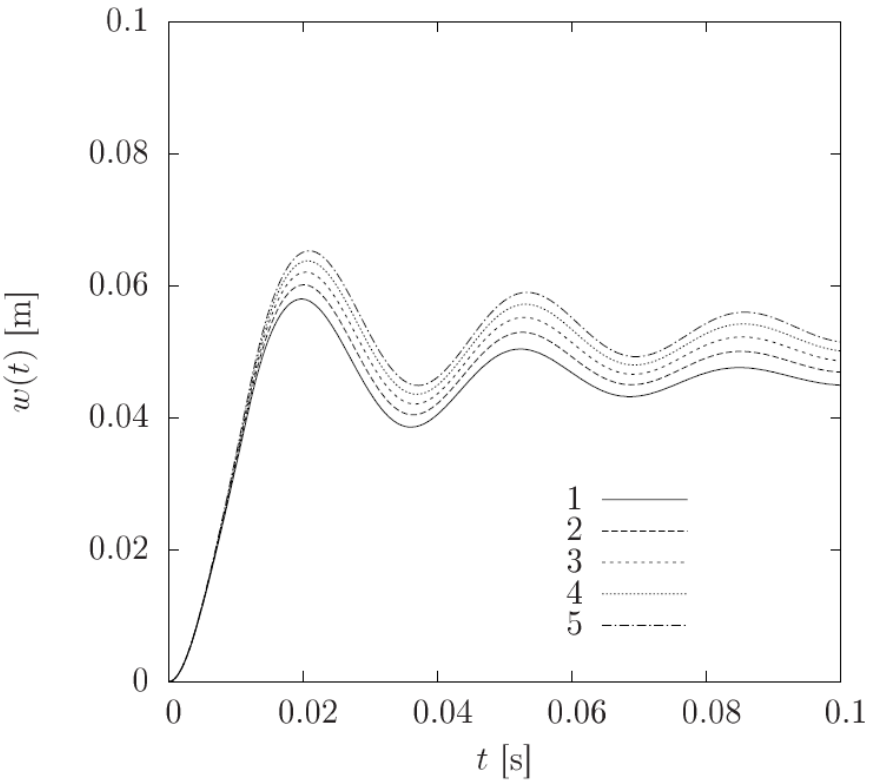

Figure 25. Deflection of TDOF plate model of Test 663 with a diagonal damping matrix and impact velocity of v_0 =129 m/s.

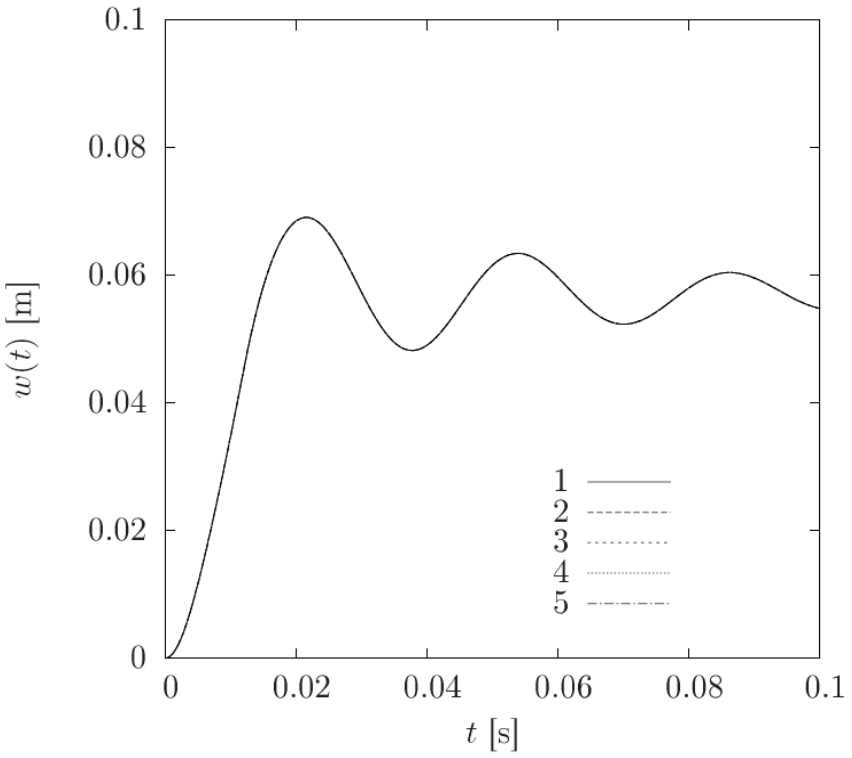

Figure 26. Deflection of TDOF plate model of Test 663b with a non-diagonal damping matrix and v_0 =129 m/s.

Dry aluminium missile Test 673 with impact velocity of 127 m/s

Figure 27 and Figure 28 depict the deflection of plate in Test 673 obtained with the TDOF model and assuming a non-diagonal damping matrix. Solutions with labels “ABQ-PL” and “ABQ-VP” are calculated with the damaged plastic concrete model offered by Abaqus and elasto-plastic (“PL”) or elastic viscoplastic model (“VP”) for the reinforcing steel. Figure 29 and Figure 30 show force histories in Test 673 calculated with a diagonal damping matrix and assuming shear cone angles of 30^o and 40^o. Test plate 673 was reinforced with stirrups.

Figure 31 depicts the corresponding force histories in Test 673 calculated with a non-diagonal damping matrix and assuming a shear cone angle of 30^o.

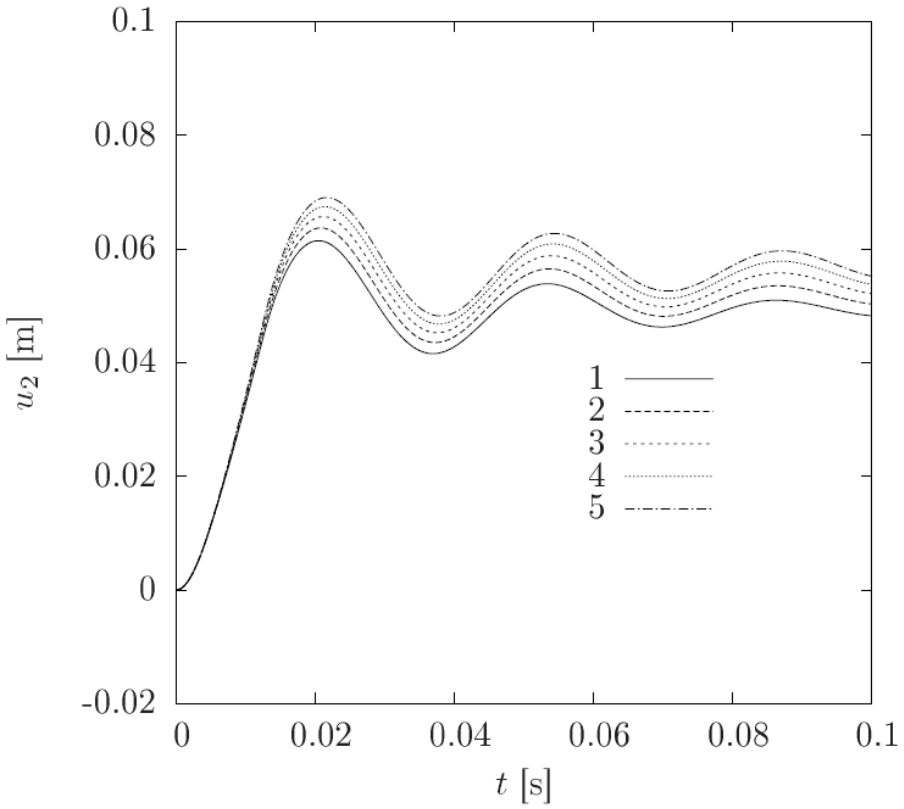

Figure 27. Deflection of TDOF plate model of Test 673 with stirrups, obtained with a diagonal damping matrix and impact velocity of v_0 =127 m/s.

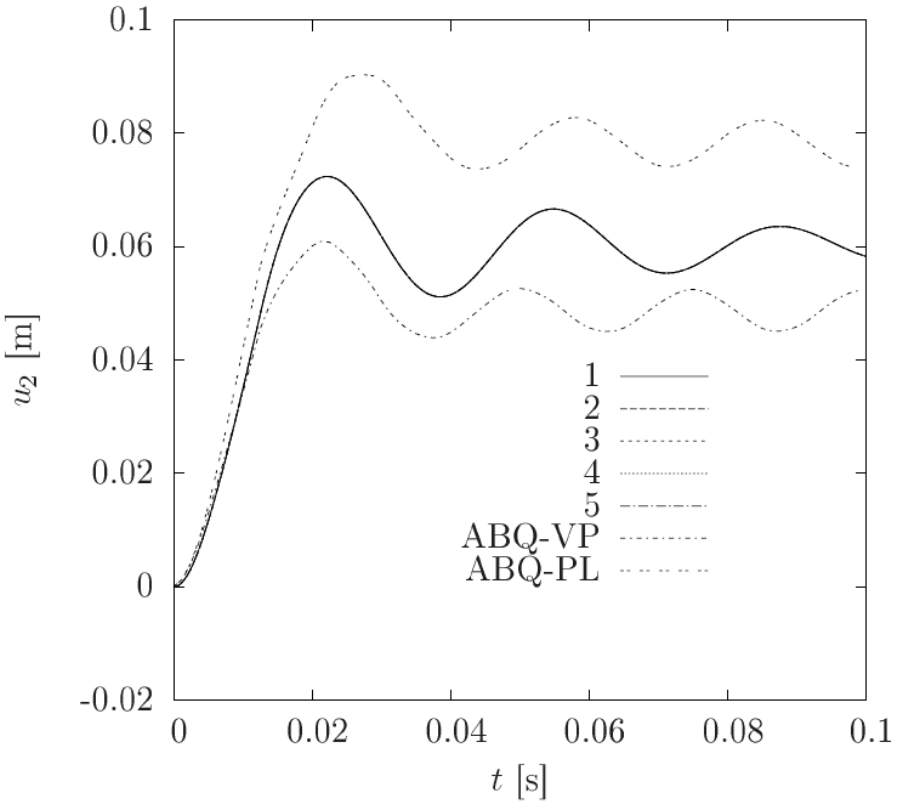

Figure 28. Deflection of TDOF plate model of Test 673b with stirrups obtained with a non-diagonal damping matrix for impact velocity of v_0 =127 m/s.

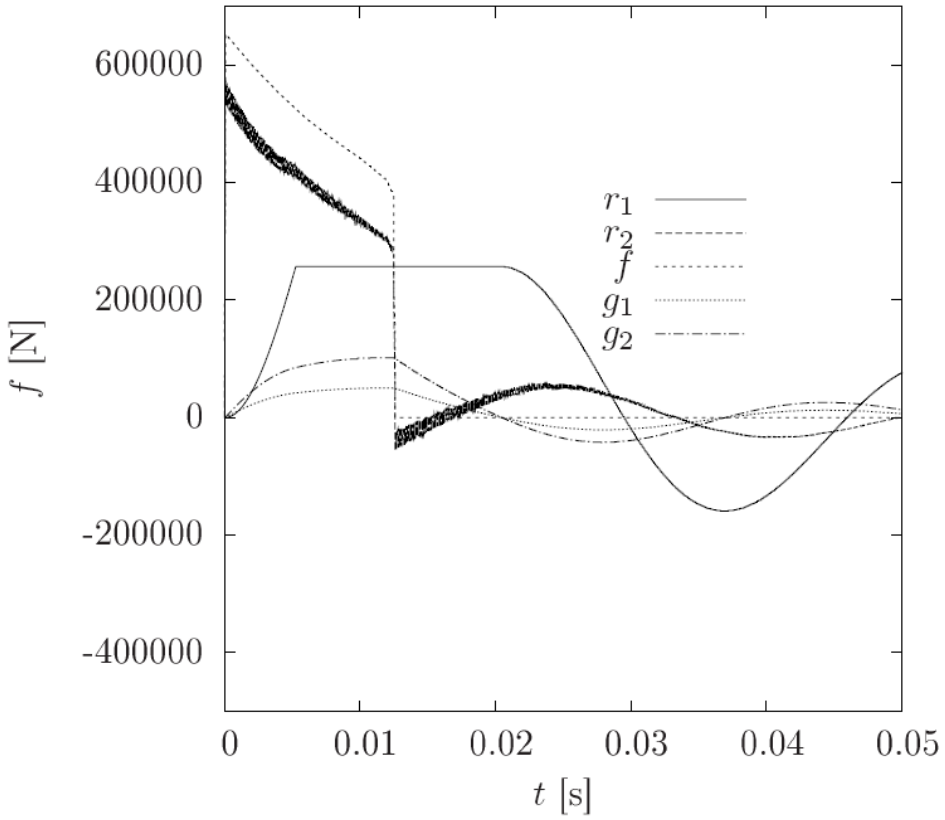

Figure 29. Force histories of TDOF plate model of Test 673 with a diagonal damping matrix for impact velocity of v_0 =127 m/s and α=30^o.

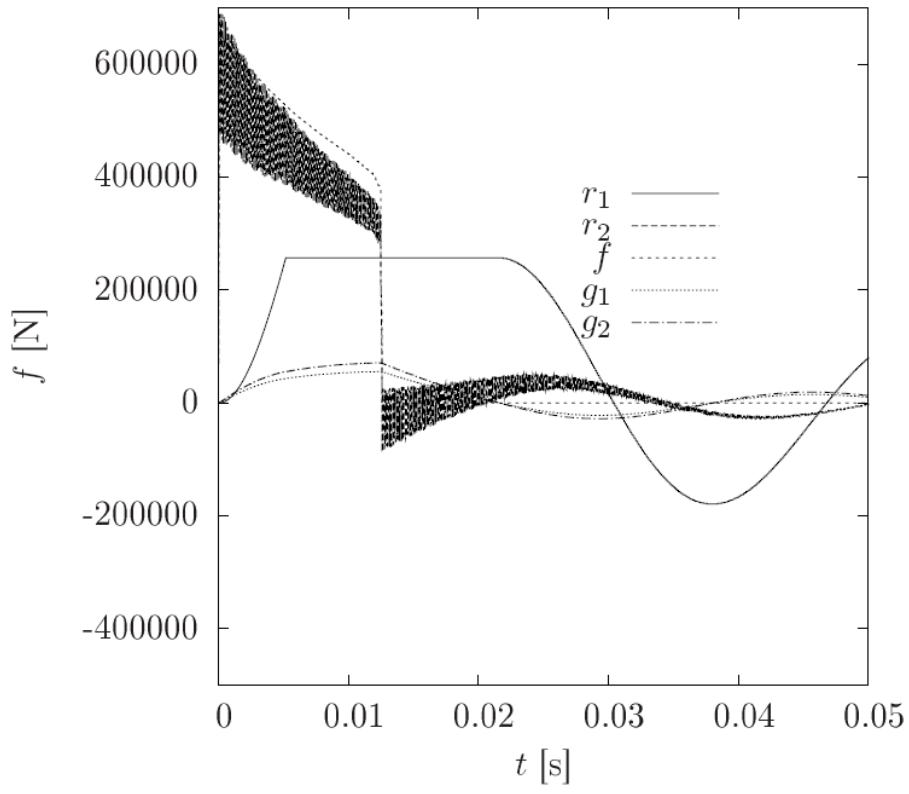

Figure 30. Force histories of TDOF plate model of Test 673 with a diagonal damping matrix for initial velocity of v_0 =127 m/s and shear cone angle of α=40^o.

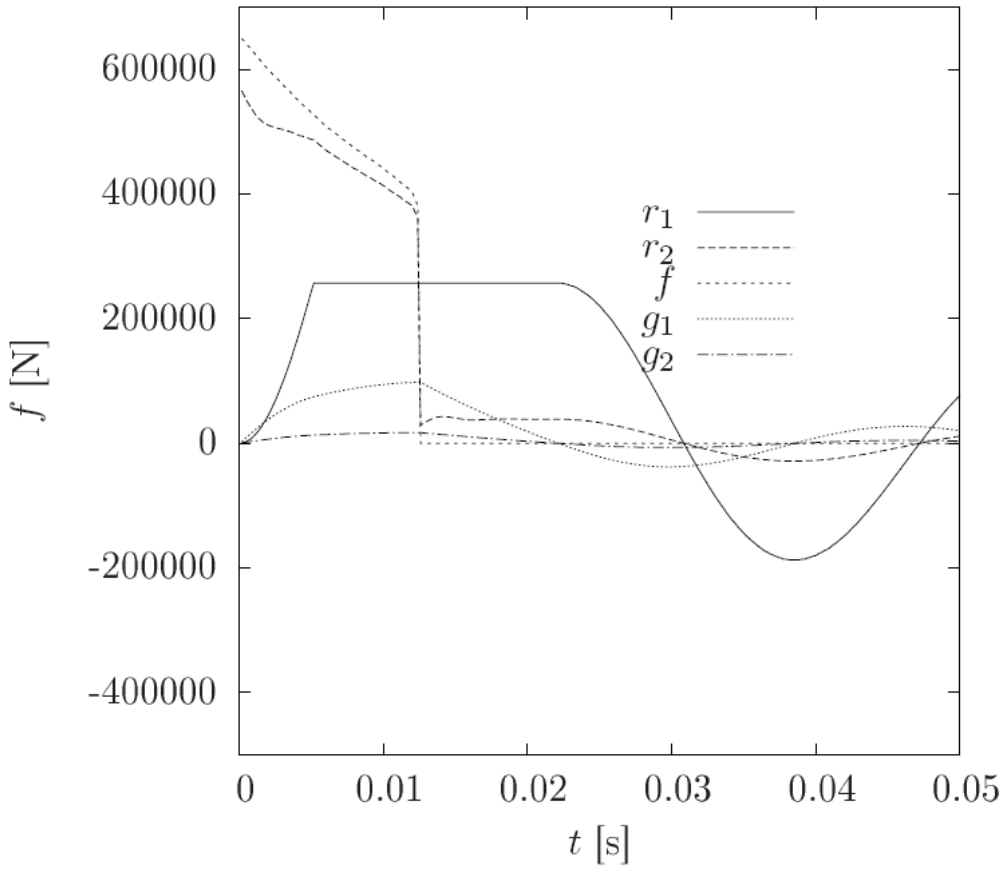

Figure 31. Force histories of TDOF plate model of Test 673b with a non-diagonal damping matrix for initial velocity of v_0=127 m/s and a shear cone angle of α=30^o.

The calculated main results of dry missile wall tests are collected in Table 3. The results calculated using a diagonal damping matrix with $\varsigma_1 = 5\%$ and $\varsigma_2 = 0.25\%$ and using a non-diagonal damping matrix with damping ratios $\varsigma_1 = 10\%$ and $\varsigma_2 = 1\%$ for dry missiles, are compared with each other.

Table 3. Comparison of main results of dry missile wall tests.

Test number	**Velocity [m/s]**	**Damping matrix**	**Disp. 1 [m]**	α_1	U_2 **[m]**	α_2	**Meas. disp. [m]**
642	109	diagonal	0.051	30	57	40	0.057
		non-diagonal	0.061	30	0.061	40	
663	129	diagonal	0.058	30	0.066	40	0.07
		non-diagonal	0.069	30	0.069	40	
673 (stirrups)	127	diagonal	0.061	30	0.067	40	
		non-diagonal	0.072	30	0.072	40	

3.3 Wet aluminium missile tests

Wet (water filled) aluminium missile tests are analysed using a two degree of freedom (TDOF) model assuming a diagonal damping matrix and alternatively a non-diagonal damping matrix (result option b). In the case of diagonal damping matrix the damping factors for masses 1 and 2 are $\varsigma_1 = 0.05$ and $\varsigma_2 = 0.0025$, while for non-diagonal damping matrix the damping factors are $\varsigma_1 = 0.1$ and $\varsigma_2 = 0.01$.The shear cone angle is varied from 30 to 40 degrees. Solution curves from "1" to "5" are connected to shear cone angles (from horizontal plane) of 30, 32.5, 35, 37.5 and 40 degrees, respectively.

Wet aluminium missile Test 644 with impact velocity 105 m/s

Figure 32 and Figure 33 show the deflection curves obtained by assuming different shear cone angles and using diagonal or non-diagonal damping matrices.

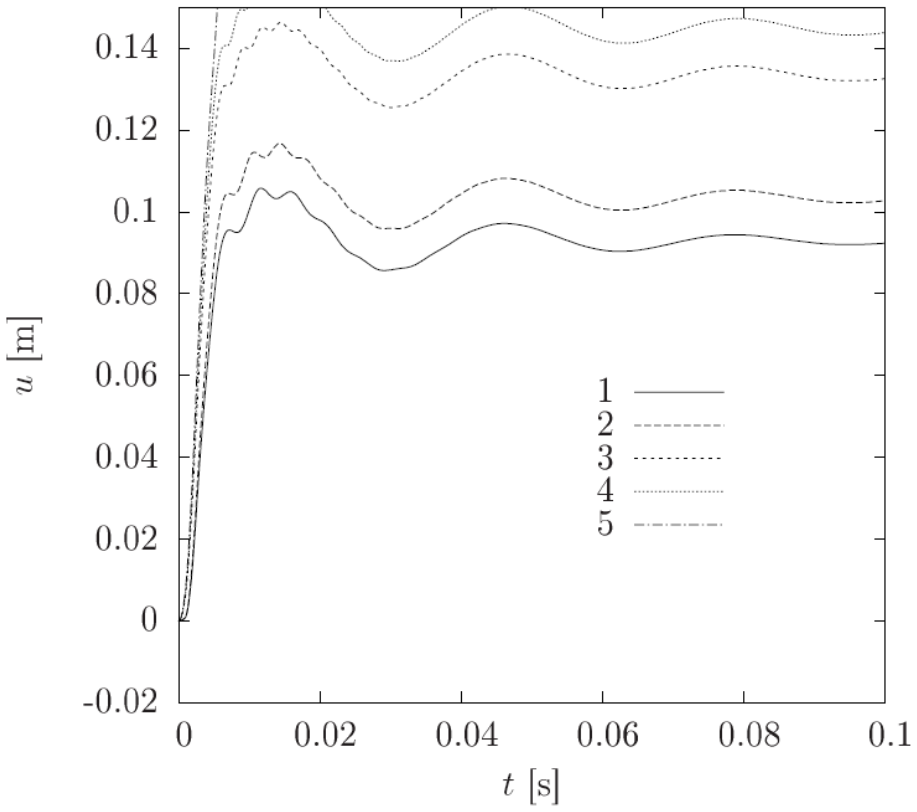

Figure 32. Deflection of the TDOF plate model with a diagonal damping matrix in wet aluminium missile Test 644 with impact velocity of v_0 =105 m/s.

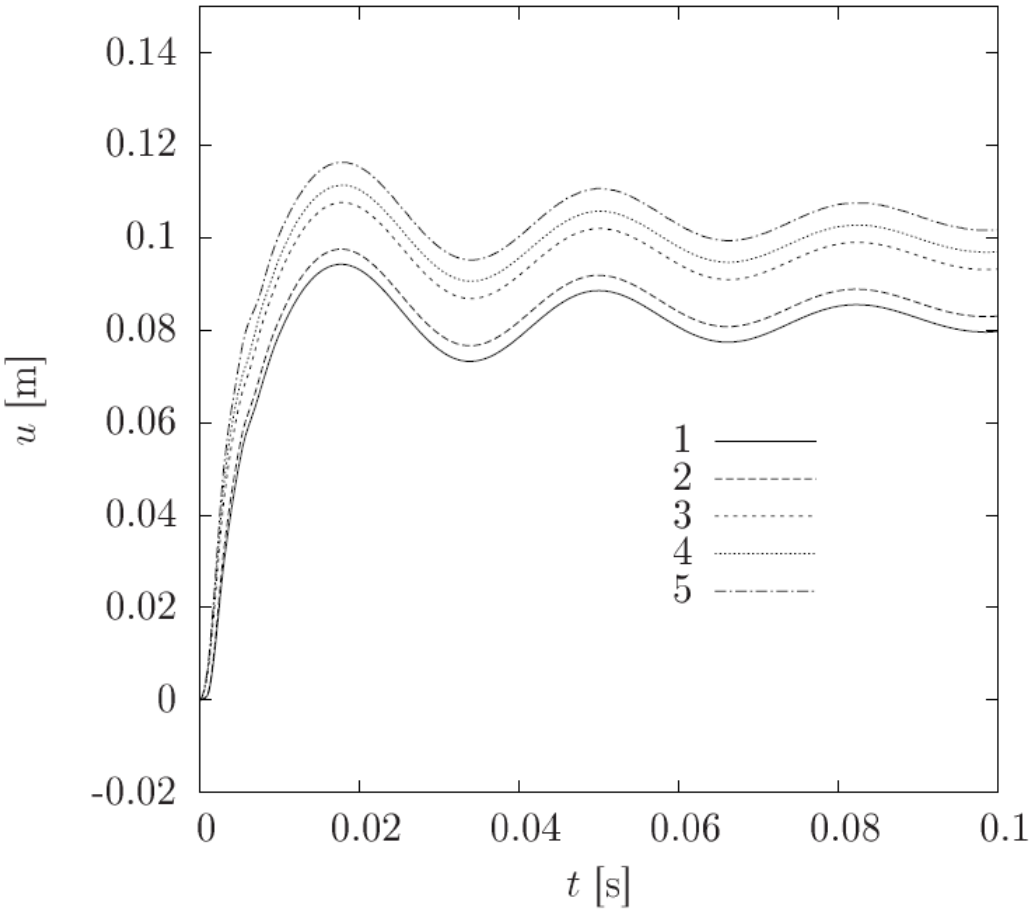

Figure 33. Deflection of the TDOF plate model with a non-diagonal damping matrix in wet aluminium missile Test 644b with impact velocity of v_0 =105 m/s.

The calculated main results of wet missile wall tests are collected in Table 4. The results calculated using a diagonal matrix with $\varsigma_1 = 5\%$ and $\varsigma_2 = 0.25\%$ and a non-diagonal damping matrix with $\varsigma_1 = 10\%$ and $\varsigma_2 = 1\%$ for wet missile are compared with each other.

Table 4. Comparison of main results of wet missile wall tests.

Test number	Velocity [m/s]	Damping matrix	u_1 [m]	α_1	u_2 [m]	α_2	Measured displacement [m]
644	105	diagonal	0.15	30	0.14	40	0.07, 0.08
		non-diagonal	0.094	30	0.116	40	

3.4 Punching capacity of concrete slab

The static punching capacity of a concrete slab can be obtained from the formula

$$F_p = 8170(\rho_p f_c)^{1/3} \pi d_e (d_{load} + 2.5 d_e),$$

where ρ_p [%] is the average percentage of reinforcement on the tensioned face, f_c [Pa] is the compression strength of concrete, d_e [m] is the distance between the front face and reinforcement and d_{load} [m] is the diameter of loaded area [Jowett, 1989]. The punching load as a function of slab thickness is presented in Figure 34 for concrete compression strength values of 60 MPa and 70 MPa.

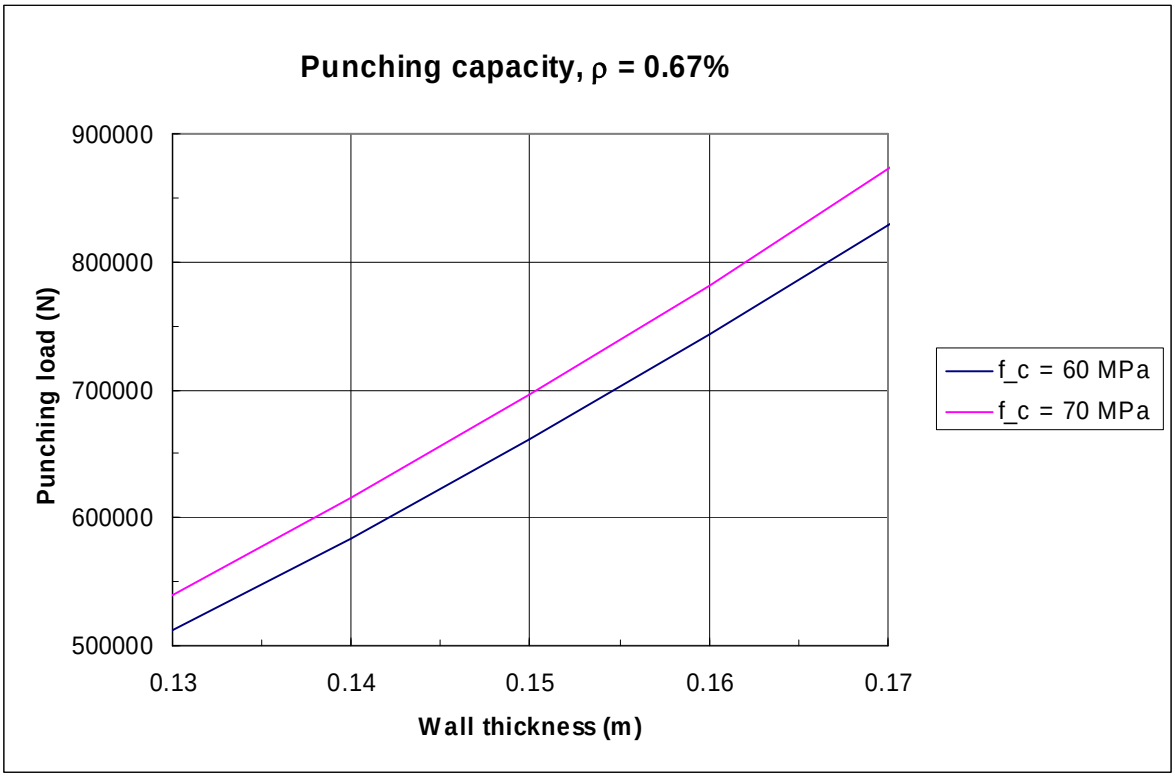

Figure 34. Punching load as a function of wall thickness.

According to Reference (Jowett, 1989), the static punching shear resistance formula can be applied for dynamic soft impact cases by checking the condition

$$\overline{F} \le F_p,$$

where $\overline{F}$ is the average value of the time dependent force resultant of the missile, and it can be calculated by

$$\overline{F} = \frac{0.9I}{t_{0.9I}},$$

where $t_{0.9I}$ is the time when 90% of the total impulse ($0.9I$) is reached during the dynamic loading transient. This means in practice that the possible long tail of the loading function $F(t)$ is discarded.

Average forces predicted for the impact tests are presented in Table 5. These values are calculated by dividing the impulse by the duration of the load transient. In Test 642, also the varied loading function is considered. According to these results, no punching is expected in Tests 642, 663 and 673. On the other hand, in Tests 644 and 650, punching is predicted.

Table 5. Average force due to impact.

Test	642	663	673	644	650
Impulse [Ns]	5630	6230	6400	5344.5	5292
Time [ms]	10.6 13	12.1	12.5	5.2	5.1
$\bar{F}$ **[MN]**	0.53 0.43	0.52	0.51	1.03	1.04
F_p **[MN]**	0.66	0.76	0.66	0.66	0.7

4 Impact tests with one-way 15 cm thick reinforced concrete walls

Nonlinear structural analyses of Tests 642 and 644 were carried out with Abaqus/Explicit code (Abaqus, 2007) and with a two degree of freedom (TDOF) model (ASCE, 1980). In addition, Test 642 was simulated with LS-DYNA FE code (LS-DYNA, 2003). All these models are described below. This chapter concentrates on structural analyses of Tests 642 and 644, but shows also some main results of several other tests with same type of 15 cm thick reinforced concrete walls.

Two types of missiles were used in those test series. The first type was an empty aluminium missile (often denoted as DRY) and it was used for instance in Test 642. The missile of the second type used for instance in Test 644 was shorter and filled with water (WET). The photographs of the missiles are shown in Figure 2 and their dimensions and other specifics in Figure 35. The main characteristics of all the public tests in these series are shown in Table 6. Notice that some of the tests are force plate tests without a concrete wall. The load time functions calculated using the Riera method and applied in the calculations for Tests 642, 644 and 673 are shown in Figure 36. The load curve of Test 663 is very similar to the one of Test 673. The load curve of Test 650 is very similar to the one of Test 644. Notice that two types of aluminium (Al1 and Al3) are used for the missile in these tests. The material choice affects the load time function.

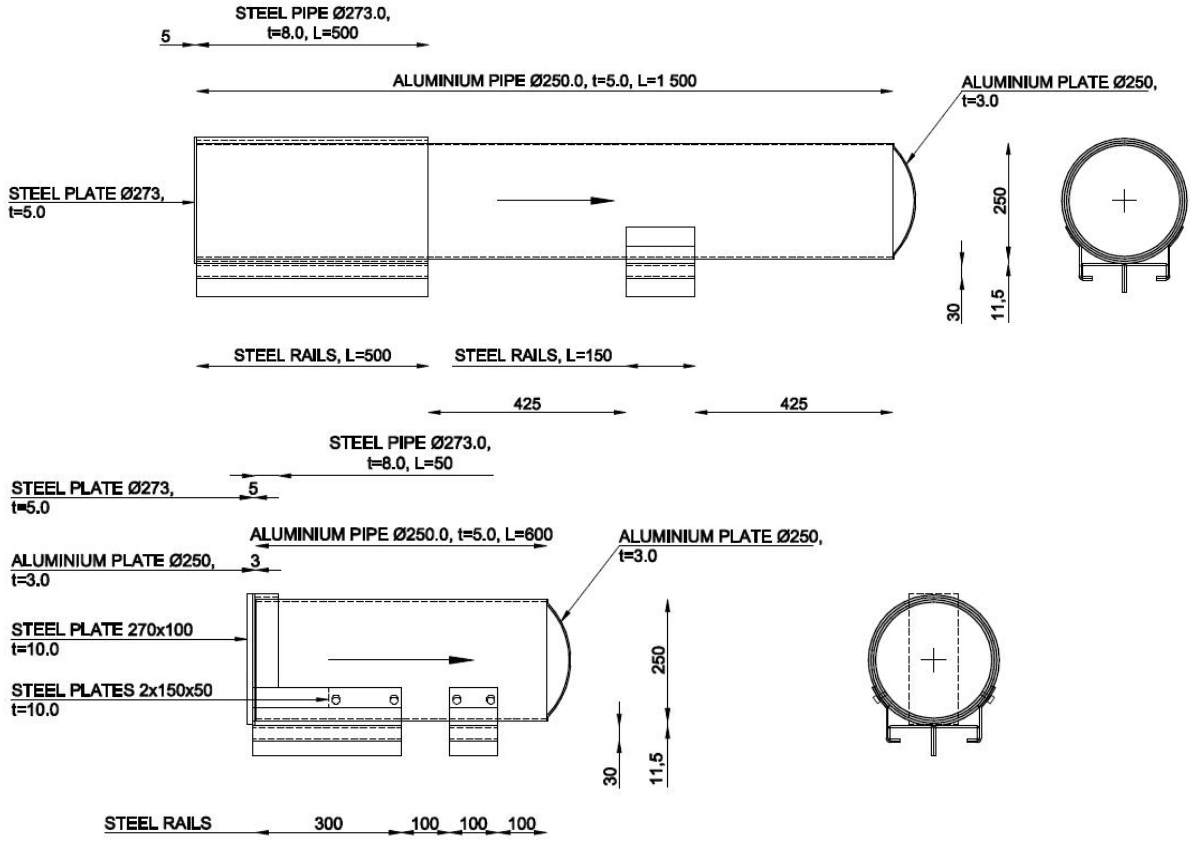

Figure 35. Aluminium pipe missiles of both types, the empty one above and the one filled with water below.

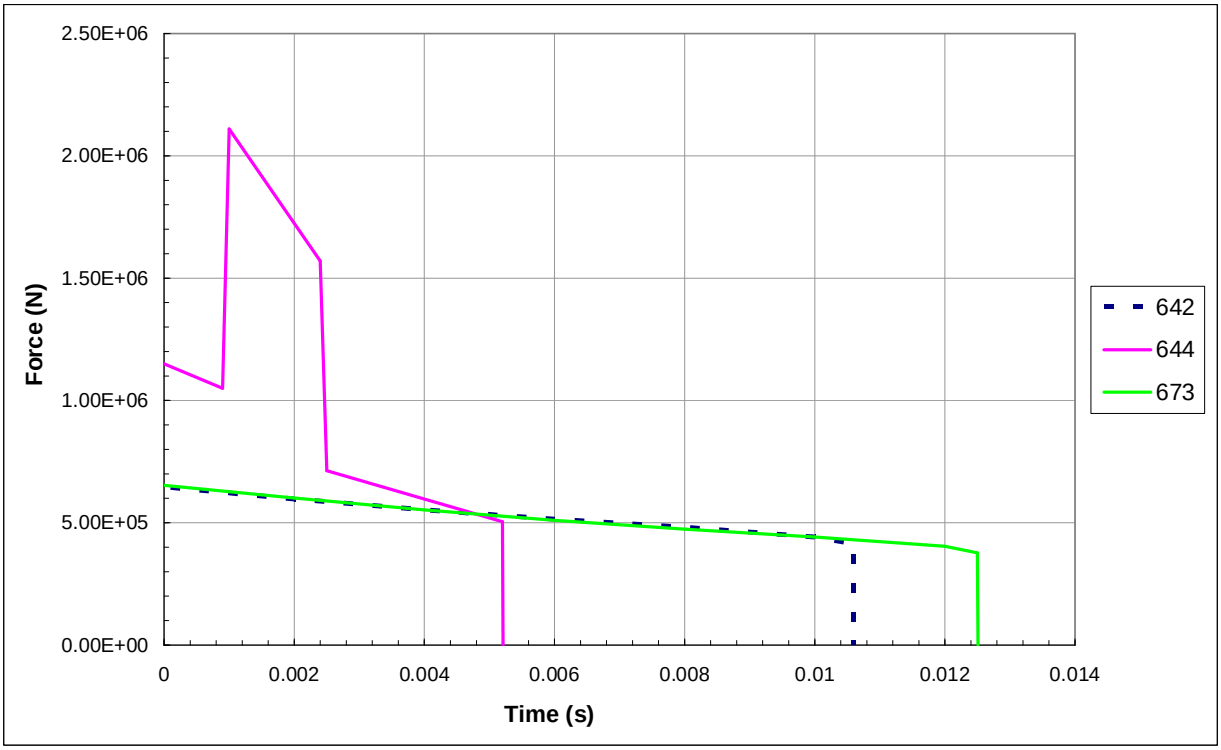

Figure 36. Load time functions for Tests 642, 644 and 673 calculated using the Riera method.

Table 6. Main characteristics and results of aluminium missile tests.

Test	Type of test	v_o [m/s]	m [kg]	Material of missile	L_o [1] [mm]	L_{cr} [2] [mm]	ΔL [3] [mm]	Comments
642	wall	109	51.5	Al1	1 500	800	700	DRY
637	f_plate	110	50.1	Al1	1 500	910 - 1 020	480 - 590	DRY
663	wall	129	48.2	Al3	1 800	1 000	800	DRY
673	wall	127	50.3	Al3	1 800	1 000	800	DRY, stirrups
661	f_plate	130	48.2	Al3	1 800	900	900	DRY
639	f_plate	150	57.5	Al1	1 500	700	800	DRY
644	wall	105	50.9	Al1	600	0	600	WET
650	wall	105	50.4	Al1	600	0	600	WET

[1] L_o is the initial length of the missile
[2] L_{cr} is the length of the missile after the test
[3] $\Delta L = L_o - L_{cr}$

The reinforced concrete wall type used in the impact tests is depicted in Figure 4, Figure 13 and Figure 37. The dimensions of the slabs in the test series are: width 2 m, length 2.3 m, support length 2.2 m and thickness 0.15 m. The slab was simply supported on two opposite vertical sides (dot-and-dash lines) and free on the two other sides. Locations of the displacement sensors were somewhat varied in different tests. The locations of the displacement sensors used in Tests 642 and 644 are shown in Figure 37. The locations of strain gauges in the reinforcement are shown in Figure 38. Locations of the strain gauges 1-8 were the same in all the tests. In Test 673 there were eight additional strain gauges (no. 9-16).

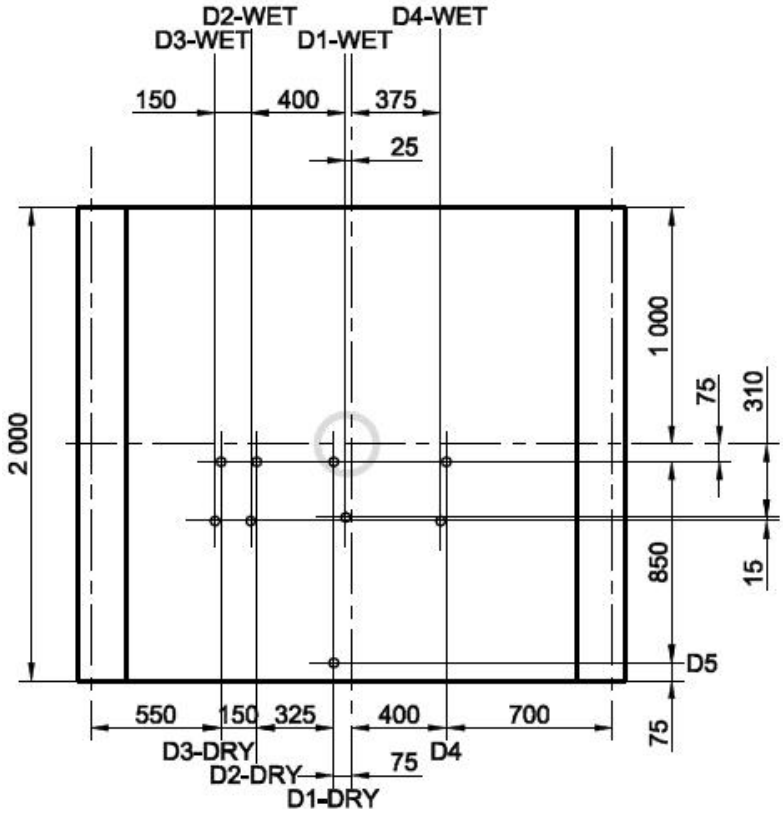

Figure 37. Instrumentation of the wall in Tests 642 (DRY) and 644 (WET): Displacement sensors are at locations D1-D5.

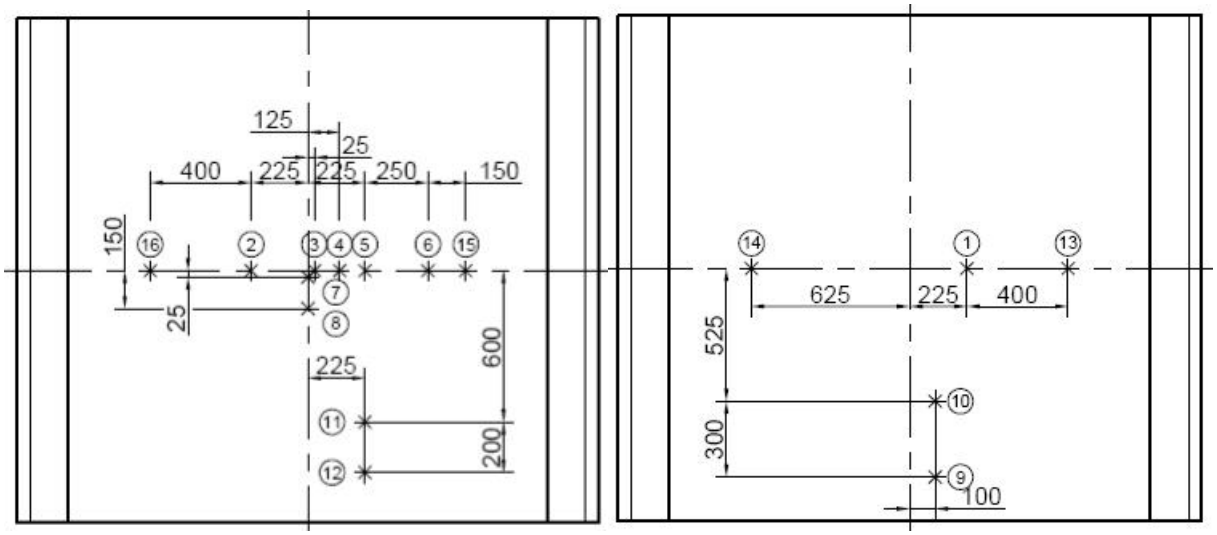

Figure 38. Strain gauge locations.

The slabs were reinforced using bars with a diameter of 8 mm and a spacing of 50 mm, in both directions and on both faces. The amount of reinforcement (on both the bottom and top faces) is $A_s = A_{st} = A_{sb} = 0.00100531$ m^2/m. The reinforcement ratio is in this case $A_s / h = 0.0067$ or $\rho_s = 0.67\%$.

4.1 Material properties

Material tests were carried out for every concrete casting. The measured material strength values are listed in Table 7. The tensile strength value was obtained by the Brazilian test. Material parameter values for the nonlinear finite element analyses are prepared based on these material test results.

Table 7. Measured material properties of concrete.

Material no.	Wall test no.	Young's Modulus [MPa]	Compressive strength [MPa]	Tensile splitting [MPa]	Tensile f_{ctk} [MPa]
1	642	31 000	58	2.85	3.04
2	663	30 000	65	4	3.28
3	673	27 000	59.5	3.6	3.1
5	650	30 000	70	3.35	3.45
6	644	31 000	61	2.8	3.15

4.1.1 Concrete in tension

The concrete tensile cracking strength can be calculated according to the Finnish standard BY50 (Suomen Betoniyhdistys, 2004) by the formula

$$f_{ctk} = \alpha K^{\frac{2}{3}},$$

where $\alpha = 58\varepsilon_{cu} \leq 0.2$ and K is the characteristic strength of concrete. For comparative reasons, tensile strength values calculated according to BY50 are also presented within these material test results.

For example in the case K = 60 MPa, the tensile strength is

$$f_{ctk} = 3.07 \text{ MPa}$$

and the corresponding elastic strain is

$$\varepsilon_{ctk} = 51 \cdot 10^{-6} \text{mm/mm}.$$

The smeared stress-strain curve of concrete in tension can be defined as

$$\sigma_1 = E_c \varepsilon_1, \ \varepsilon_1 \leq \varepsilon_{cr}$$

or

$$\sigma_1 = f_{cr} \left(\frac{\varepsilon_{cr}}{\varepsilon_1} \right)^{0.4}, \ \varepsilon_1 > \varepsilon_{cr},$$

where E_c is the modulus of elasticity of concrete, f_{cr} is the cracking stress of concrete and ε_{cr} is the cracking strain of concrete, (Wang and Hsu, 2001).

Nonlinear tensile stress-strain curves predicted according to the method in Reference (Wang and Hsu, 2001) using the measured tensile splitting strength values are presented in Figure 39.

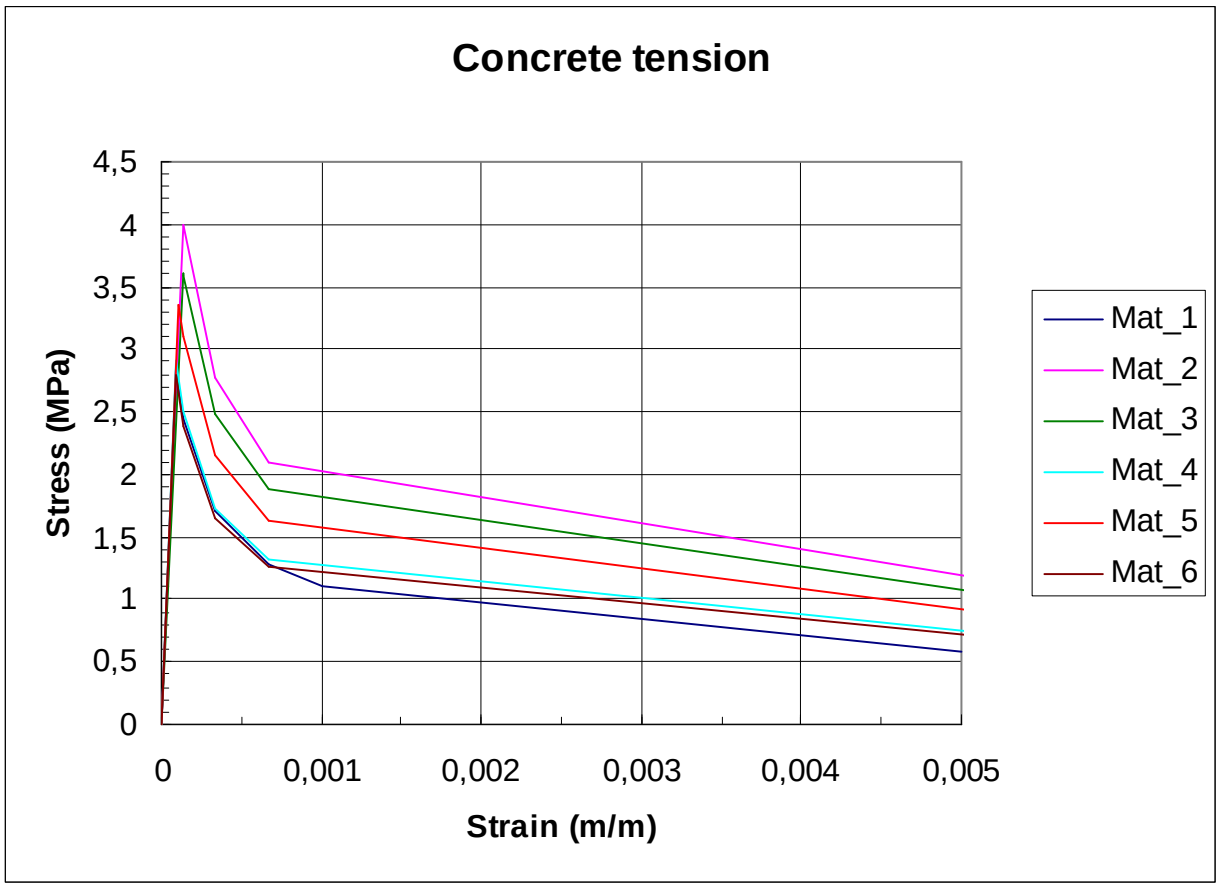

Figure 39. Tensile stress-strain behaviour of concrete material model.

For sensitivity studies, some additional analyses were carried out for Tests 642, 663 and 673 using modified tensile cracking properties. The modified tensile cracking material parameters were defined using the tensile strength value, f_{ctk}, instead of the tensile splitting strength value. These curves were further modified by setting the tensile strength to zero, when the tensile strain reaches the value of 0.67% (see Figure 40). Results calculated with this assumption are referred to as "f_{ctk_zero}".

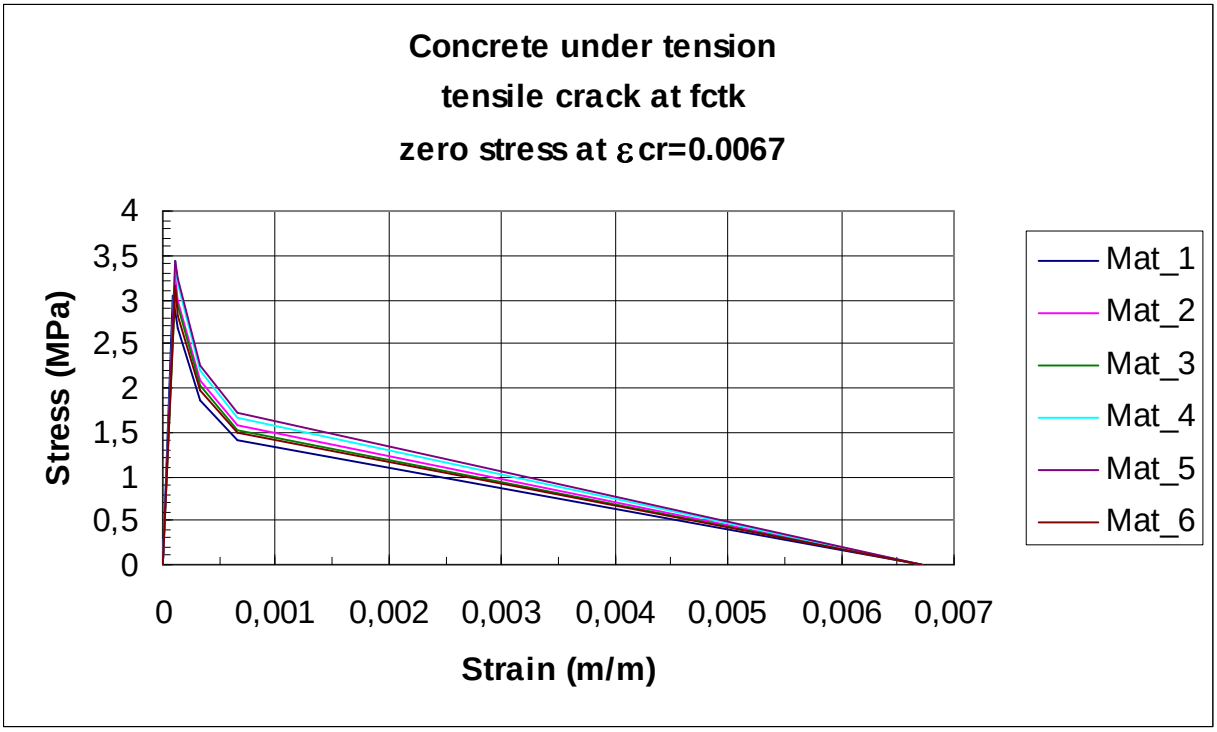

Figure 40. Modified material properties for tensile cracking.

4.1.2 Compression crushing properties for concrete material model

The ultimate compression strain, ε_{cu} , is according to BY50 (Suomen Betoniyhdistys, 2004)

$$\varepsilon_{cu} = (1.1 + \frac{\rho_c}{1000}) \cdot 10^{-3} \quad \leq \quad 3.5 \cdot 10^{-3}.$$

Assuming for the density of concrete ρ_c= 2500 kg/m^3, the ultimate compression strain becomes ε_{cu} = 3.5*10^{-3}. Nonlinear stress-strain curves in compression used in the analyses are presented in Figure 41.

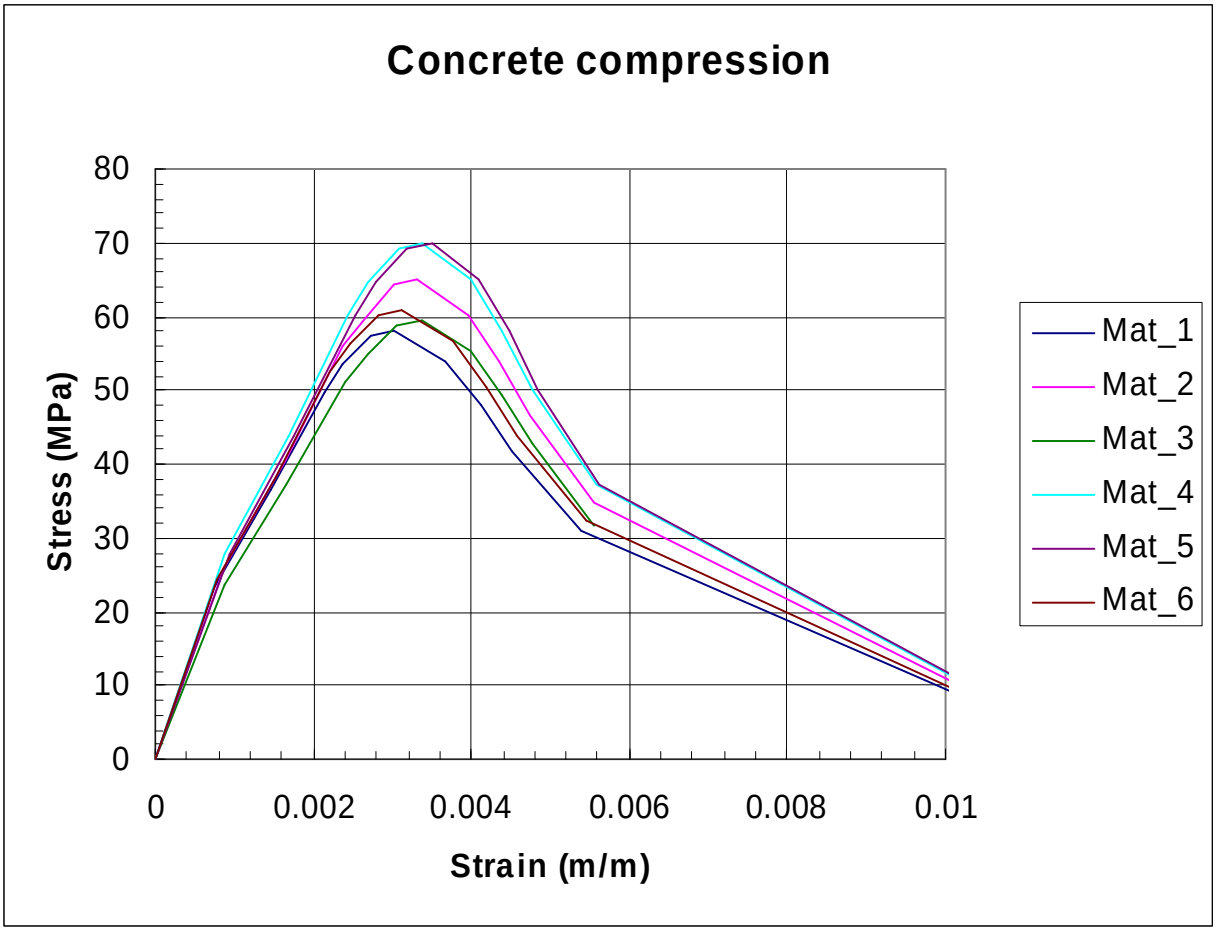

Figure 41. Concrete compression crushing behaviour.

4.1.3 Material properties of reinforcement steel

The use of the average (smeared) steel stresses in combination with the corresponding concrete stresses allows the tension stiffening effect (of steel bars by concrete) to be considered and deformations of the steel concrete composites to be correctly evaluated (Wang & Hsu, 2001). The stress in reinforcement is

$$\sigma_s = E_s \varepsilon_s, \quad \varepsilon_s \le \varepsilon_y$$

$$\sigma_s = f_y[(0.91 - 2B) + (0.02 + 0.25B\frac{\varepsilon_s}{\varepsilon_y})], \quad \varepsilon_s > \varepsilon_y,$$

where σ_s and ε_s are the average (smeared) stress and strain of mild steel bars in concrete, f_y and ε_y are the yield stress and strain of mild steel bars in concrete and E_s is the modulus of elasticity of reinforcement. The parameter B is defined by the formula

$$B = \frac{1}{\rho}\left(\frac{\sigma_{cr}}{\sigma_y}\right)^{1.5},$$

where ρ is the reinforcement ratio and it is greater than 0.5 %.

The stress-strain curves for reinforcement used in the nonlinear analyses are presented in Figure 42.

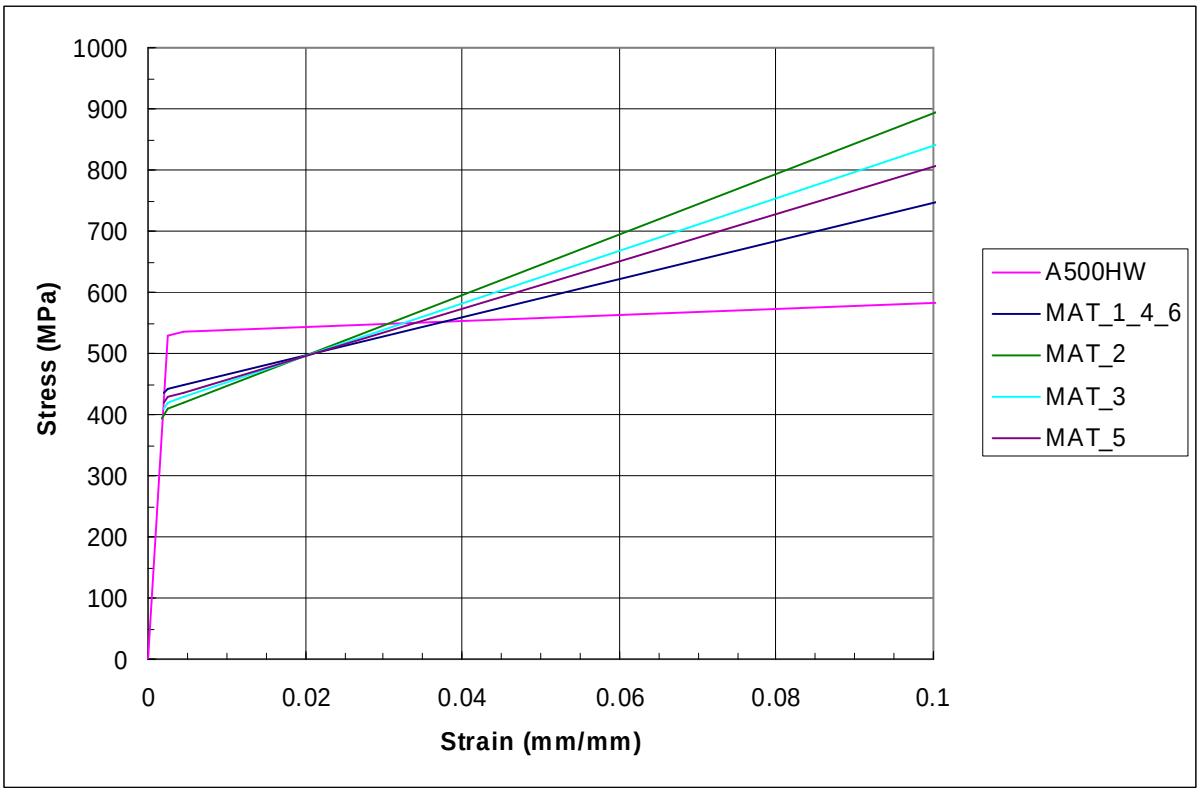

Figure 42. Stress-strain dependency for reinforcement steel.

The yield strength of reinforcement steel is highly strain rate dependent and increases when the strain rate increases. This dynamic yield strength of steel was taken into consideration by the Cowper-Symonds formula for uniaxial tension or compression.

$$\sigma_{yd} = \sigma_{ys}\left[1+\left(\frac{\dot{\varepsilon}}{D}\right)^{1/q}\right],$$

where $\sigma_{ys} \equiv \sigma_y$ and σ_{yd} are the static and the dynamic flow stress, respectively, and D and q are material parameters. For mild steel D = 40 1/s and q = 5 can be used, (Jones, 1989).

4.2 Finite shell element model of the wall

Nonlinear structural analyses were carried out with Abaqus/Explicit code (Abaqus, 2007). The finite element model for one quarter of the wall is shown in Figure 43. The reinforcement is modelled as smeared layers in the four-noded shell elements. There are two symmetry lines in the model. The upper edge of the model is free and the right hand side edge is simply supported. The loaded area is determined by assuming a load spreading angle of 45^{o} in the slab thickness direction. The load area is indicated by red colour.

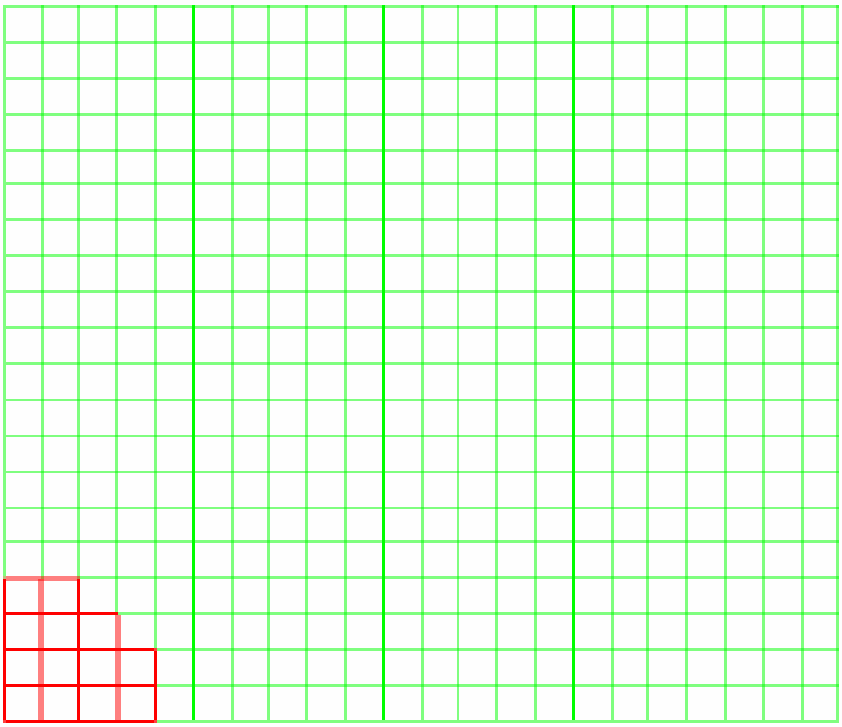

Figure 43. A quarter finite element model of the impact test walls.

4.3 Finite shell element model of the wall with supporting structure

A finite element model of the frame supporting the reinforced concrete wall was built in order to study the effects of the wall supporting frame to the behaviour of the wall and the measurements. When designing the frame, the aim was to construct as rigid support for the wall as reasonably possible. This way, the boundary conditions applied to the wall would be ideal.

The wall is supported by a steel frame that has been built from various beam profiles and plates. The frame is connected to a rock wall with long back pipes. In this simple study, the frame is modelled using linear beam and shell elements. The finite element mesh of the frame and the wall is shown in Figure 44.

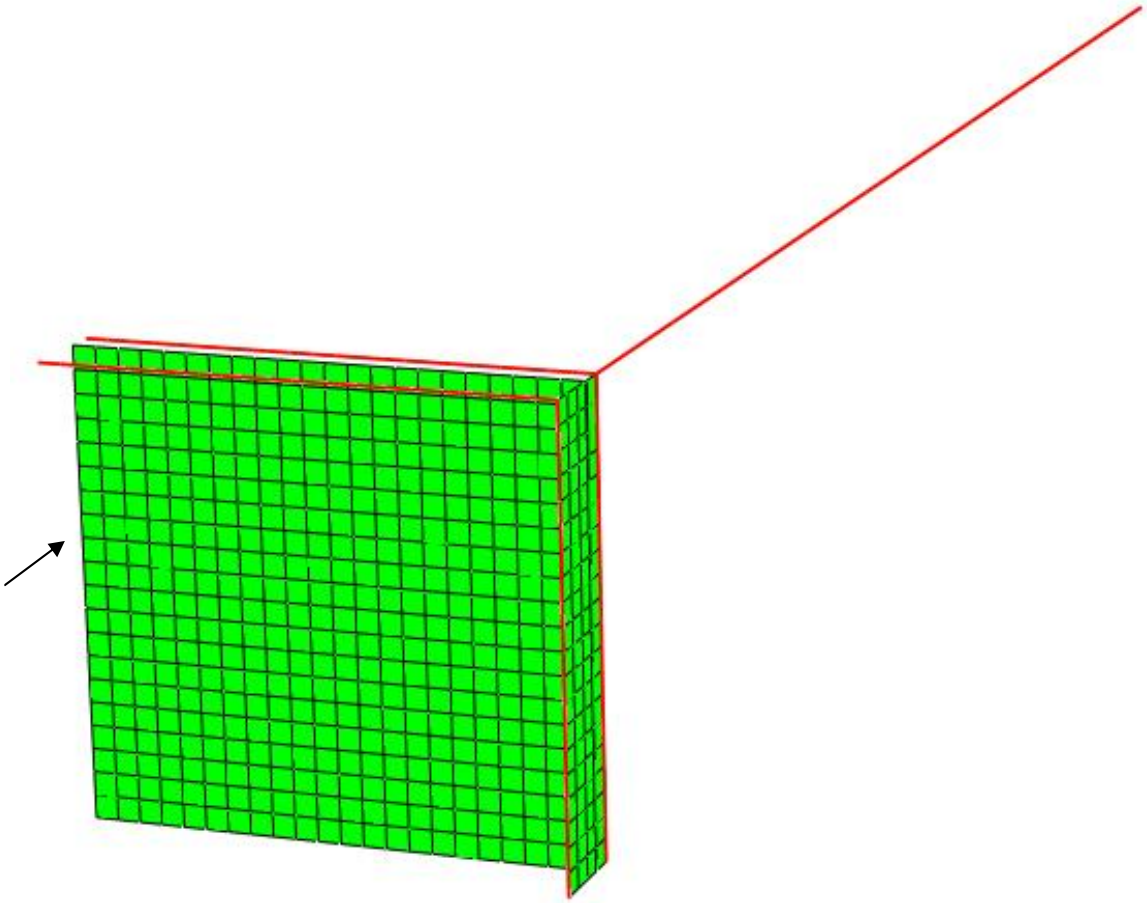

Figure 44. Element mesh of a quarter model of the wall and supporting frame. Shell elements are coloured green and beam elements are coloured red. The impact point is denoted by an arrow.

Appropriate symmetry boundary conditions are applied to the symmetry planes of the model. The free end of the back pipe is fixed. The wall is constrained in the impact direction by the frame using nonlinear connector elements so that the bending stiffness of only one side of the frame is associated with the boundary condition depending on frame deformation. That means that when the wall edge deforms in the impact direction it is supported by the back part of the frame. When the wall edge deforms against the impact direction, the front part of the frame supports the wall. These nonlinear connectors are located only on the right vertical edge of the wall. Connectors are not applied in the horizontal top edge since the frame does not constraint the vertical edges of the wall.

Section properties for the beams modelling the frame were calculated from the actual geometry of the frame so that the equivalent stiffness and mass to the frame were obtained. These calculated properties were assigned to the beam profiles. It is assumed that the frame does not experience plasticity during the impact and thus a linear elastic material model for the full frame is applied. Typical elastic properties for steel (elastic modulus 210 GPa and Poisson's ratio 0.3) are assumed. The front and back side of the frame are connected to each other with a plate. The plate is modelled using shell elements. The same linear material model for steel is applied. The back pipes are normal pipe profiles and are assumed to have the same elastic steel material property.

The reinforced concrete wall in the model is identical to the wall described in Section 4.2.

4.4 LS-DYNA model

A simulation of Test 642 was also carried out using LS-DYNA (version ls971d R3.1, revision 43919). Only a quarter of the wall was modelled. The model consisted of mainly solid brick elements (Figure 45). The rebars were modelled using beam elements (using strain rate dependent material properties). There were altogether 130 122 elements in the model. The wall was supported using two rigid bars. The Winfrith material model (smeared crack model) with strain rate effects was used in the simulations for the concrete material. The load area is indicated by white colour. The rebar ends in the symmetry plane can be seen in blue colour.

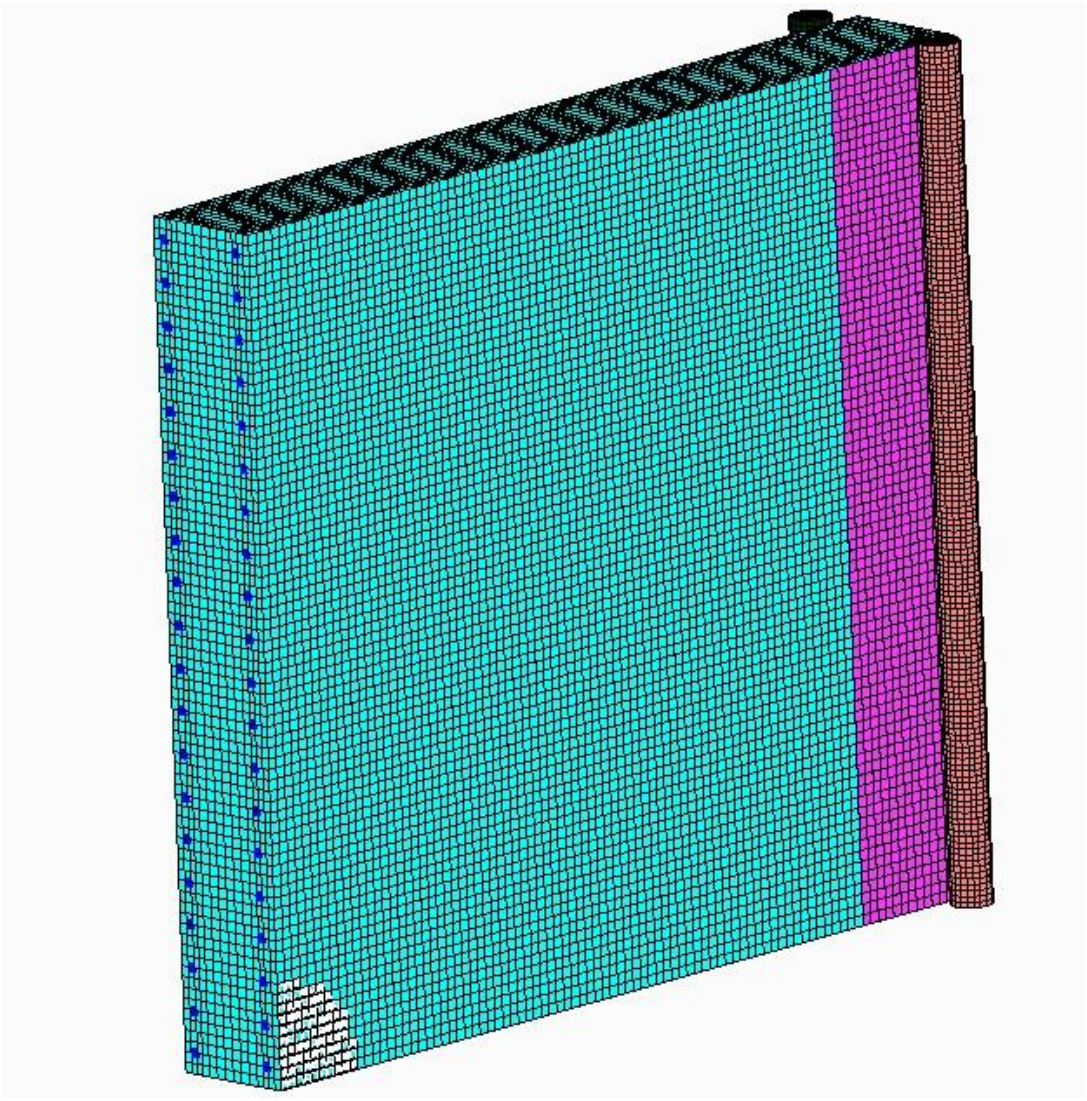

Figure 45. LS-DYNA solid element model.

The experiment was also simulated using a missile model as a load. In that model, there were altogether (both the wall and the missile) 143 222 elements (Figure 46). There are several ways in LS-DYNA to describe the fracture of a material. In the current study, the constrained tie-break method was used. In this method, the element edges are separated in order to describe crack propagation. The fracture of the aluminium tube was described by defining predetermined lines for the crack: the tube was sliced into longitudinal slices that were tied together with a failure criterion (plastic strain at failure of 30% was used). Figure 46 shows the missile and the wall right after the impact. The length of the missile was around 984 mm after the impact (original length was 1 504 mm). (LS-DYNA, 2003) (LS-DYNA, 2007).

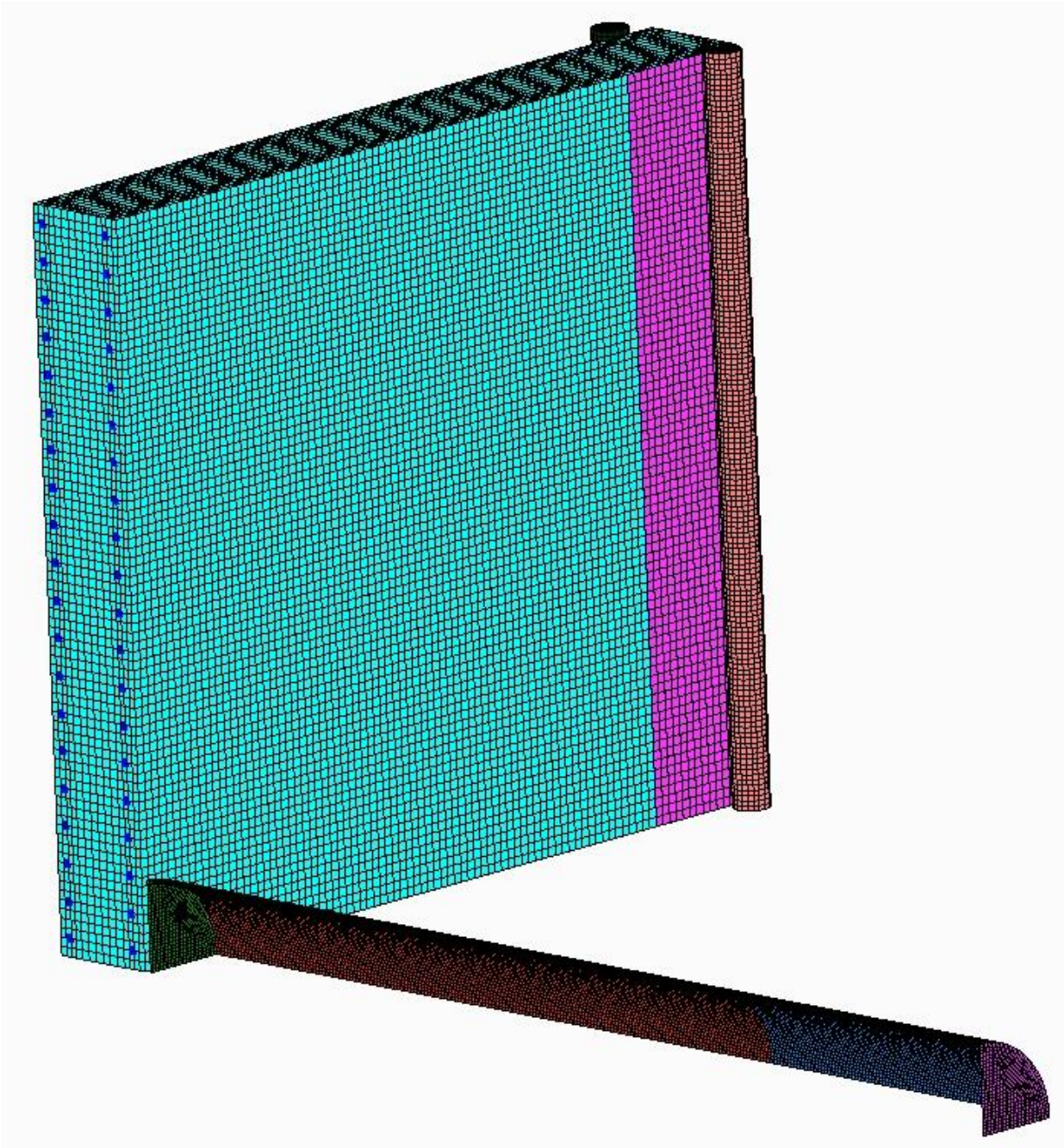

Figure 46. LS-DYNA solid element model with a missile.

4.5 Test 642

4.5.1 Shell element analyses of Test 642

Post test analysis for Test 642 was carried out with the FE model shown in Figure 43. The applied load function is presented in Figure 36 and the assumed nonlinear material parameters are presented in Table 7 and in Figure 39 to Figure 42. The energy balance during the analysis was maintained and it is shown in Figure 47. The energy balance can be considered maintained when ETOTAL is close to zero. This means that no energy is disappearing from the model or appearing to the model. The total energy balance is defined as

$$ETOTAL=ALLKE+ALLIE+ALLVD-ALLWK,$$

where ALLKE is kinetic energy, ALLIE is total strain energy, ALLVD is viscous energy and ALLWK is external work. Total strain energy is defined as a sum

$$ALLIE=ALLSE+ALLPD+ALLAE+ALLDMD,$$

where ALLSE is recoverable strain energy, ALLPD is energy dissipated by rate independent and rate dependent plastic deformation, ALLAE is artificial strain energy associated with constraints used to remove singular modes (such as in hour glass control) and ALLMD is energy dissipated by damage.

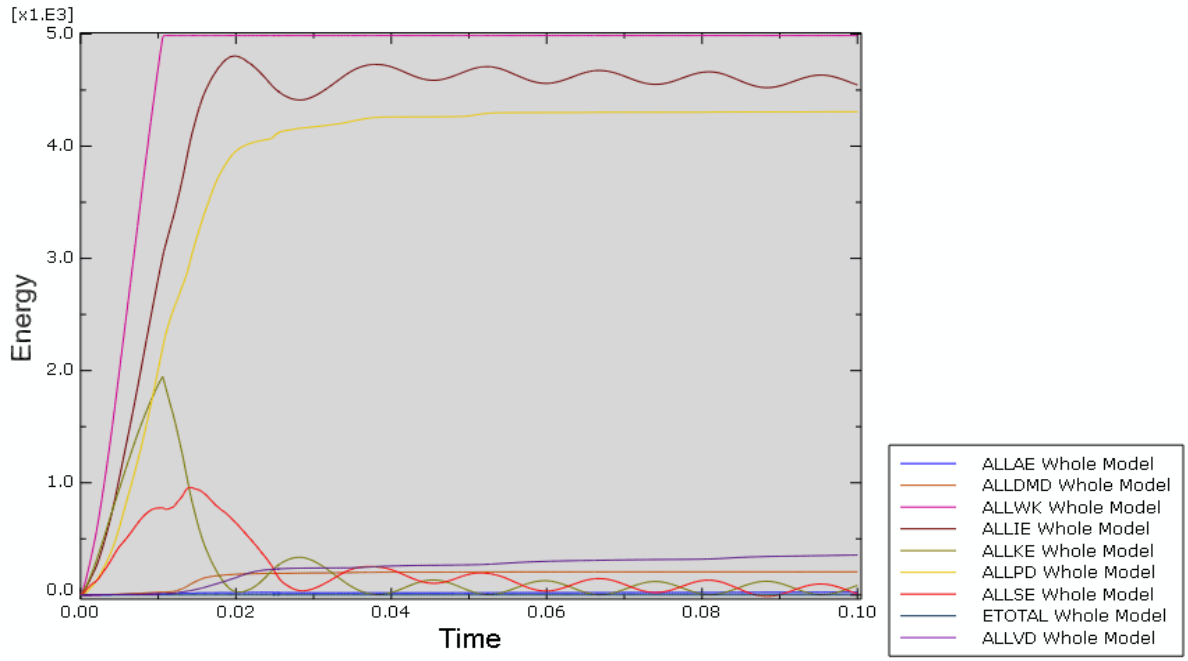

Figure 47. Energy balance during the calculation in Test 642.

The measured and calculated displacements as a function of time are presented in Figure 48. The measured and calculated values for strains in reinforcement are shown in Figure 49 and Figure 50. The displacement values were predicted quite well with the FE calculations. The maximum strain value occurs in the back surface horizontal reinforcement. The calculated maximum value is reasonably close to the measured strain value (see BH3 in Figure 49). It

should be noted that the strains in reinforcement are rather localized. Figure 51 shows the calculated rebar strains at the measurement locations. These numerical results are in agreement with the experimental observations.

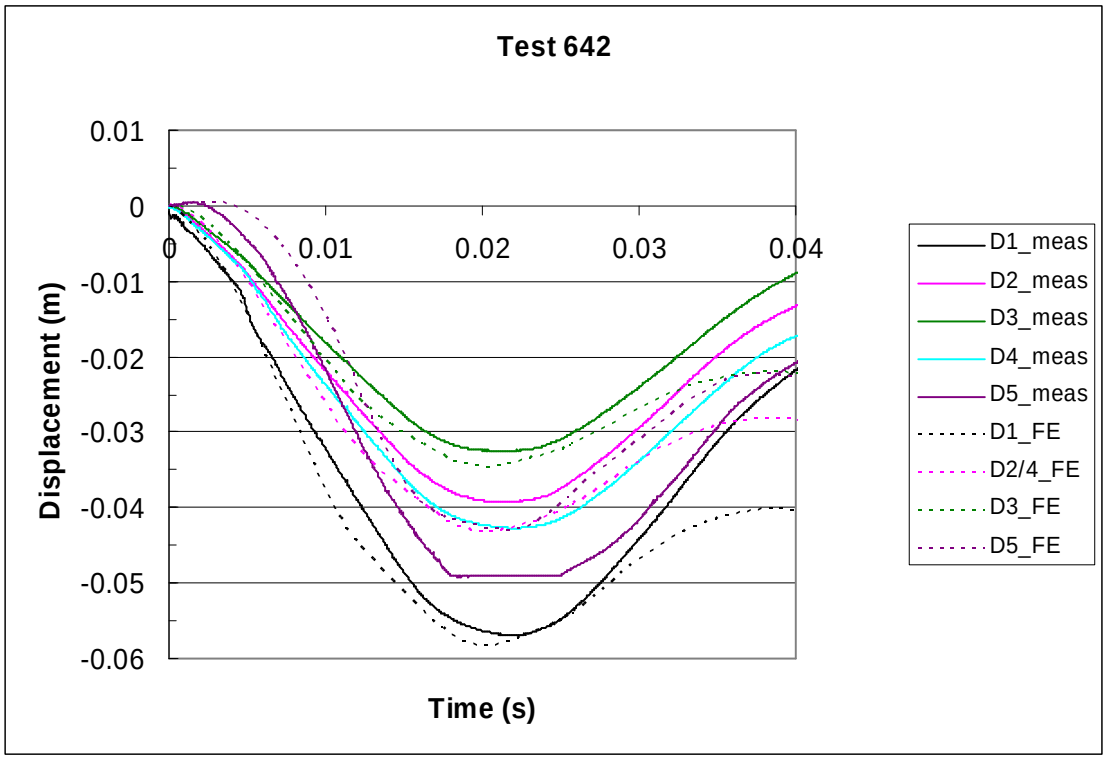

Figure 48. Measured and calculated displacements as a function of time in Test 642.

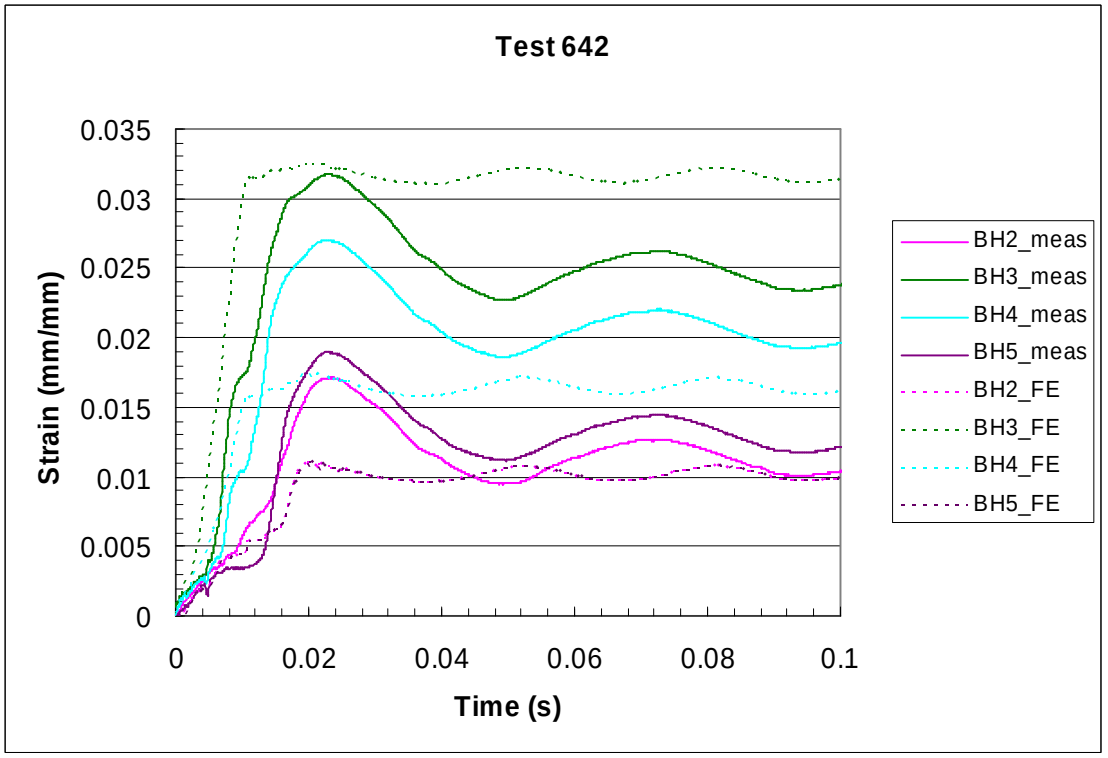

Figure 49. Measured and calculated strains in the reinforcement at BH2-5 in Test 642.

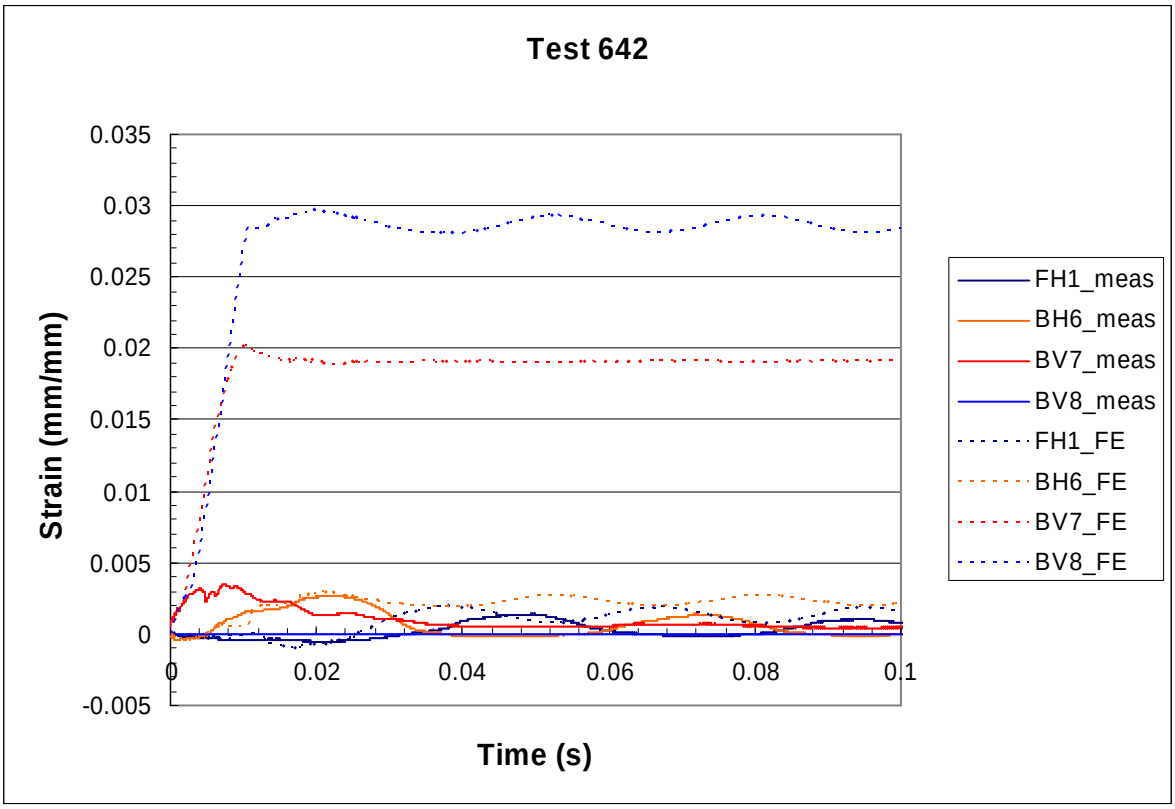

Figure 50. Measured and calculated strains in the reinforcement at FH1, BH6 and BV8 in Test 642.

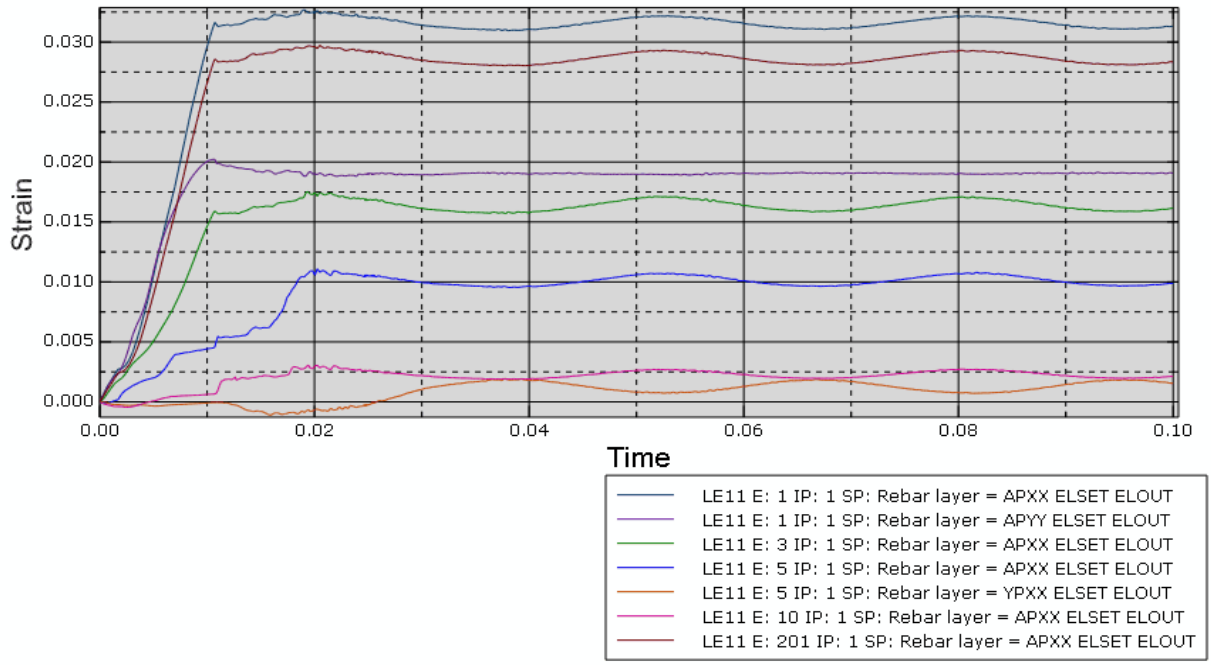

Figure 51. Calculated strains in reinforcement in Test 642.

The enveloped SDEG (Scalar stiffness degradation variable) contour in Figure 52 shows an idea of degradation of the wall after impact. No spalling or scabbing was observed in this test. After the test, a sample specimen was bored from the wall centre. At the middle of the span width, the cross section was tensile cracked until the front surface reinforcement. This can clearly be seen in the sample specimen bored from the centre of the tested wall in Figure 53. A quarter section of the test wall cut at the centre line is shown in Figure 54. Also X-ray photographs were taken of the same specimen. Photographs from four different angles at even intervals around the circumference are shown in Figure 55 (taken by Pieti Marjavaara at VTT).

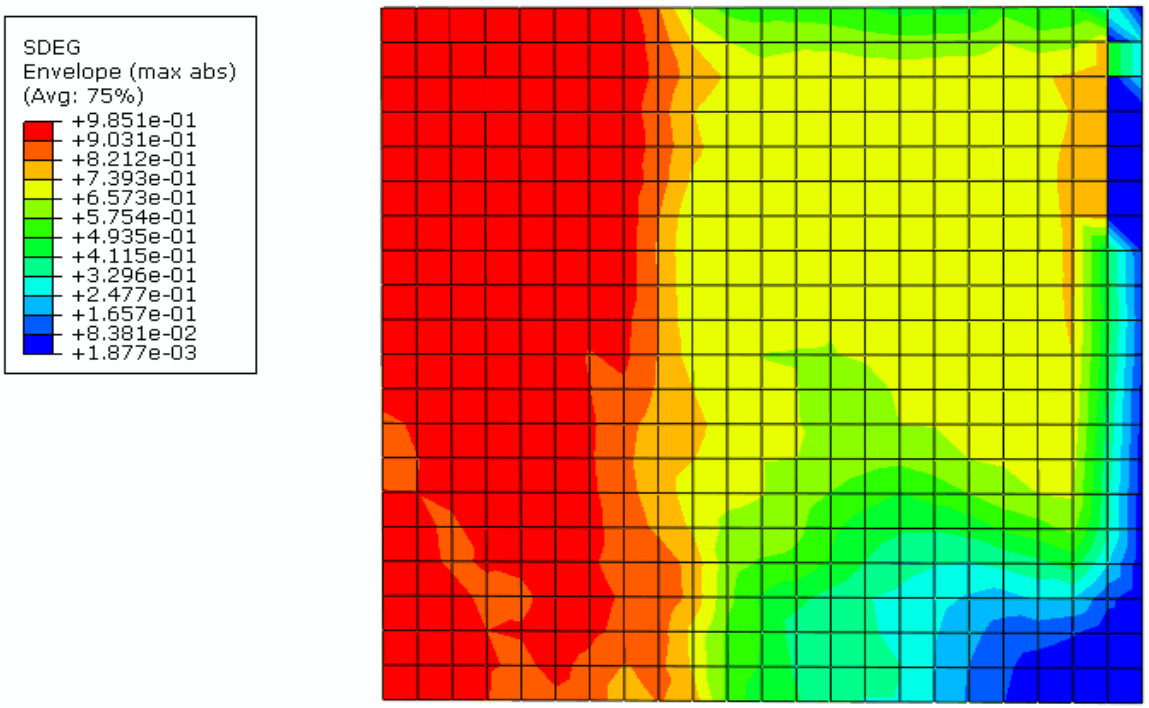

Figure 52. Enveloped SDEG distribution.

Figure 53. Sample specimen bored from the test wall 642.

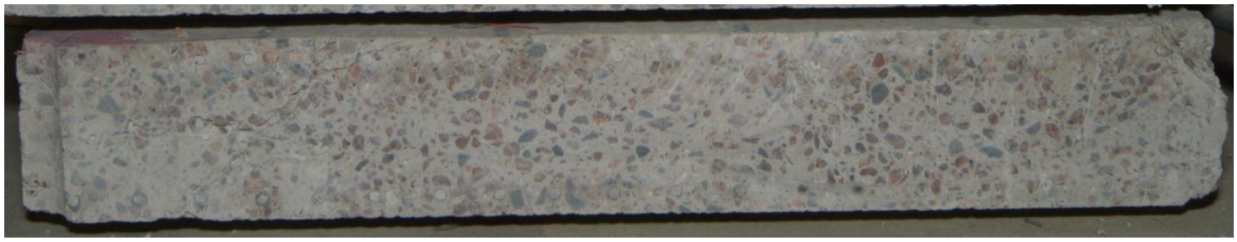

Figure 54. Quarter section of the test wall 642 cut at the centre line.

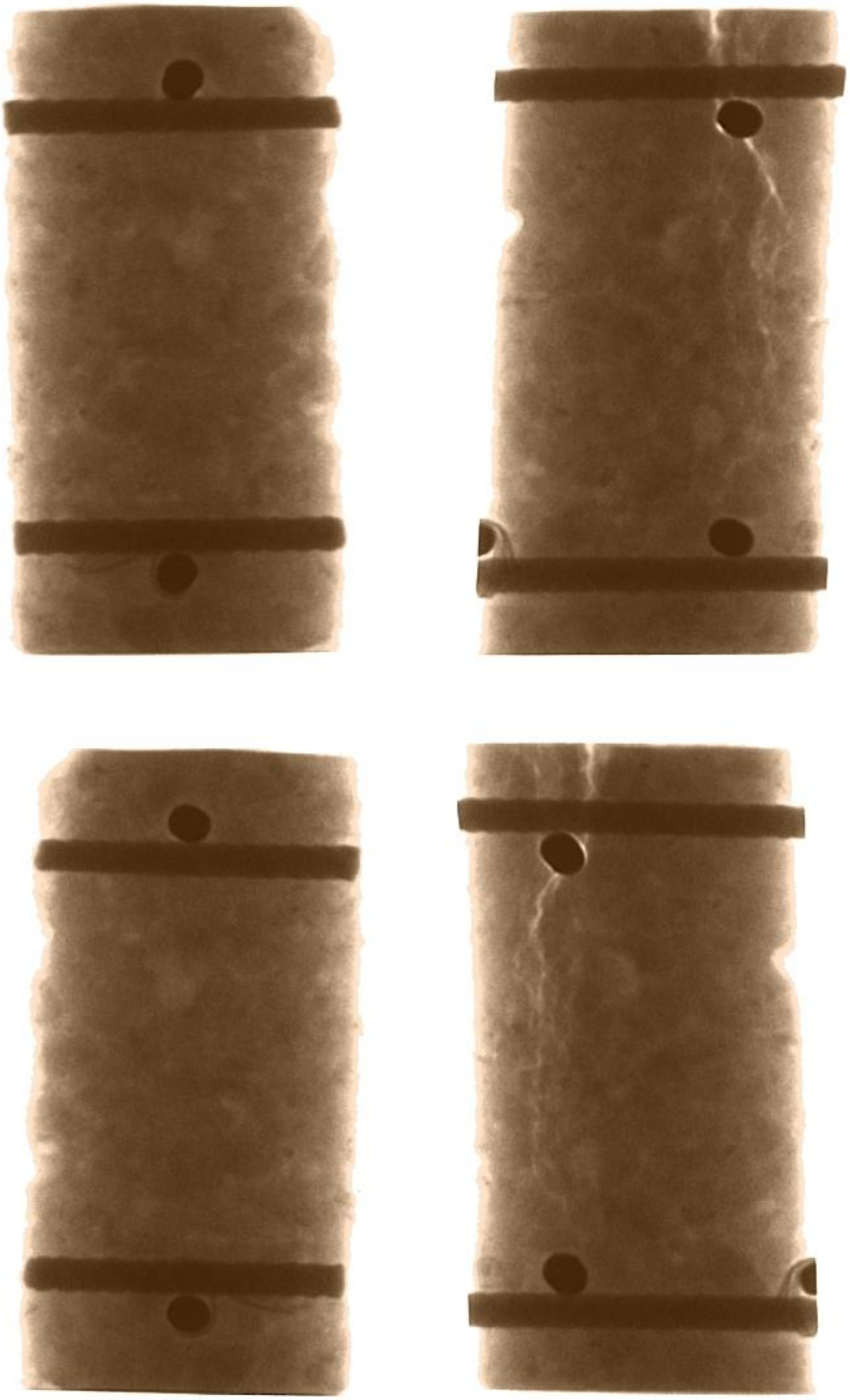

Figure 55. Sample specimen bored from the test wall 642 from four different angles at even intervals around the circumference.

Sensitivity studies with modified material parameters for Test 642

Deflections calculated with tensile stress–strain dependency, presented in Figure 40, are shown with the corresponding measured data in Figure 56. The calculated deflections are still quite close to the measured values, though they are somewhat larger than the displacements presented above.

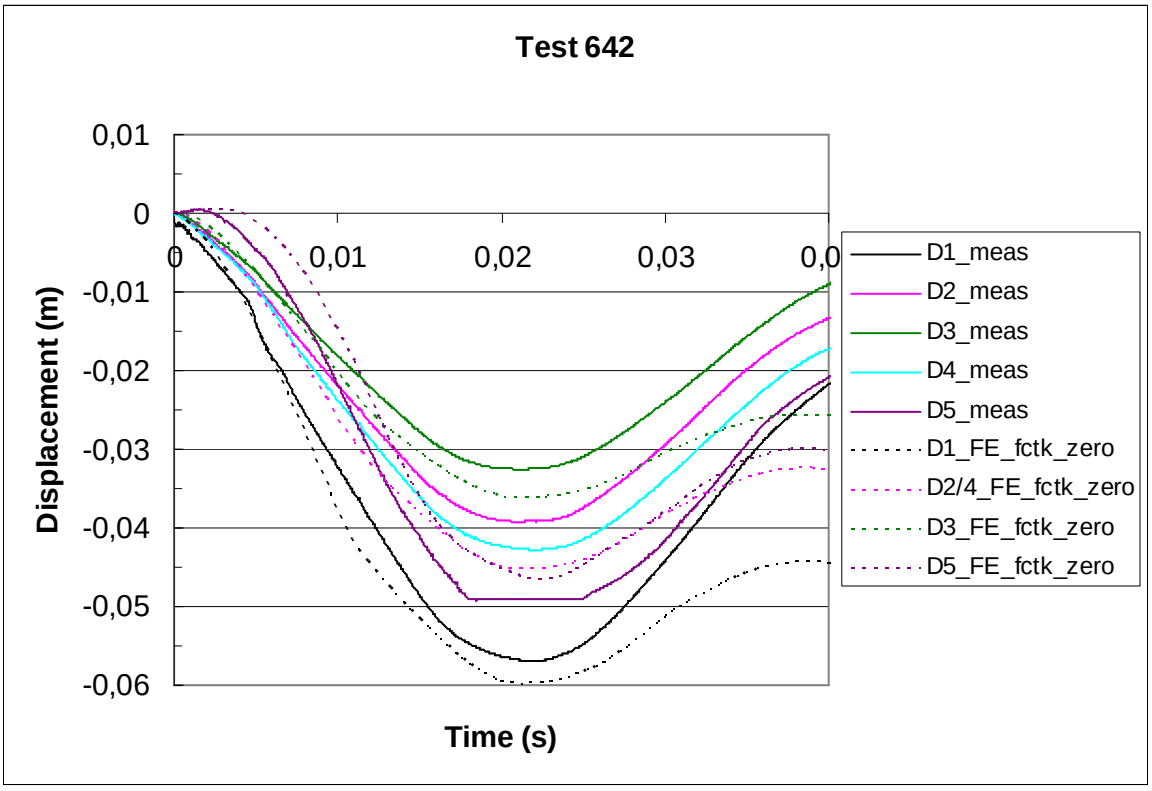

Figure 56. Measured and calculated deflections in Test 642.

Sensitivity studies with modified load for Test 642

Modified load functions were predicted by varying the assumed yield stress of aluminium. Force-time functions calculated with varied yield strength values are presented in Figure 57 and the corresponding crushed lengths of the missile can be seen in Figure 58. Then the impulse produced by these load functions is the same, 5600 Ns.

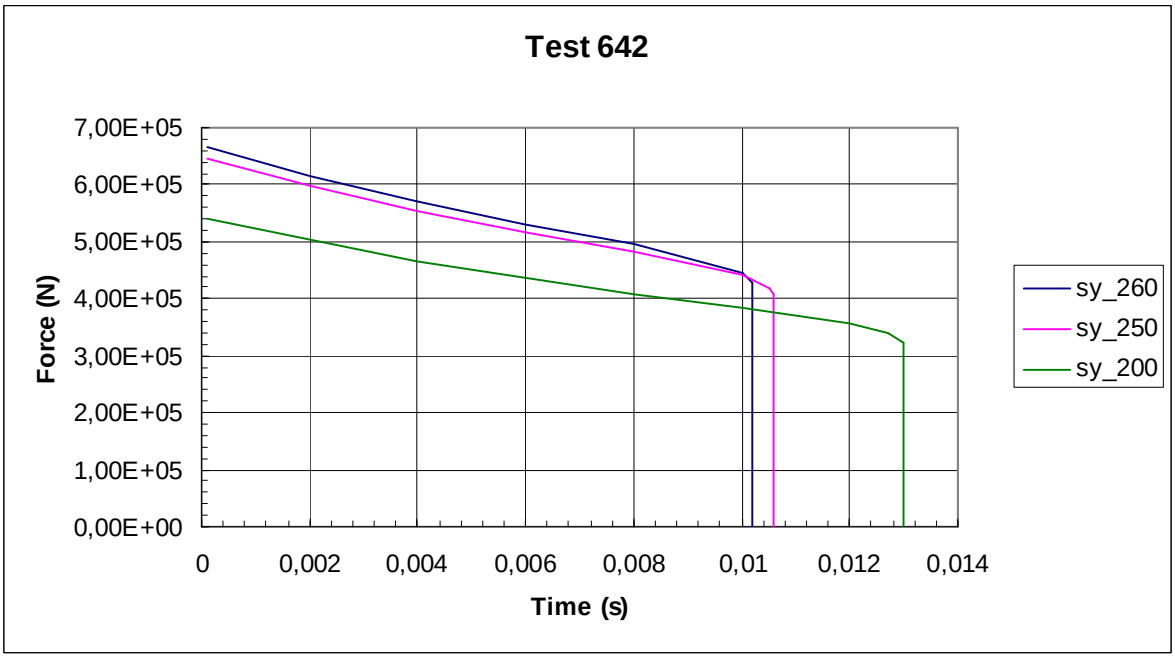

Figure 57. Force-time functions compared using varied yield strength values for Test 642.

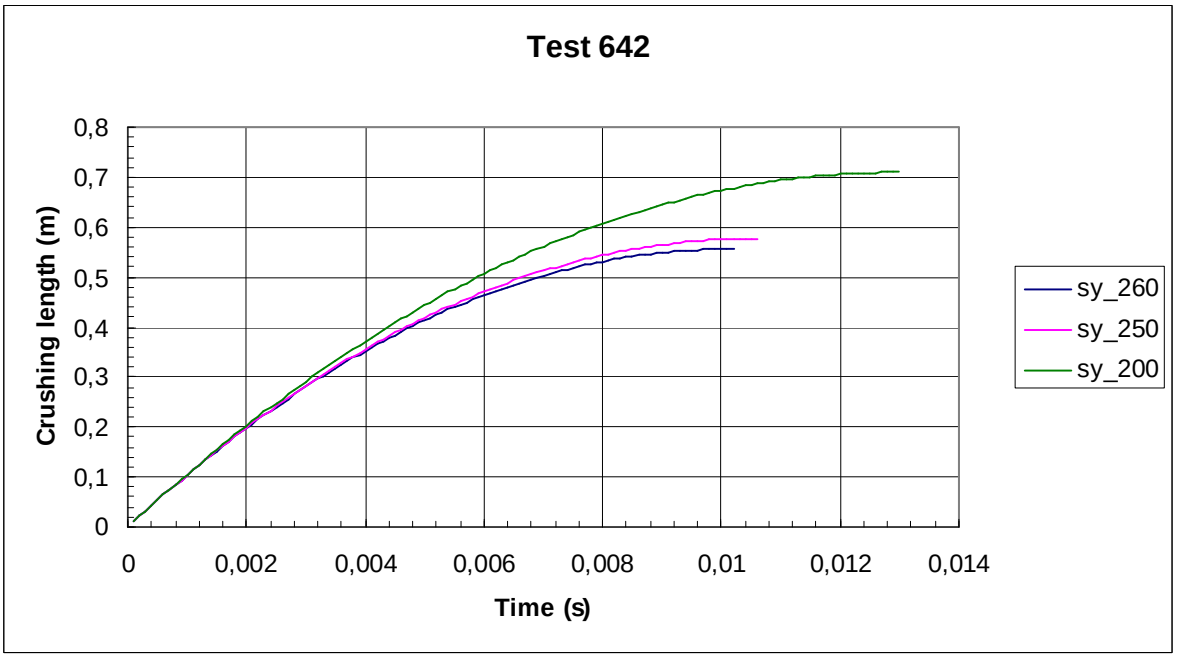

Figure 58. Crushed length of missile compared using varied yield strength values in Test 642.

Displacements as functions of time, calculated with the varied force-time functions, are shown in Figure 59, where also the measured result is shown. The calculated deflection decreases considerably when the maximum force value decreases and the impact duration time correspondingly increases.

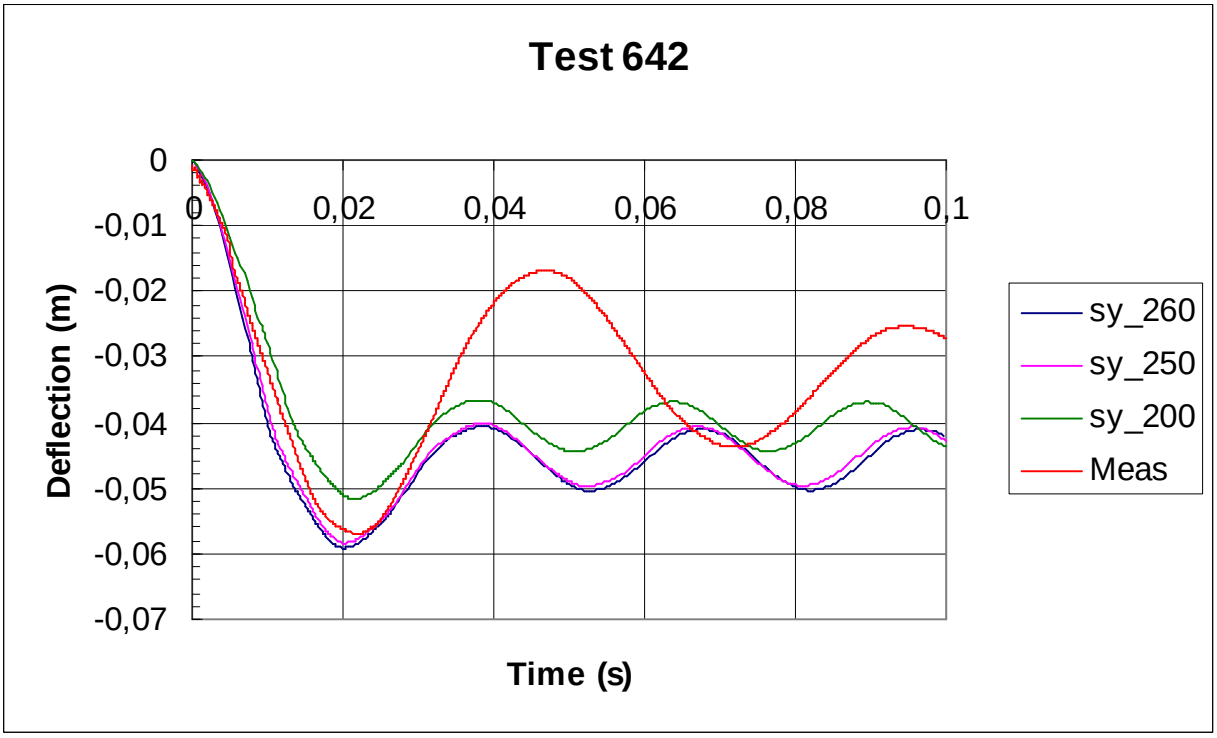

Figure 59. Deflections calculated using varied force-time function.

4.5.2 LS-DYNA results of Test 642

Many analyses were conducted with LS-DYNA code varying different parameters and four of them are considered here. In three cases of them, also the missile impacting onto the wall was modelled. In the fourth case, a pressure load according to the Riera method was applied onto the wall surface.

There are several ways in LS-DYNA to describe the fracture of a material. In the current study, the constrained tie-break method was used (LS-DYNA, 2007). In this method, the element edges are separated in order to describe crack propagation. The fracture of the aluminium tube was described by defining predetermined lines for the crack: the tube was sliced into longitudinal slices that were tied together with a failure criterion. When the criterion was set to 30% plastic strain, the cracks did not open and the main deformation mode was folding. In this case, the remaining length of the missile after the impact was approximately 915 mm. The original length is 1504mm. When the criterion was set to 25%, the cracks did open and the main deformation or failure mode was tearing. In this case, the remaining length of the missile after the impact was approximately 800 mm.

In the most recent case, some adjustments were made (such as smaller time steps) and the plastic strain value in failure was again set to 30%. This time there were clearly two successive modes and the missile deformed less than in the previous cases. The missile first tore into couple of strips after which it still folded slightly. The length of the missile was 984 mm after the impact. This type of behaviour was present also in the test. Figure 60 shows the missile and the wall at the ending phase of the impact in the most recent case. Figure 61 shows a detail of the missile model (left) and the picture of the real deformed missile (right). However, in the test, the remaining length after the impact was approximately only 800 mm, which corresponds best with the mere tearing mode case.

Figure 62 shows the impact forces in Test 642 calculated with the Riera method and LS-DYNA with different parameter values. As can be seen, the simulated contact forces correspond reasonably well with the Riera curve. The impacts last slightly longer, but correspondingly the force stays slightly lower (excluding the first peak). Especially with the tearing mode the impact lasts relatively long, while the force time curve is smoother than with the folding mode. The most recent analysis case discussed above is depicted as “New” in Figure 62.

(Dilger et al., 1984), (Lin, 1998), (Malvar et al., 1997), (Yonten et al., 2002).

Figure 60. The missile and the wall after the impact.

Figure 61. The deformed missile model and the actual deformed missile after the impact.

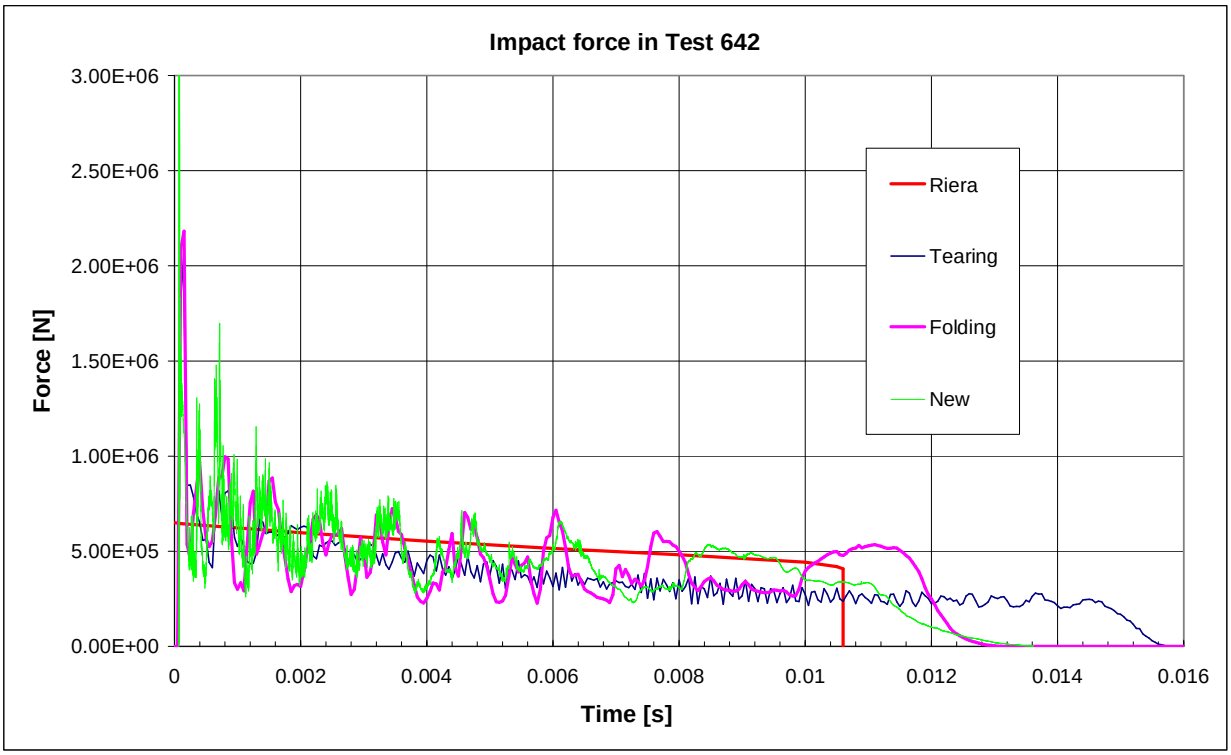

Figure 62. Impact forces in Test 642 calculated with the Riera method and LS-DYNA with different parameter values.

4.6 Test 644

4.6.1 Shell element analyses of Test 644

Test 644 was carried out with a water filled missile. The loading function transient is shown in Figure 36. Nonlinear material properties used in this calculation are presented in Chapter 4.1. Energy balance during the calculation is shown in Figure 63. The locations for displacement sensors are presented in Figure 37. The calculated and measured displacements are presented in Figure 64 and they are in a quite good agreement. The displacement recorded at the location D1 was slightly underestimated by the FE calculation. This may be due to the fact that the used shell element is not capable to calculate nonlinear transverse shear behaviour. The displacement at D1 is partly due to bending and partly due to transverse shear deformation.

The measured and calculated strains in reinforcement are presented in Figure 65 as a function of time. Figure 66 shows the calculated strains in reinforcement. The accumulated plastic strain distribution contour in the horizontal back surface reinforcement is presented in Figure 67. The maximum strain value is about 5% in a relatively small area in the middle part of the slab.

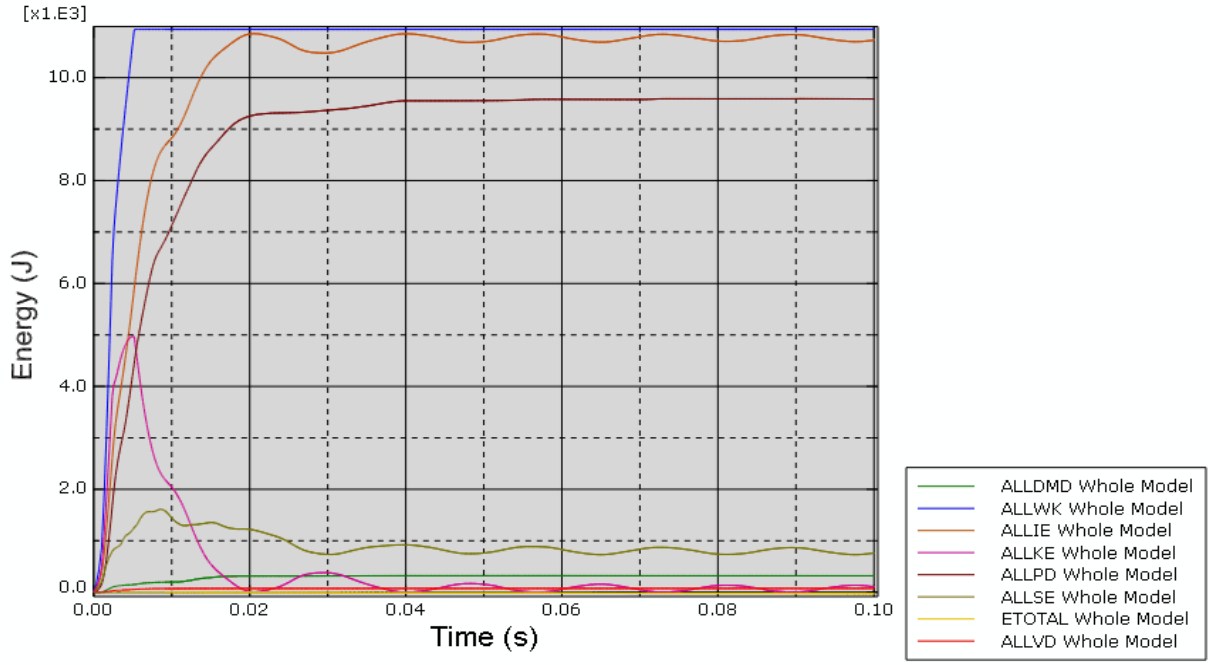

Figure 63. Energy balance during the calculation in Test 644.

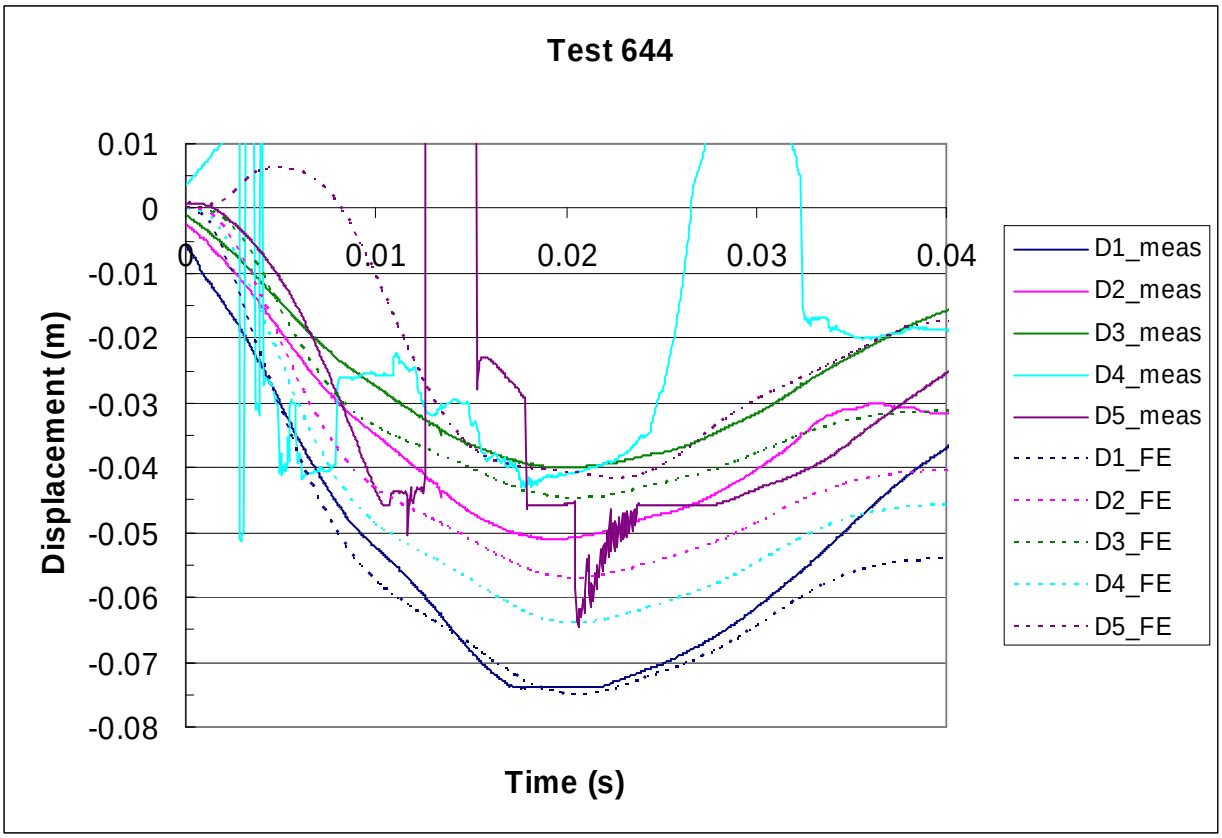

Figure 64. Measured and calculated displacements as a function of time in Test 644.

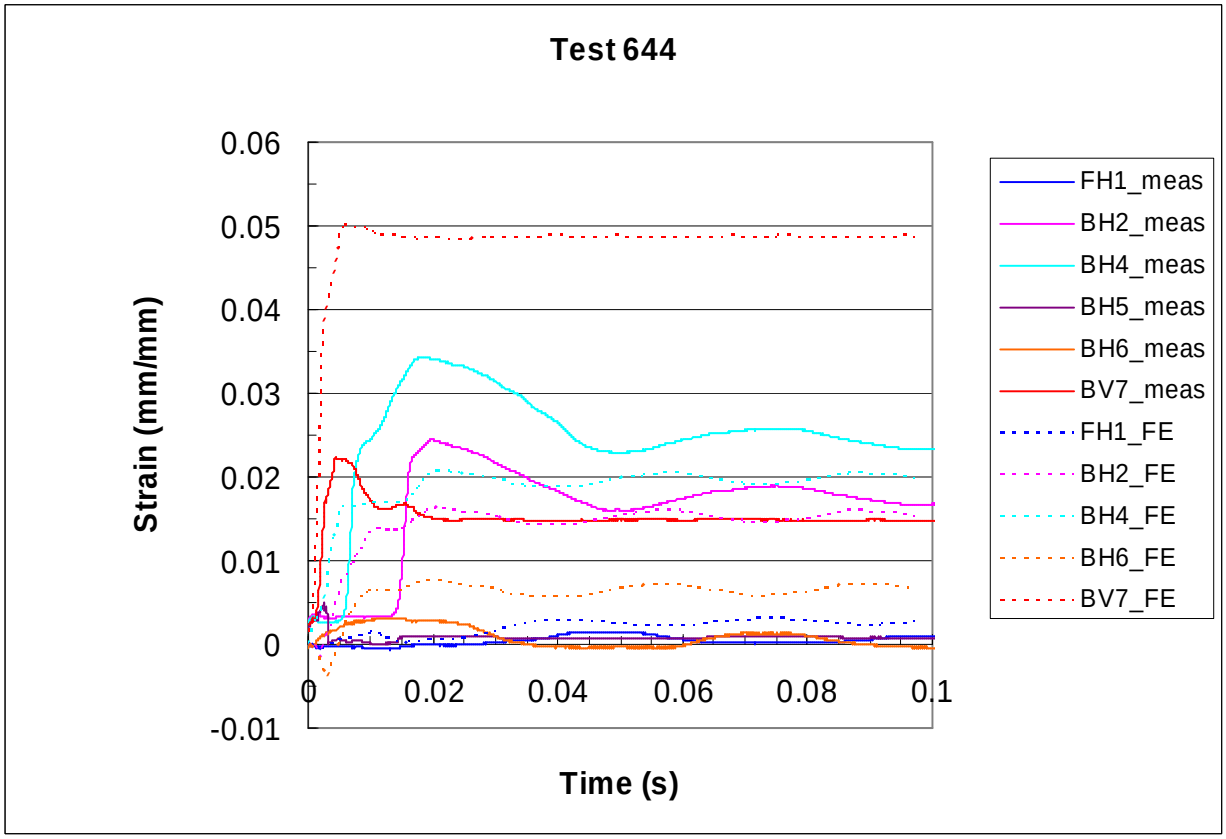

Figure 65. Measured and calculated strains in the reinforcement in Test 644.

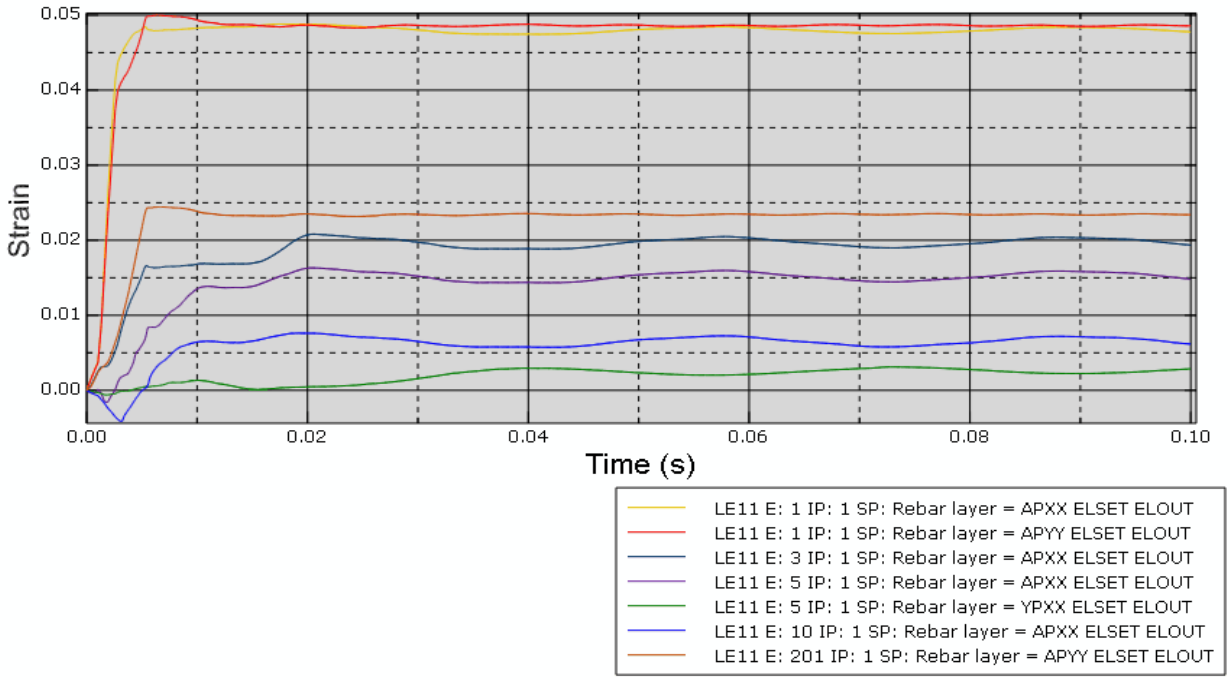

Figure 66. Calculated strains in reinforcement in Test 644.

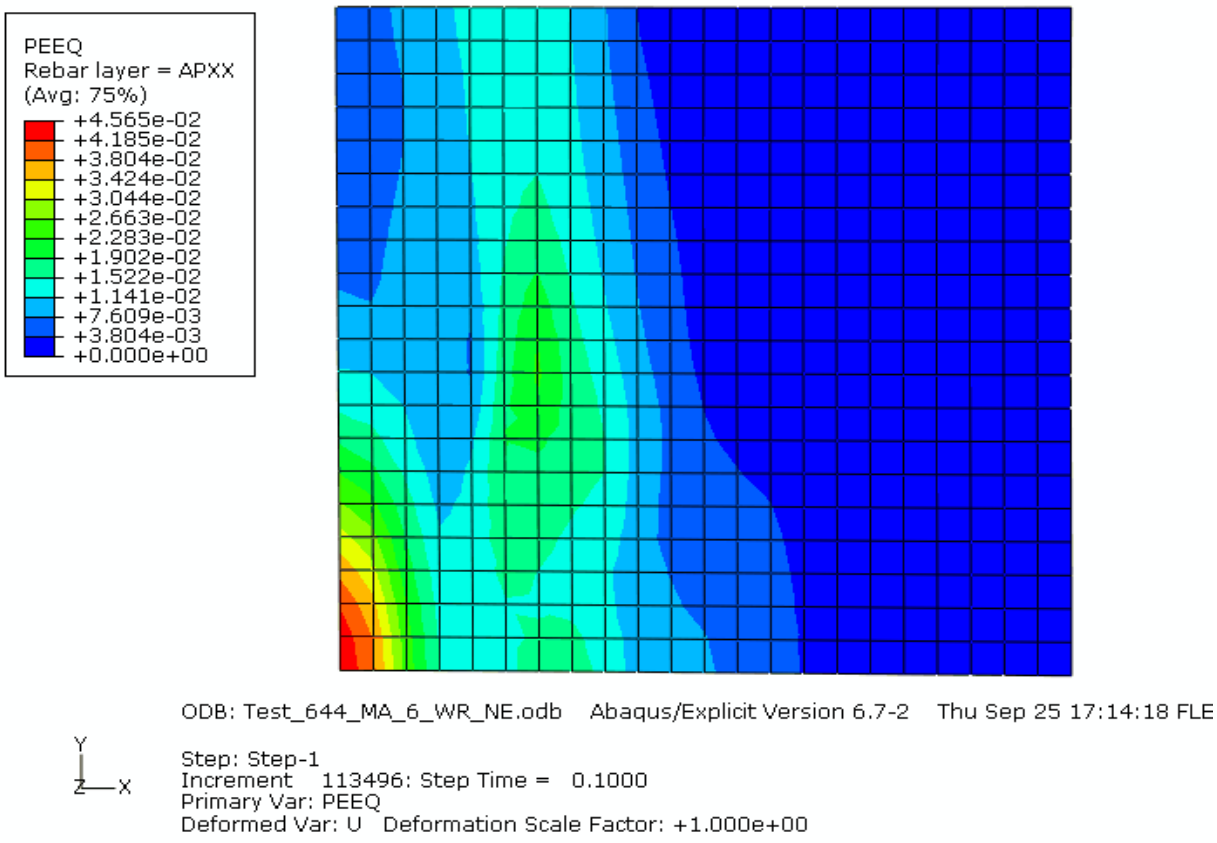

Figure 67. The plastic strain distribution in horizontal reinforcement at the back surface in Test 644.

The front surface of the wall 644 after the test is shown in Figure 68 and a part of the back surface is shown in Figure 69. As can bee seen, the tensile cracking is somewhat localized in the central part of the wall. A quarter section of the test wall 644 cut at the centre line is shown in Figure 70.

Figure 68. Wall front after Test 644.

Figure 69. The backside of the wall after Test 644.

Figure 70. Quarter section of the test wall 644 cut at the centre line.

Test 663

4.6.2 Shell element analyses of Test 663

The aluminium material of the missile used in Test 663 was not exactly the same as in the previous tests, and this material is referred to as Al3. Material properties affect the loading function by decreasing the P_c force used in the Riera formula. The loading function used in the following calculation is presented in Figure 36 (almost the same as for Test 673). Energy balance was maintained during the FE analysis, shown in Figure 71. The locations for displacement sensors in Test 663 are shown in Figure 72. The calculated and measured displacements are presented in Figure 73. The measured and calculated strain values in the reinforcement are presented in Figure 74 and in Figure 75.

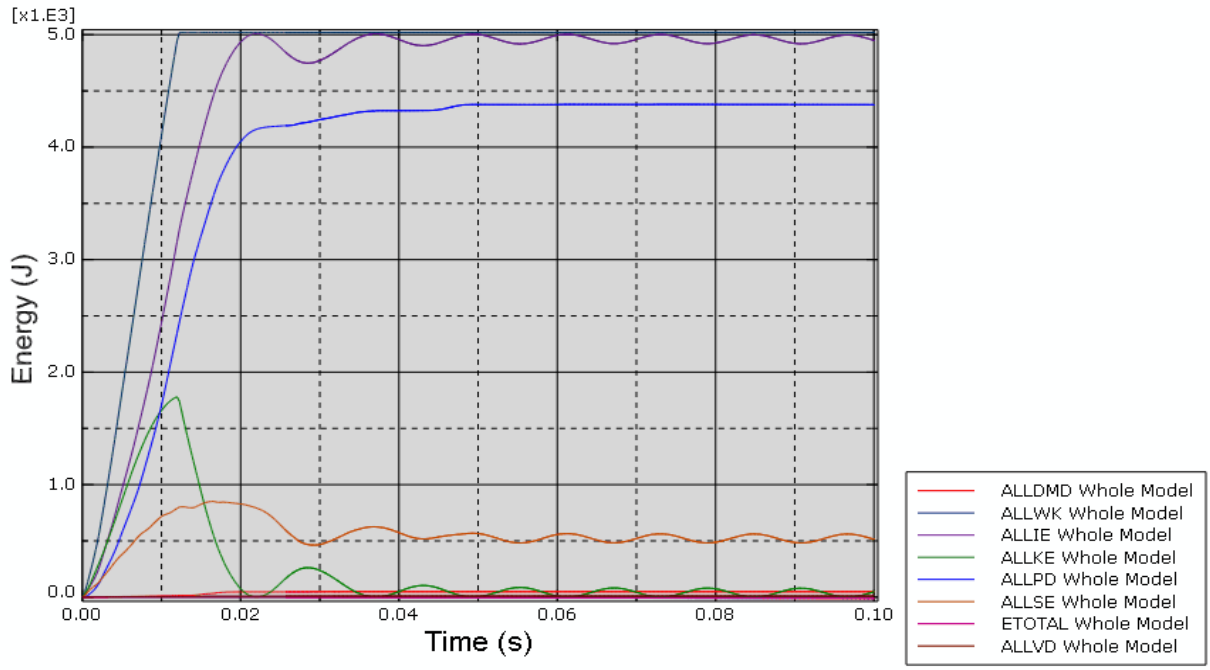

Figure 71. Energy balance during the calculation of Test 663.

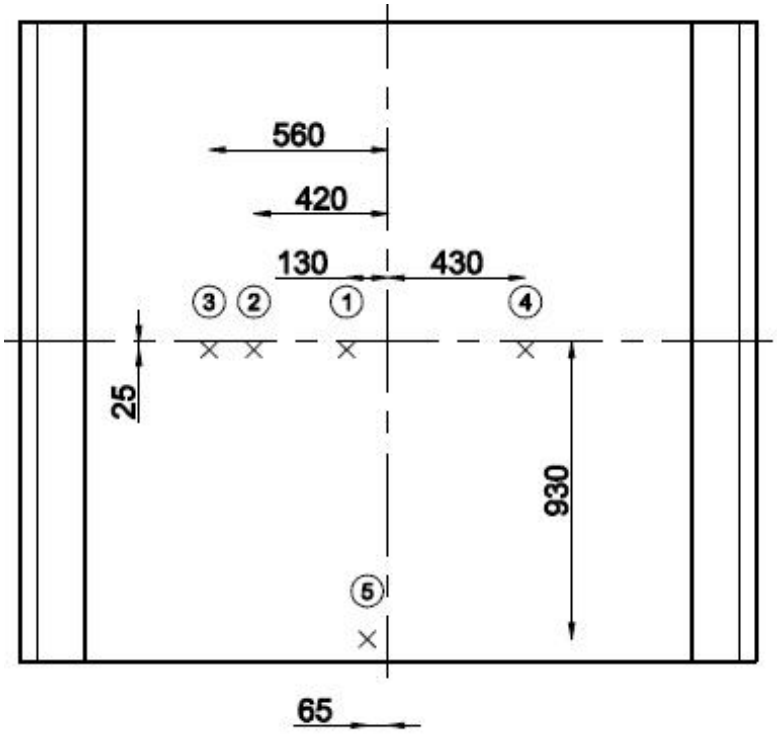

Figure 72. Locations of displacement sensors in Test 663.

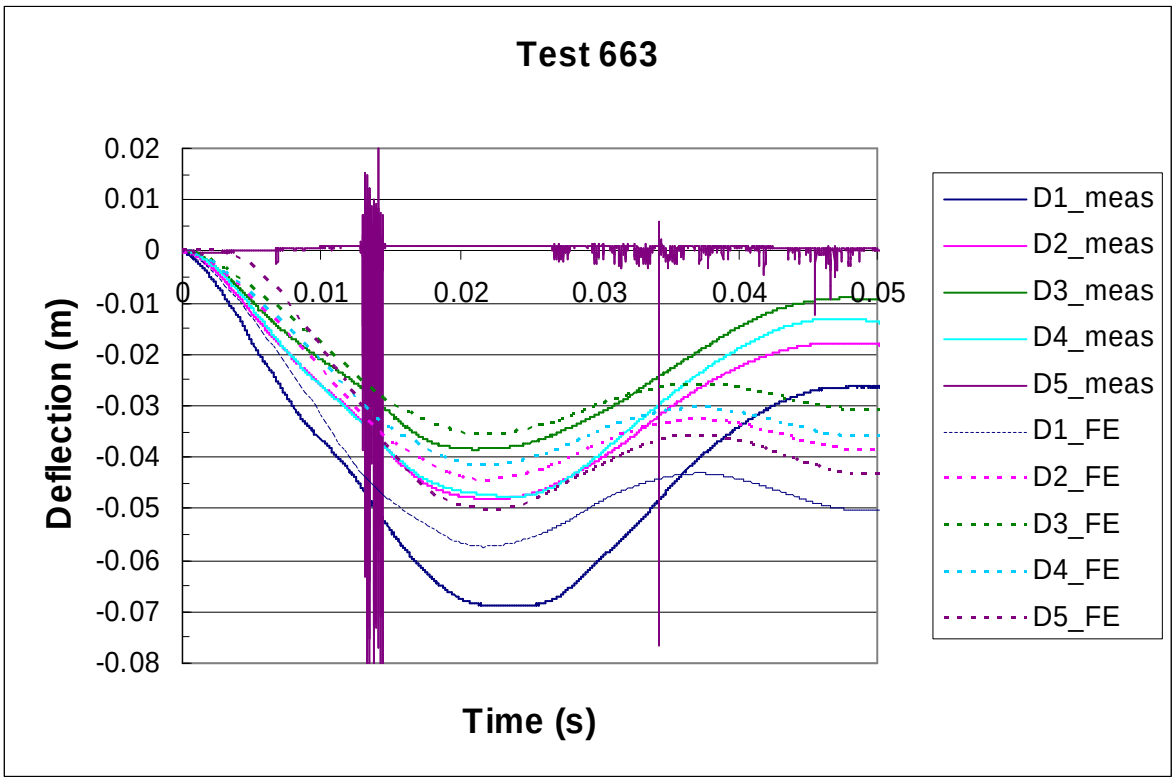

Figure 73. Measured and calculated displacements as functions of time in Test 663.

The calculated displacements at locations D2-D4 correspond rather well to the measured values. However, at the central area of the wall, the calculated deflection values are underestimated. This is due to the beginning of a shear cone formation, which is not taken into consideration with the shell element used in calculation.

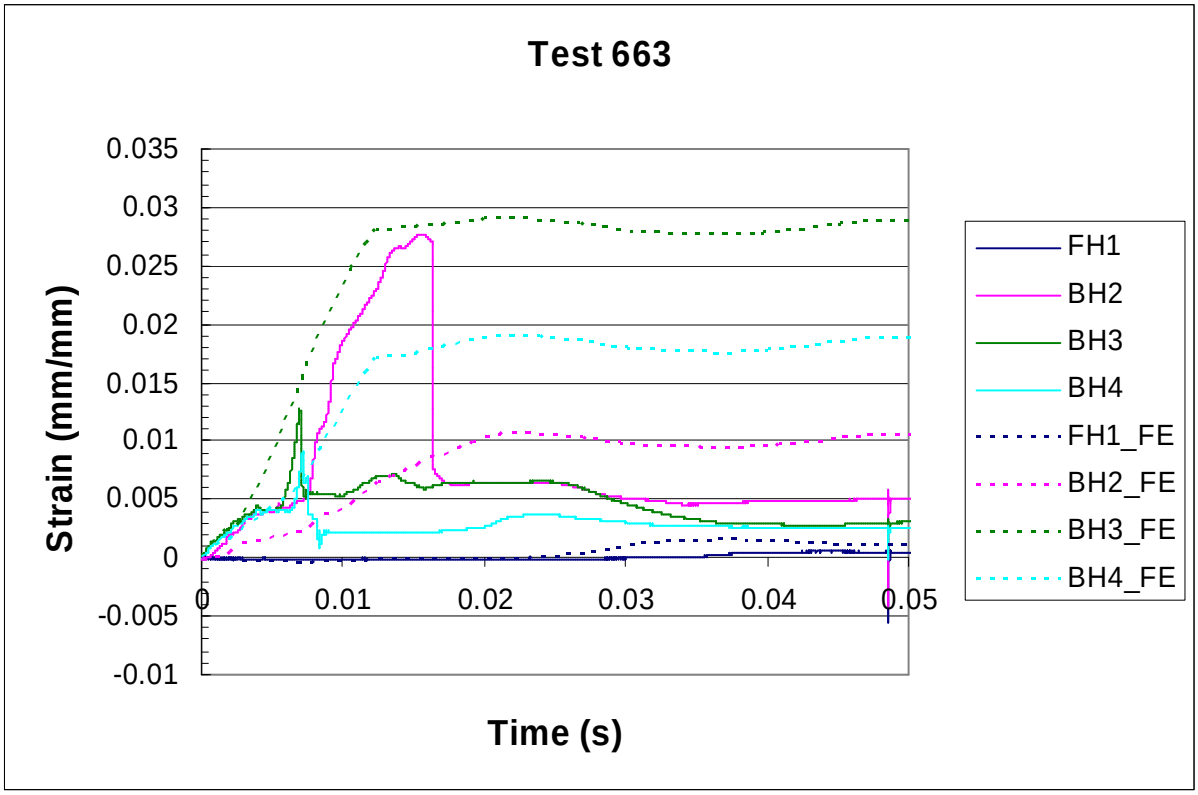

Figure 74. Measured and calculated strains in the reinforcement at BH2-5 in Test 663.

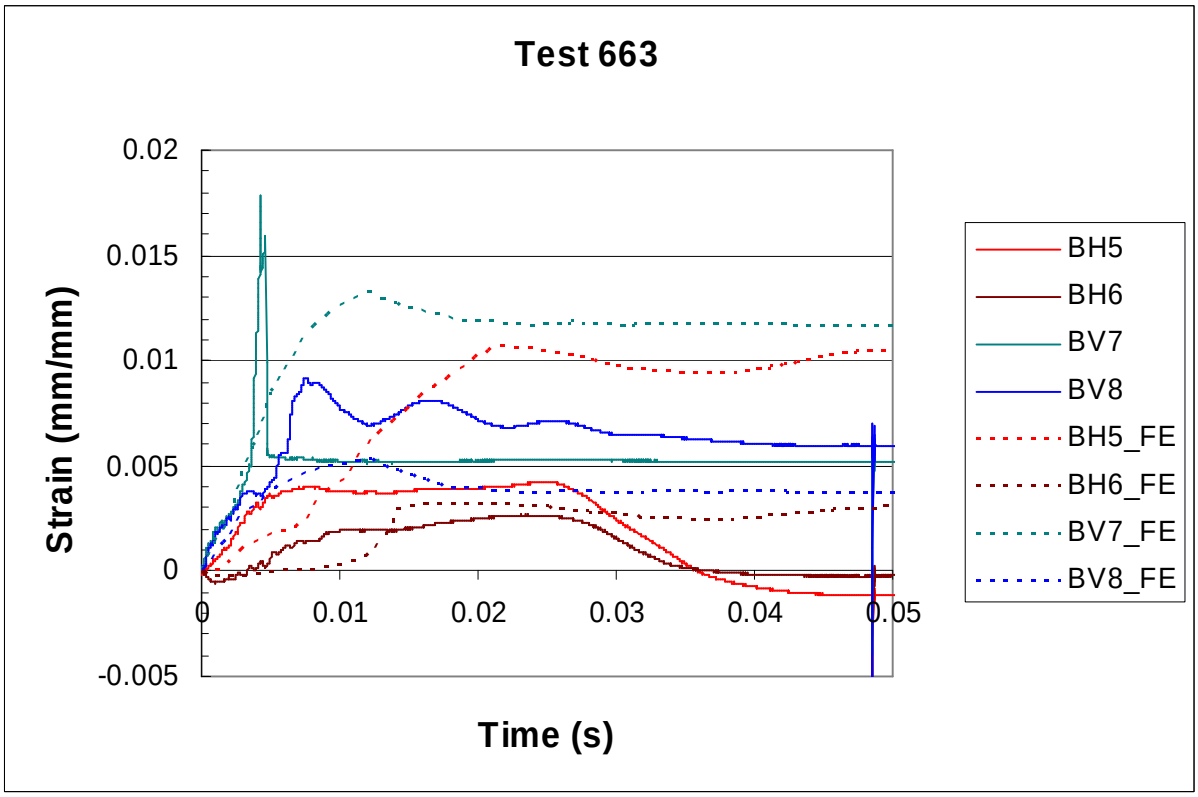

Figure 75. Measured and calculated strains in the reinforcement at FH1, BH6 and BV8 in Test 663.

The front face of the wall of Test 663 is shown in Figure 76 and the cracked back surface is shown in Figure 77. As can be seen, the cracking is localised in the middle of the wall. A quarter section of the test wall 663 cut at the centre line is shown in Figure 78.

Figure 76. Front surface of the wall after test in Test 663.

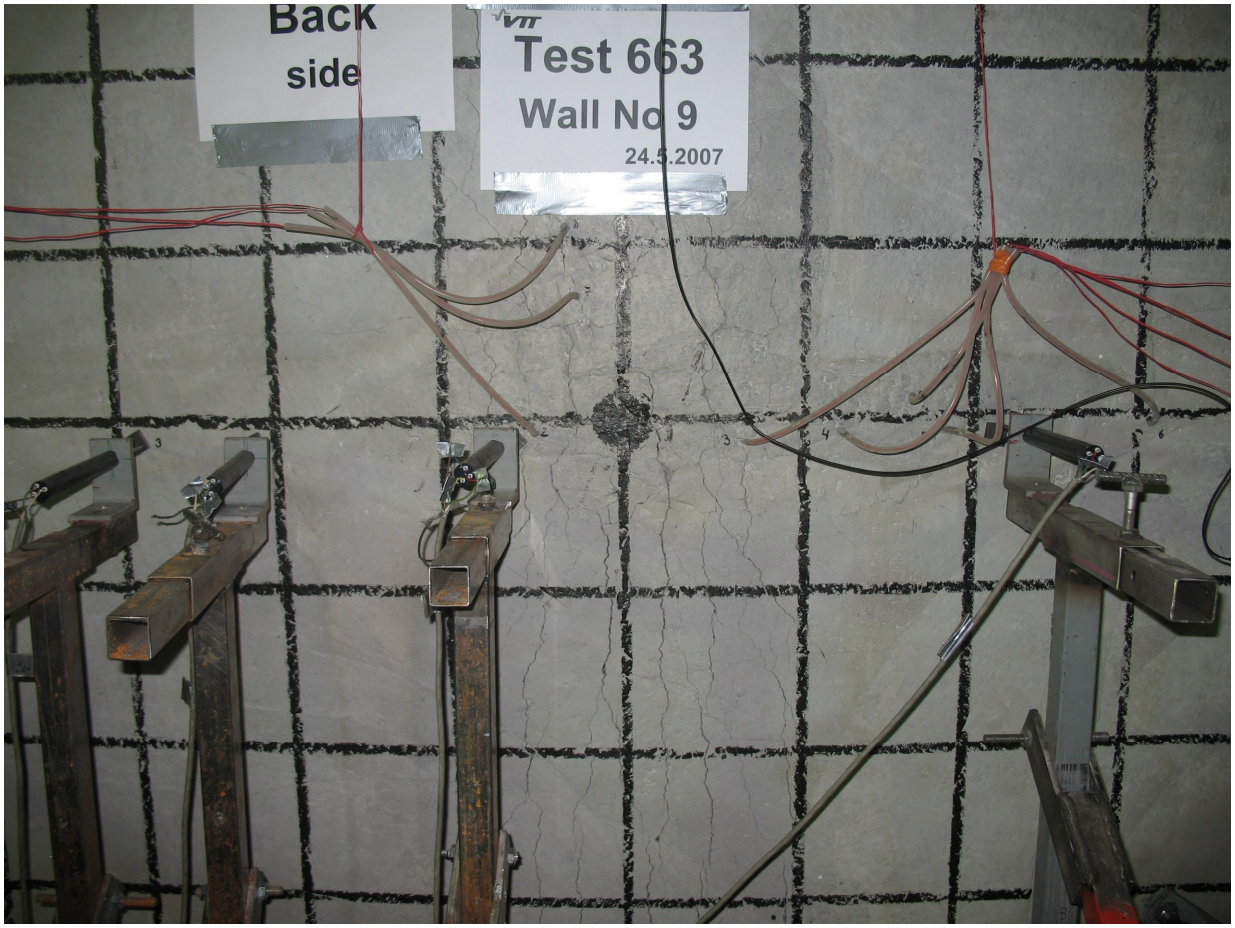

Figure 77. Back surface of the wall after test in Test 663.

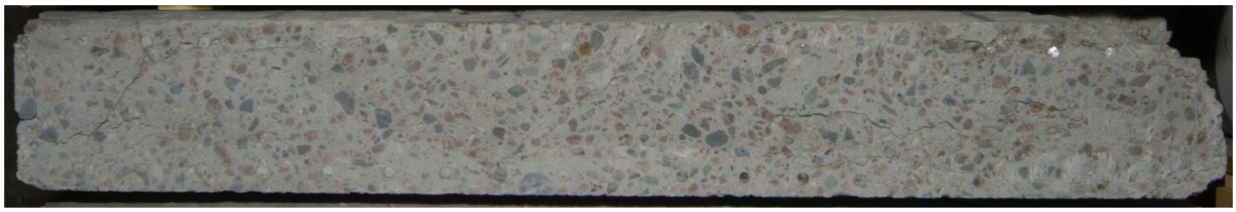

Figure 78. Quarter section of the test wall 663 cut at the centre line.

Sensitivity study with varied tensile cracking stress-strain parameters

For the sake of comparison, the post calculation was carried out with alternative tensile stress-strain behaviour of material 2, presented in Figure 40. The calculated displacements are presented with the corresponding measured values in Figure 79. The calculated displacement values at locations denoted by D2 to D4 are now somewhat higher than the corresponding measured values. The measured deflection closest to the centre of the wall is still greater than the corresponding calculated deflection. As mentioned already before, this is believed to be due to the formation of the shear cone. A shear cone was visually observed in situ but it cannot be clearly seen in Figure 78.

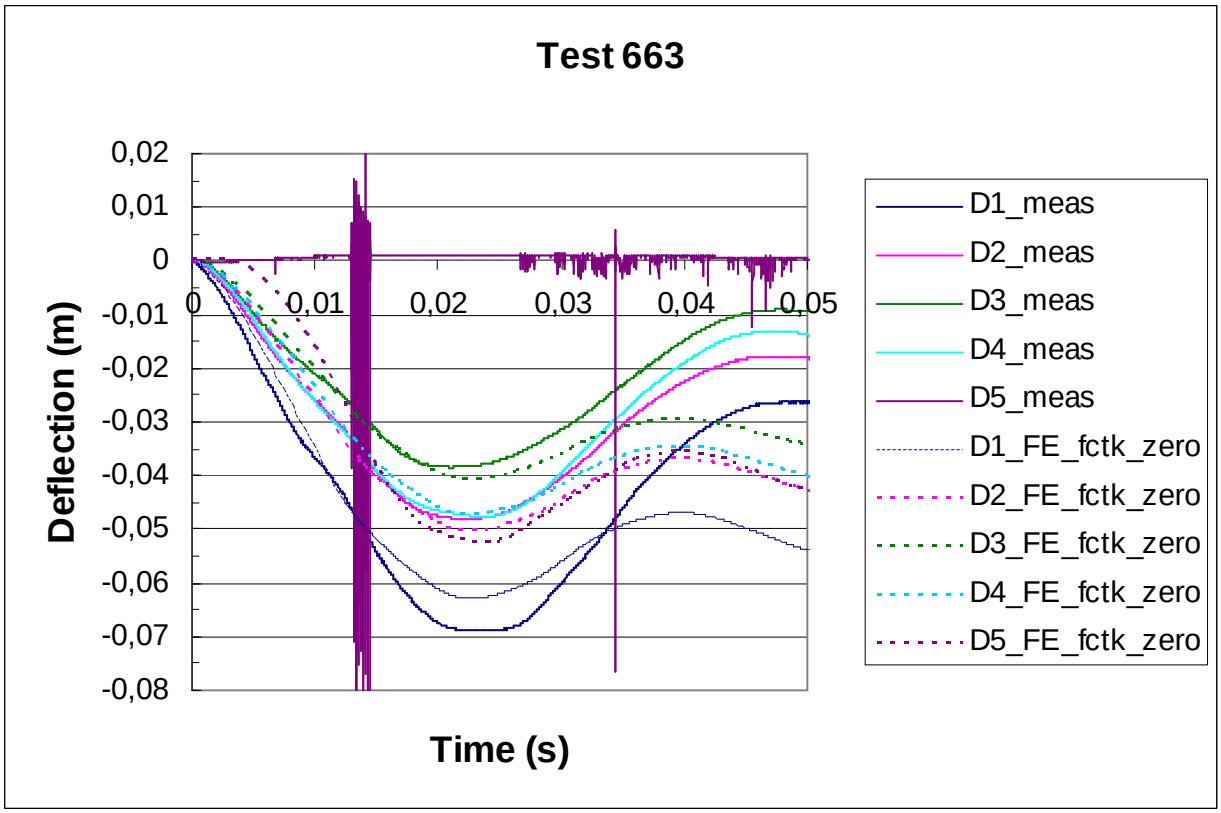

Figure 79. Calculated and measured displacements in Test 663.

4.7 Test 673

4.7.1 Shell element analyses of Test 673

The main difference between Test 663 and Test 673 is that in the wall of Test 673 there was shear reinforcement of 0.00503 mm^2/m^2. In this analysis, the shear reinforcement is not taken into consideration. The loading function predicted for Test 673 is presented in Figure 36. The material of the missile in Test 673 was Al3.

Energy balance was maintained during the analysis as shown in Figure 80. The locations for displacement sensors are presented in Figure 81. The calculated displacements are presented in Figure 82 with the corresponding measured values. The calculated displacements are somewhat lower than the corresponding measured values. The calculated strains in the horizontal back surface reinforcement are shown in Figure 83 together with the measured values. The calculated strain values are somewhat lower than the measured strain values. The calculated strain distribution in the horizontal back surface reinforcement is presented in Figure 87. The corresponding strain distributions in vertical back surface reinforcement, horizontal front surface reinforcement and vertical front surface reinforcement are presented in Figure 88, in Figure 89 and in Figure 90, respectively. As can bee seen in these figures, there are rather steep gradients in the strain distribution.

The front surface and back surface of the wall after the impact are shown in Figure 91 and Figure 92, respectively. A quarter section of the test wall 673 cut at the centre line is shown in Figure 93.

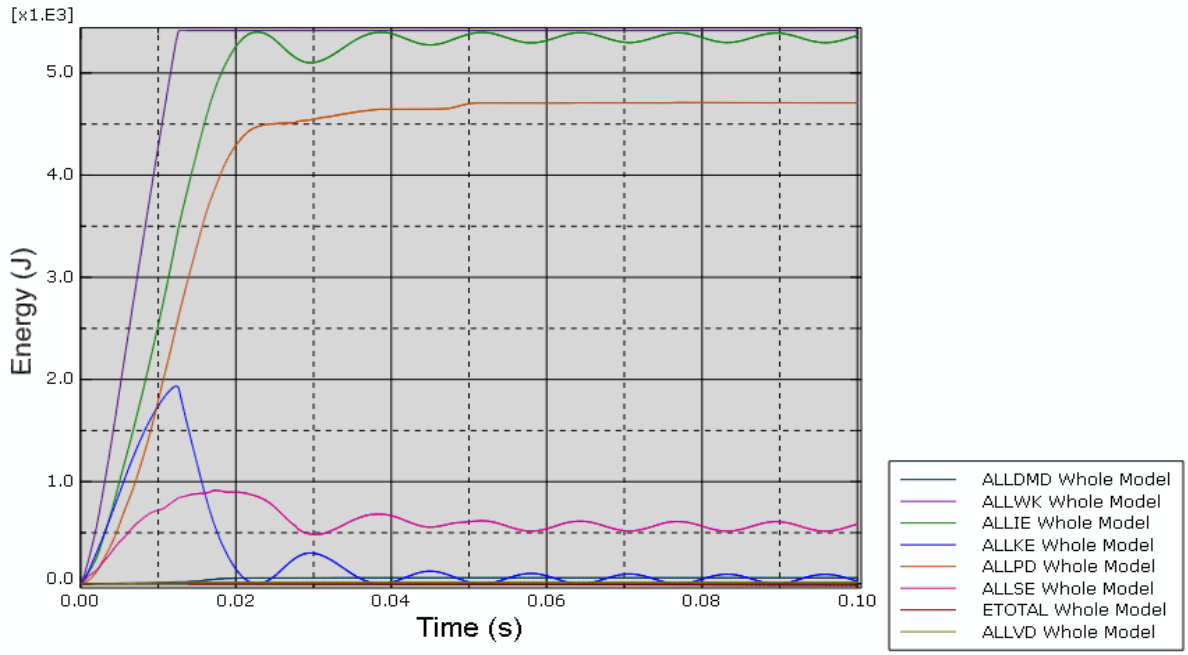

Figure 80. Energy balance during the calculation in Test 673.

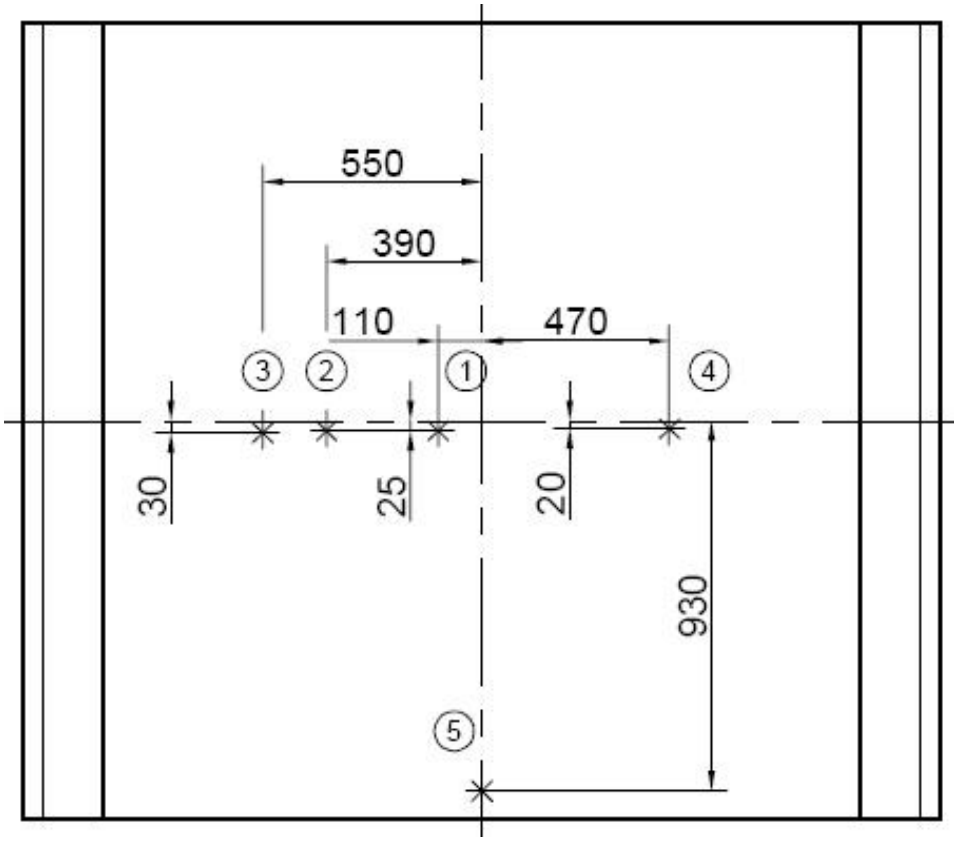

Figure 81. Displacement sensor locations in Test 673.

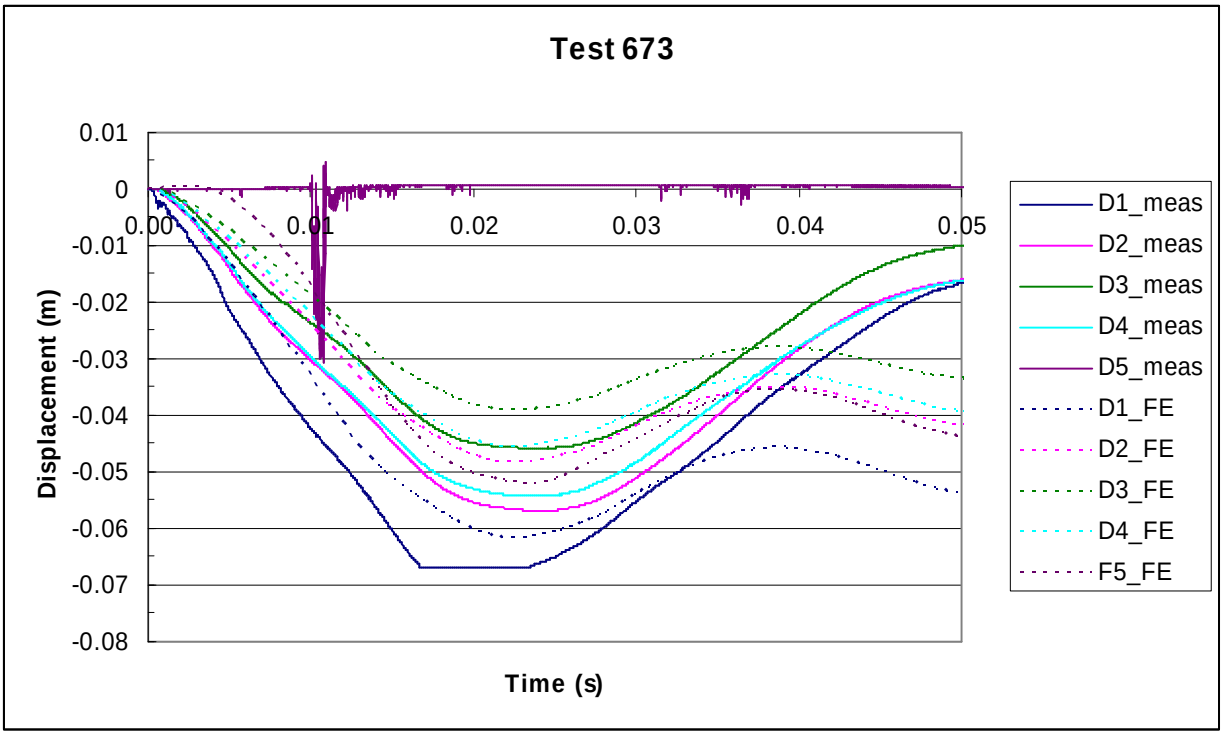

Figure 82. Measured and calculated displacements as functions of time in Test 673.

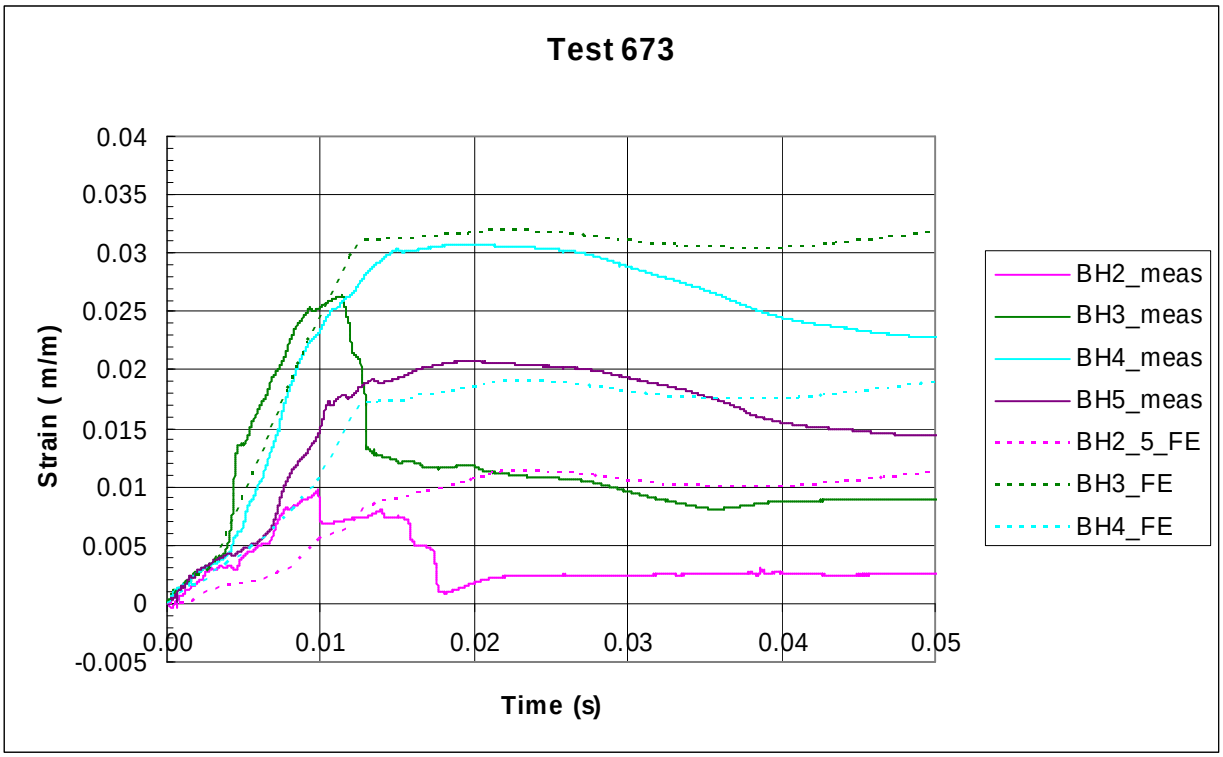

Figure 83. Measured and calculated strains in the reinforcement at locations BH2, BH3, BH4 and BH5 in Test 673.

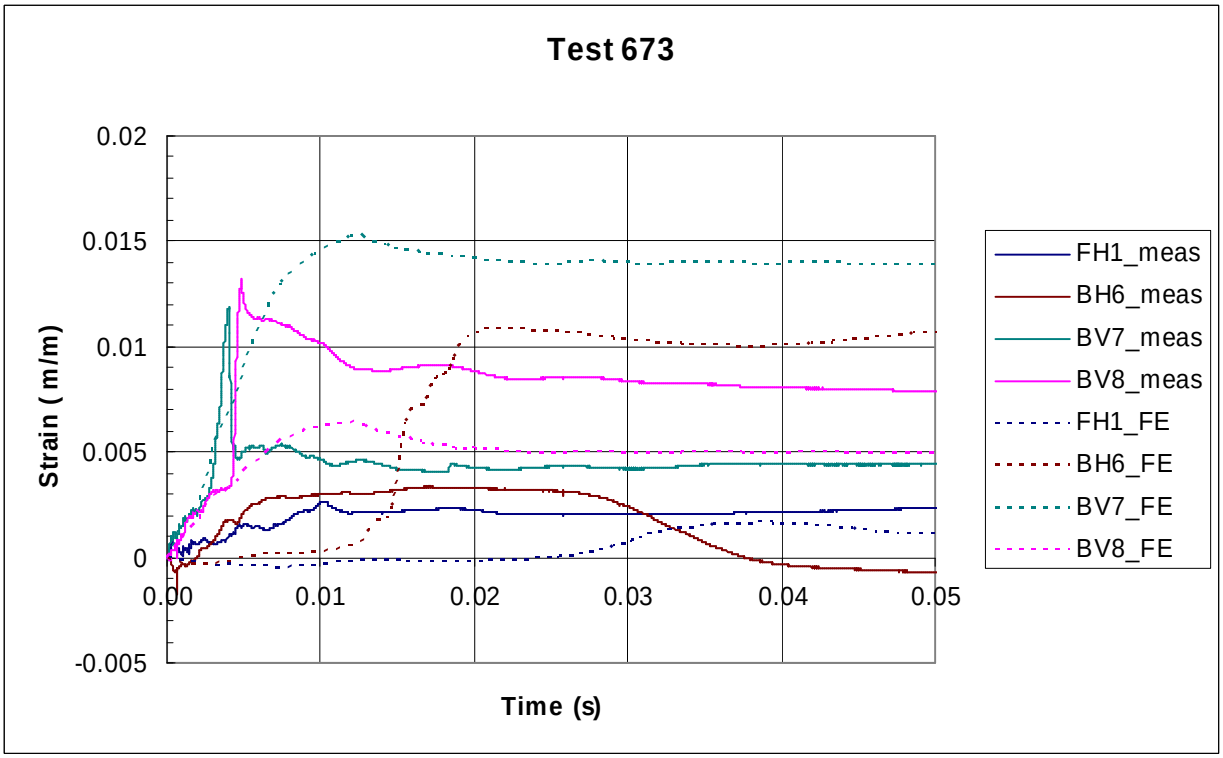

Figure 84. Measured and calculated strains in the reinforcement at FH1, BH6, BV7 and BV8 in Test 673.

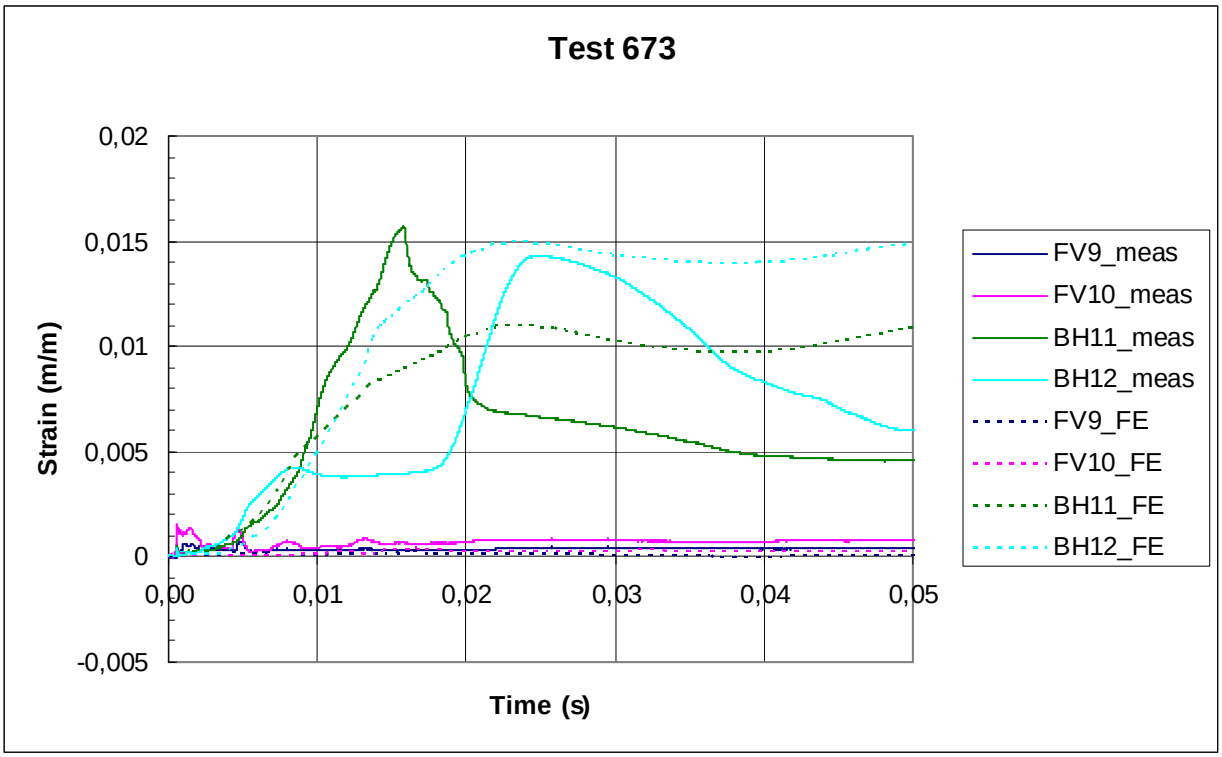

Figure 85. Measured and calculated strains in the reinforcement at FV9, FV10, BH11 and BH12 in Test 673.

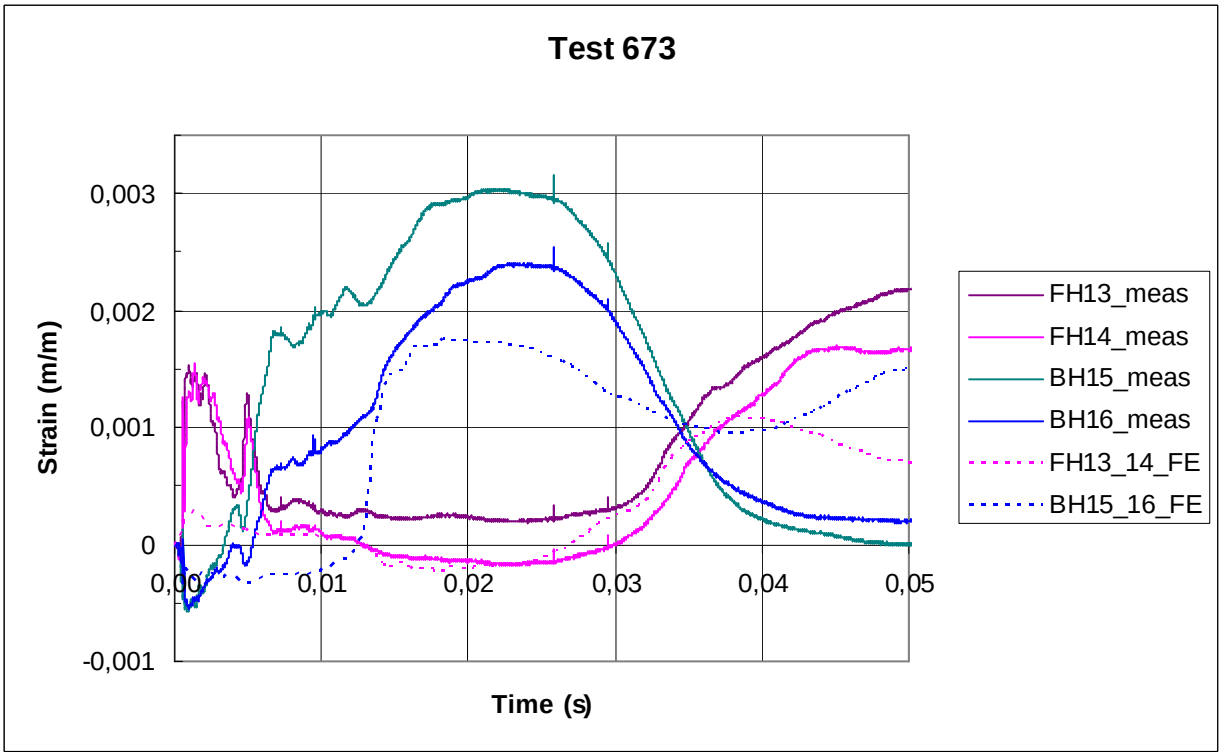

Figure 86. Measured and calculated strains in the reinforcement at locations FH13, FH14, BH15 and BH16 in Test 673.

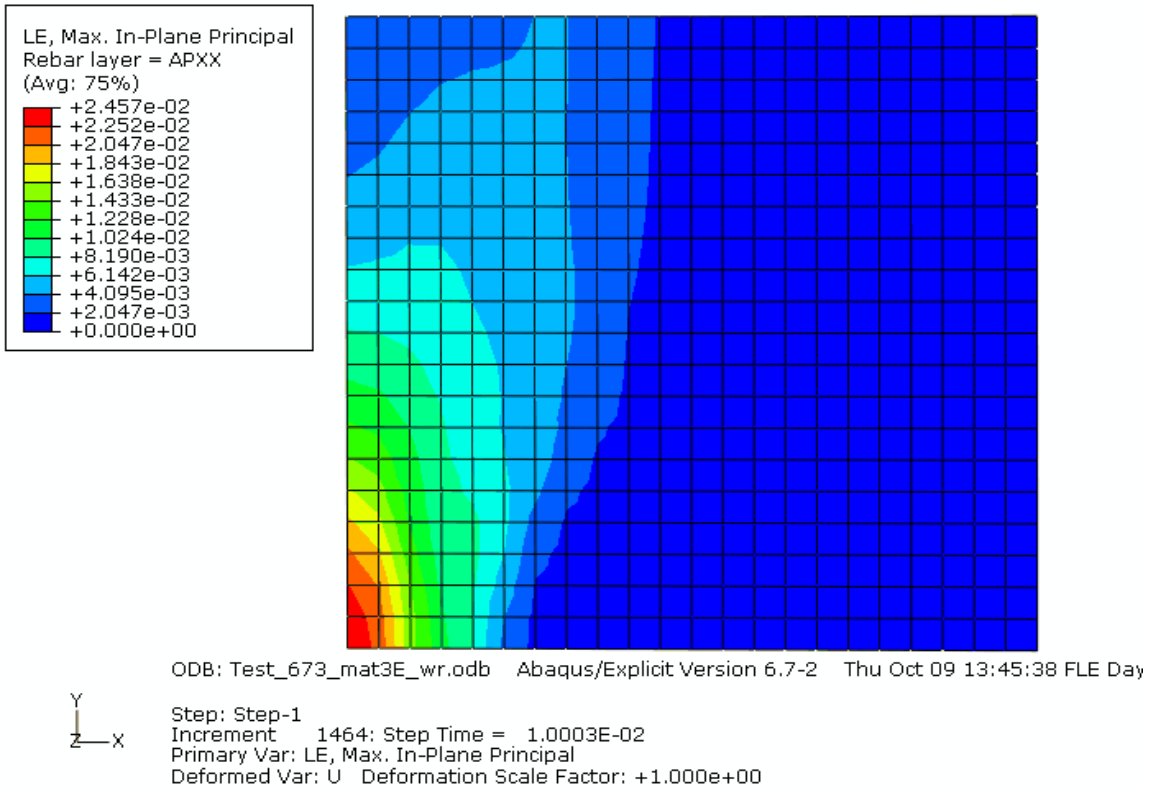

Figure 87. Strain distribution in horizontal back surface reinforcement at t= 0.01 s in Test 673.

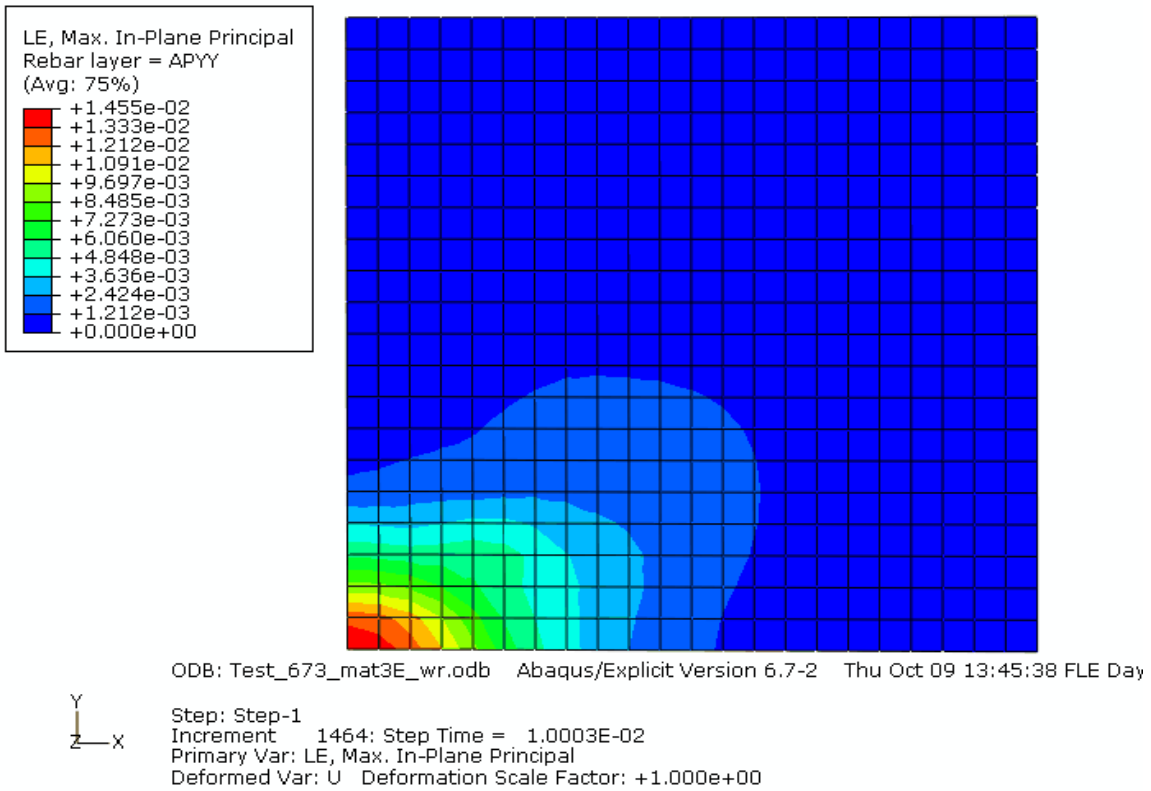

Figure 88. Strain distribution in vertical back surface reinforcement at t= 0.01 s in Test 673.

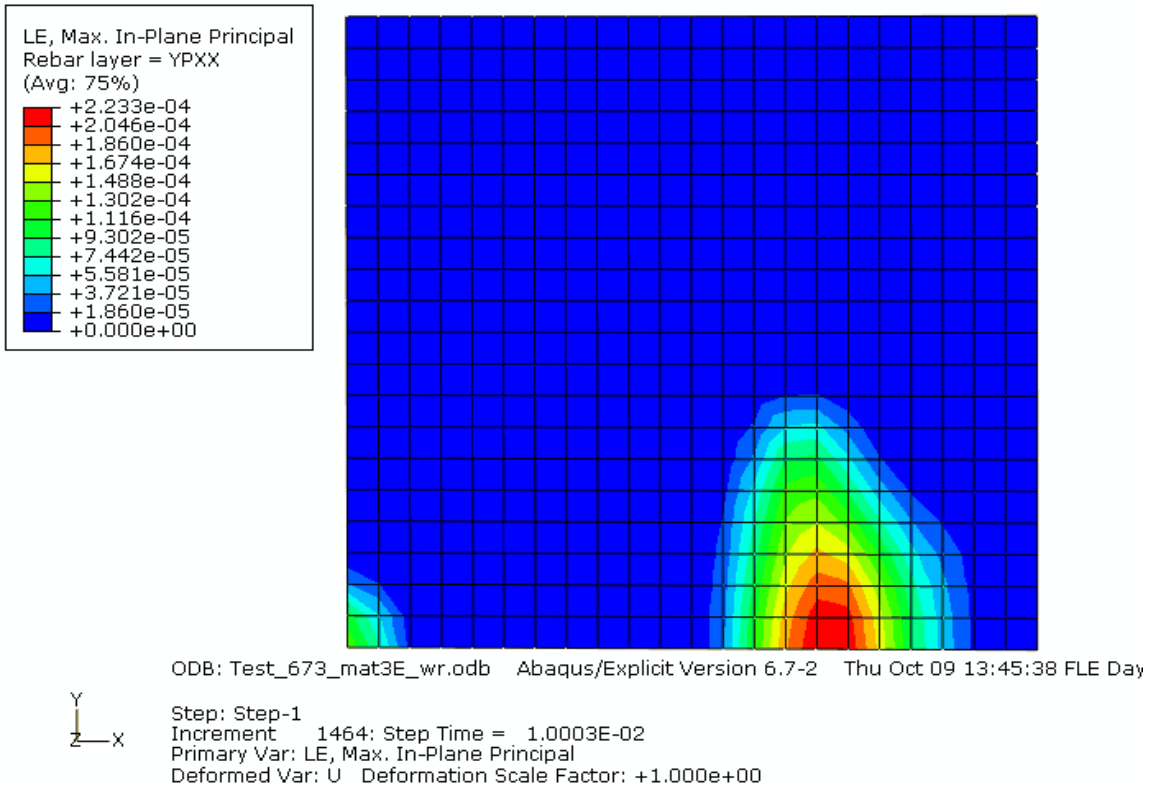

Figure 89. Strain distribution in horizontal front surface reinforcement at t= 0.01 s in Test 673.

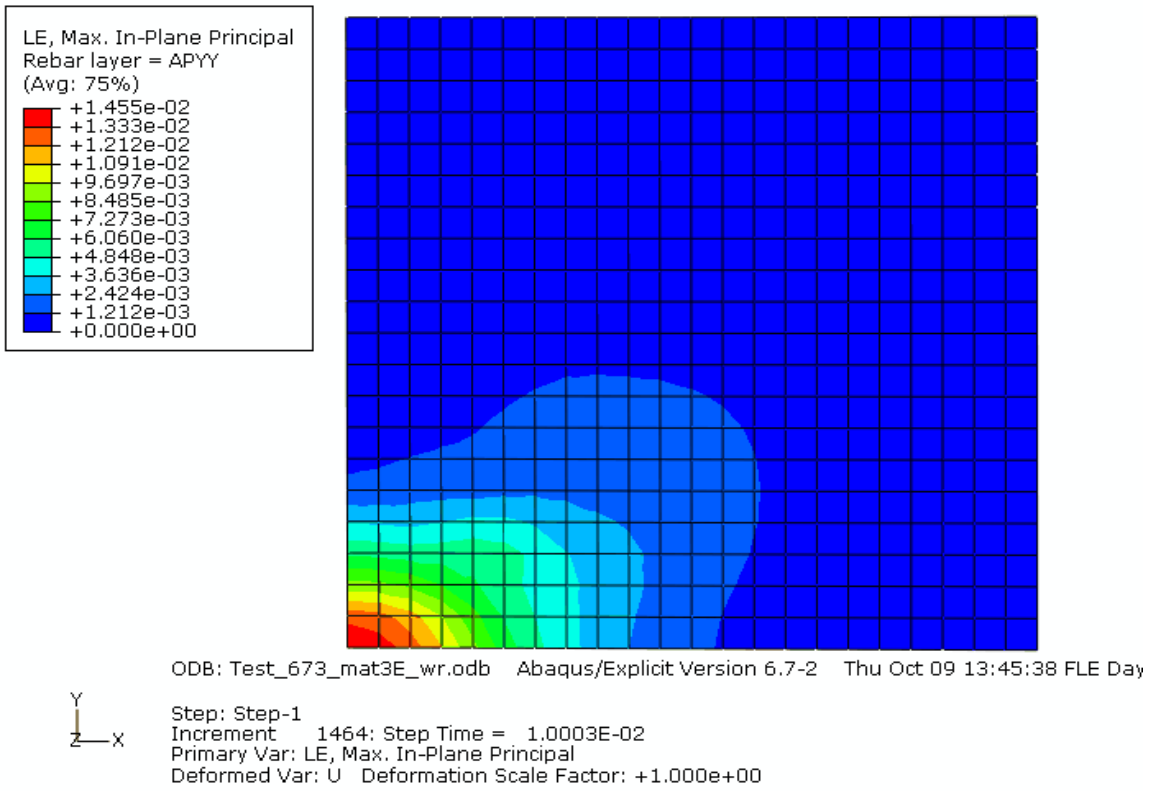

Figure 90. Strain distribution in vertical front surface reinforcement at t= 0.01 s in Test 673.

Figure 91. Front surface of the wall in Test 673.

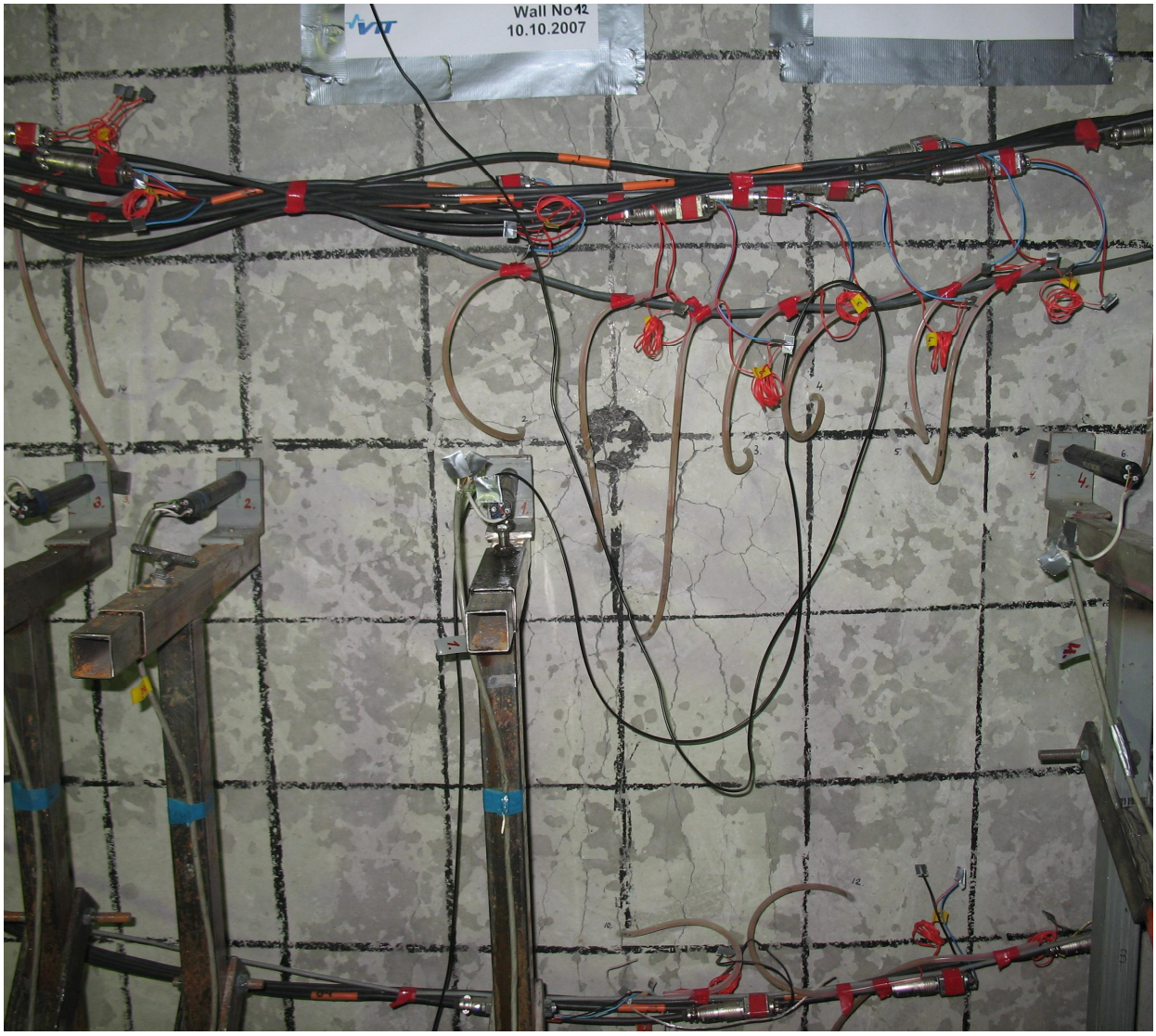

Figure 92. Back surface of the wall in Test 673.

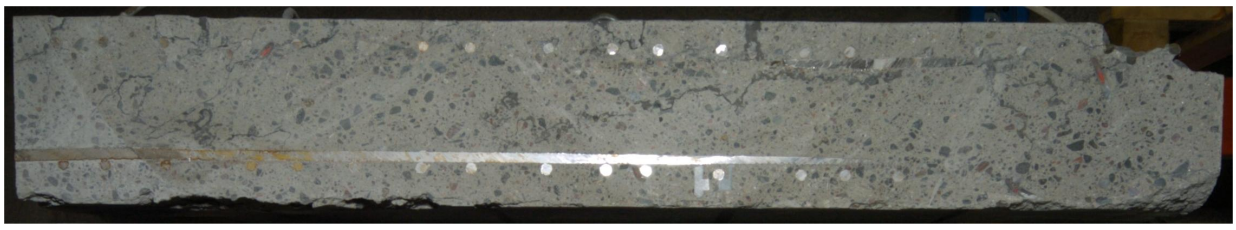

Figure 93. Quarter section of the test wall 673 cut at the centre line.

Sensitivity studies with varied tensile stress-strain parameters

A post calculation was carried out with modified material parameter values. The applied tensile stress-strain dependency of material 3 is presented in Figure 40. The calculated and measured displacement values are shown in Figure 94. In this case, there is less discrepancy between the calculated and measured results than in Test 663. In Test 673, due to the shear reinforcement, no clear shear cone formation was observed.

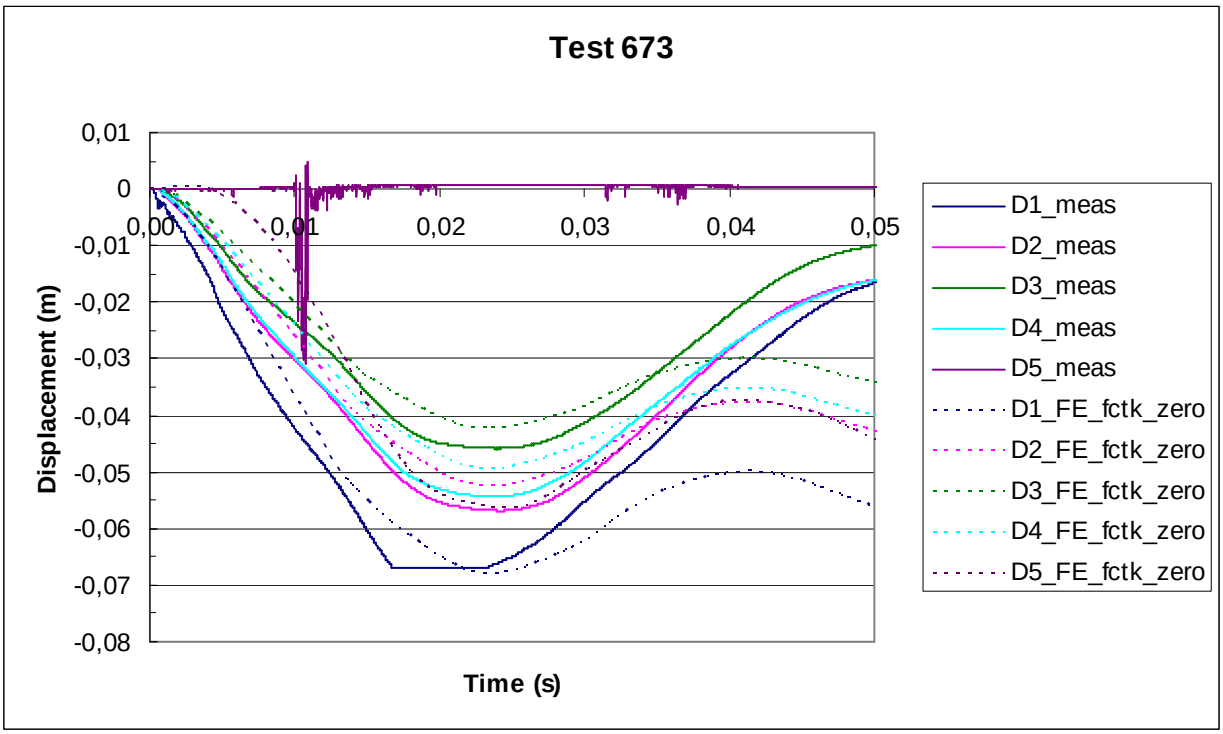

Figure 94. Measured and calculated displacements in Test 673.

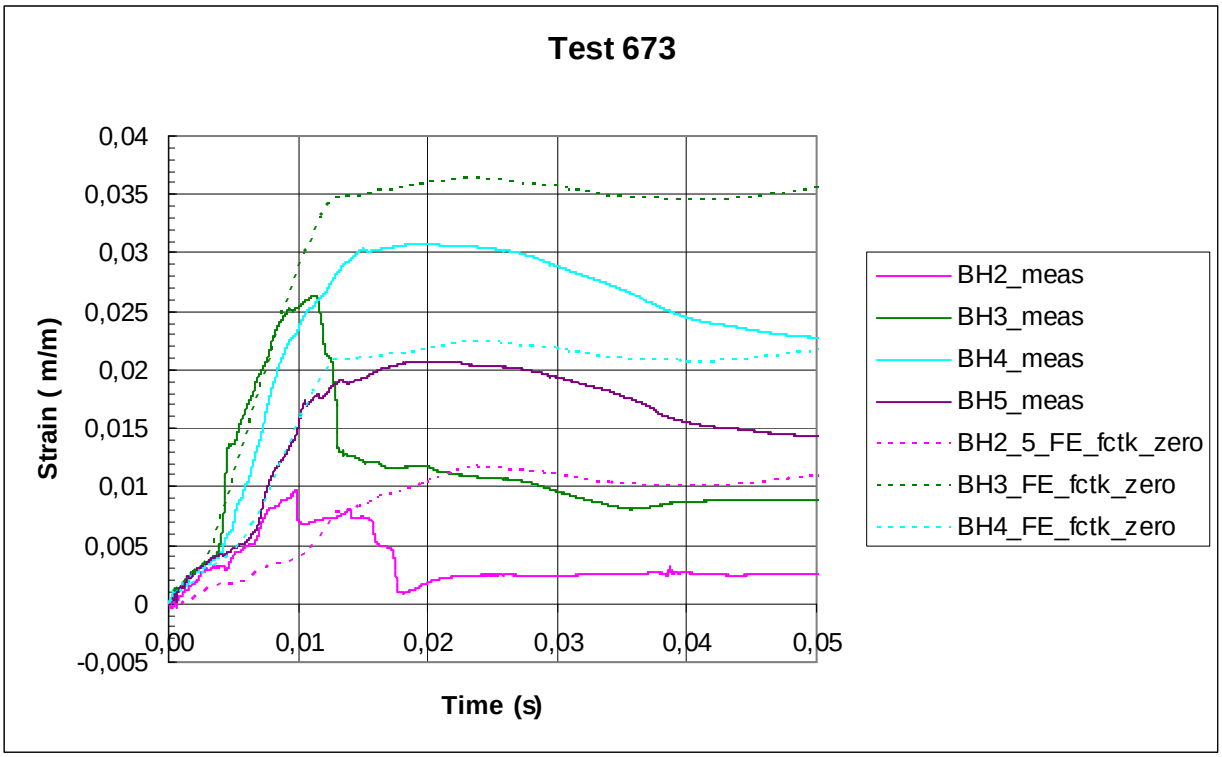

Figure 95. Measured and calculated strains in the reinforcement at locations BH2, BH3, BH4 and BH5 in Test 673.

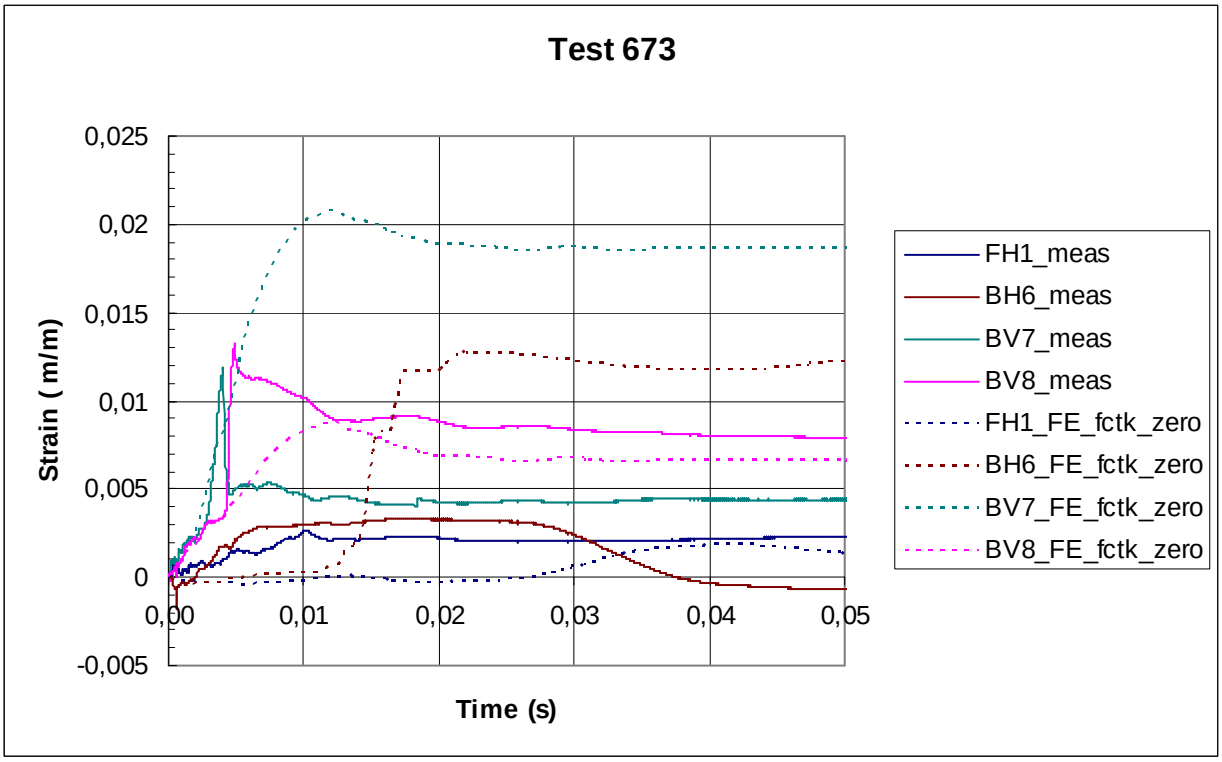

Figure 96. Measured and calculated strains in the reinforcement at FH1, BH6, BV7 and BV8 in Test 673.

4.8 Test 650

4.8.1 Shell element analyses of Test 650

Test 650 was a repeat for Test 644. The loading function is shown in Figure 36 (almost the same as in Test 644). The nonlinear material properties used in this study are presented in Section 4.1. Energy balance was maintained during the calculation as shown in Figure 97. The locations for displacement sensors are shown in Figure 98. The calculated and measured displacements are presented in Figure 99. The shell element analysis underestimates somewhat the deflection. The measured and calculated strains in reinforcement are presented in Figure 100 and in Figure 101. In this test, the strain measurements in reinforcement were not as successful as they were in test 644. The calculated strains monitored at the strain gauge locations are all presented in Figure 102 as functions of time.

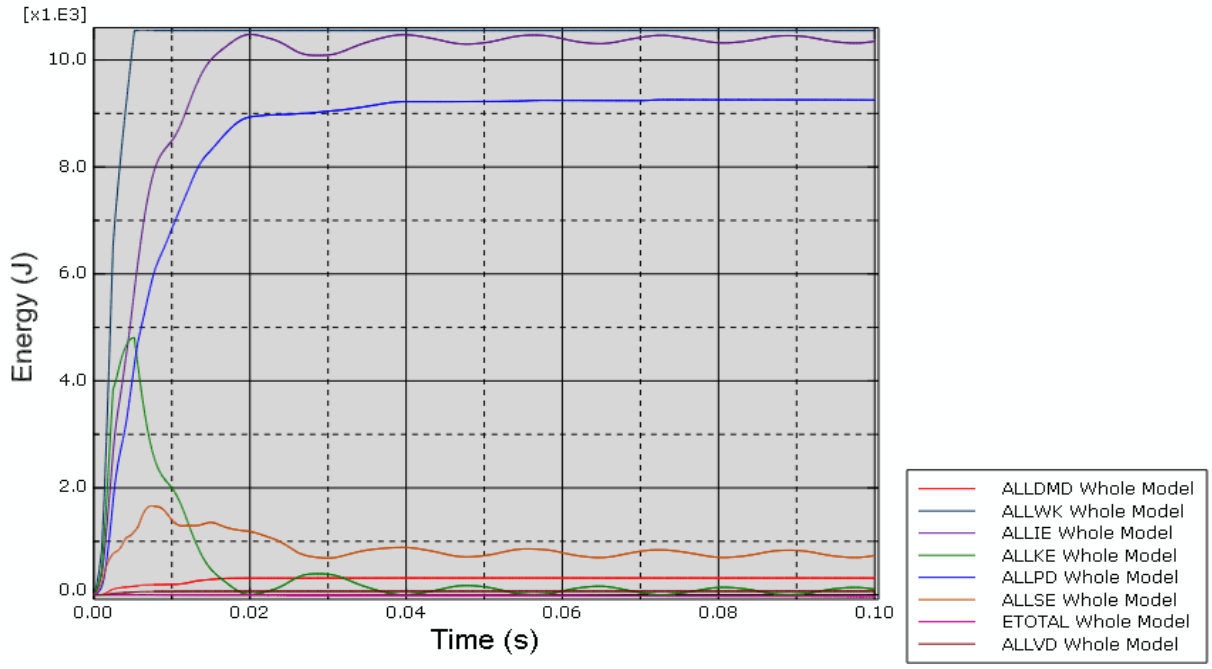

Figure 97. Energy balance during the calculation in Test 650.

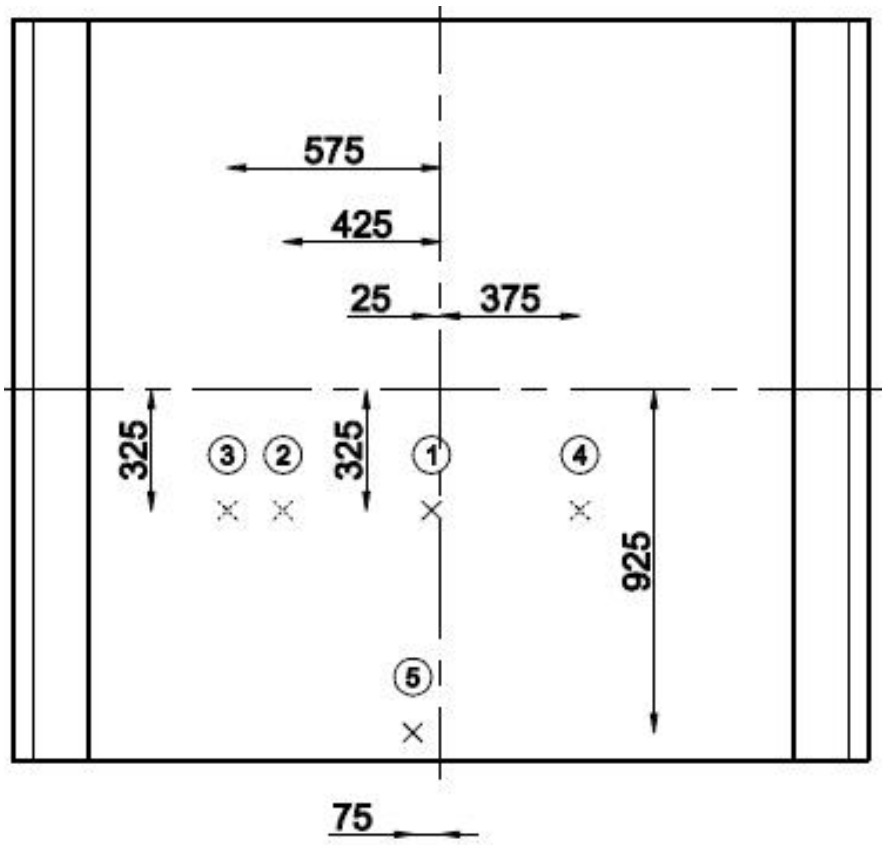

Figure 98. Locations of displacement sensors in Test 650.

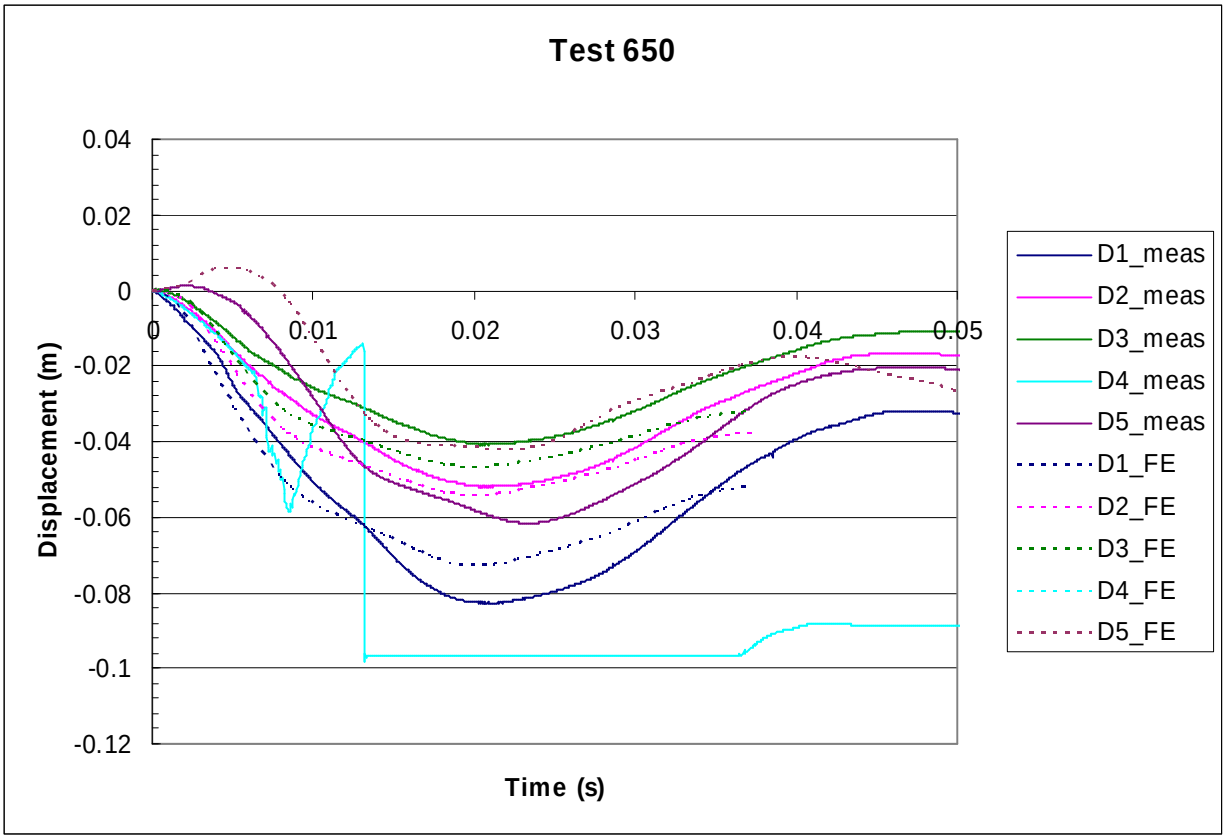

Figure 99. Measured and calculated displacements as functions of time in Test 650.

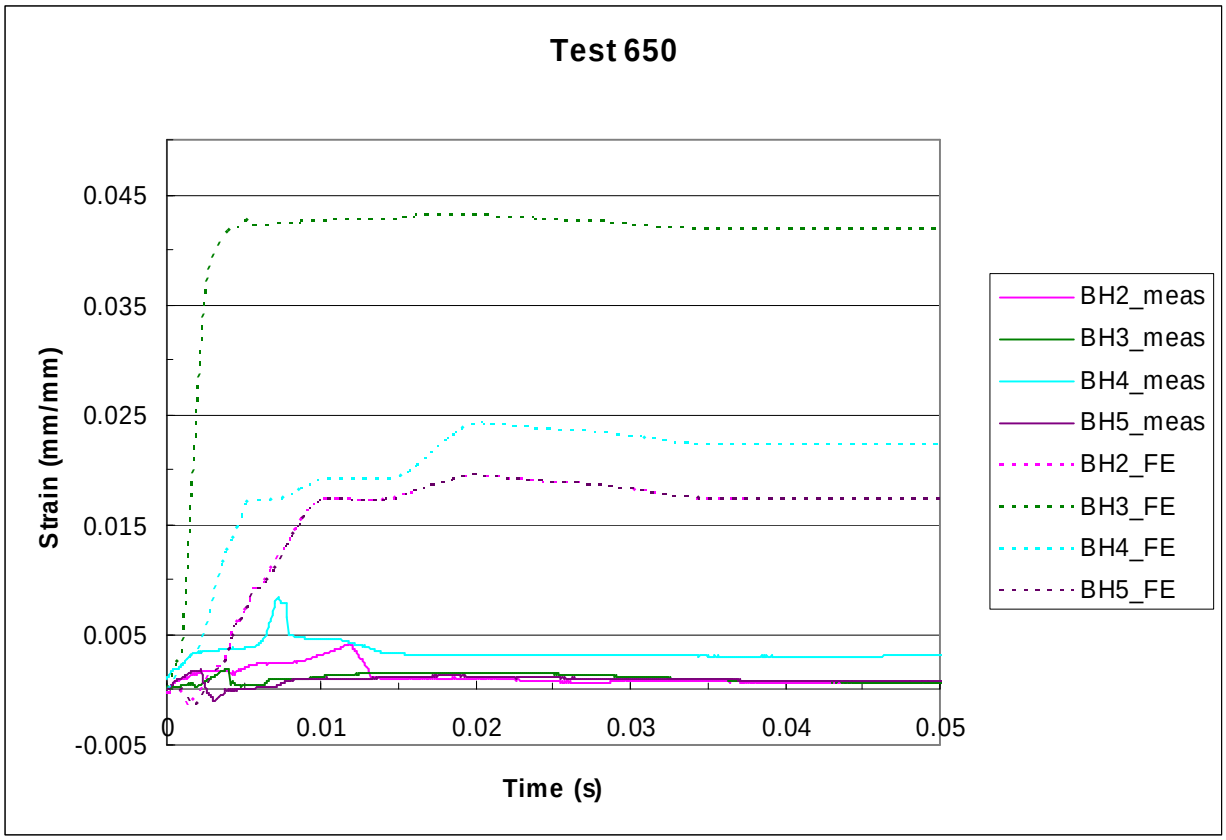

Figure 100. Measured and calculated strain in the reinforcement at locations BH2-5 in Test 650.

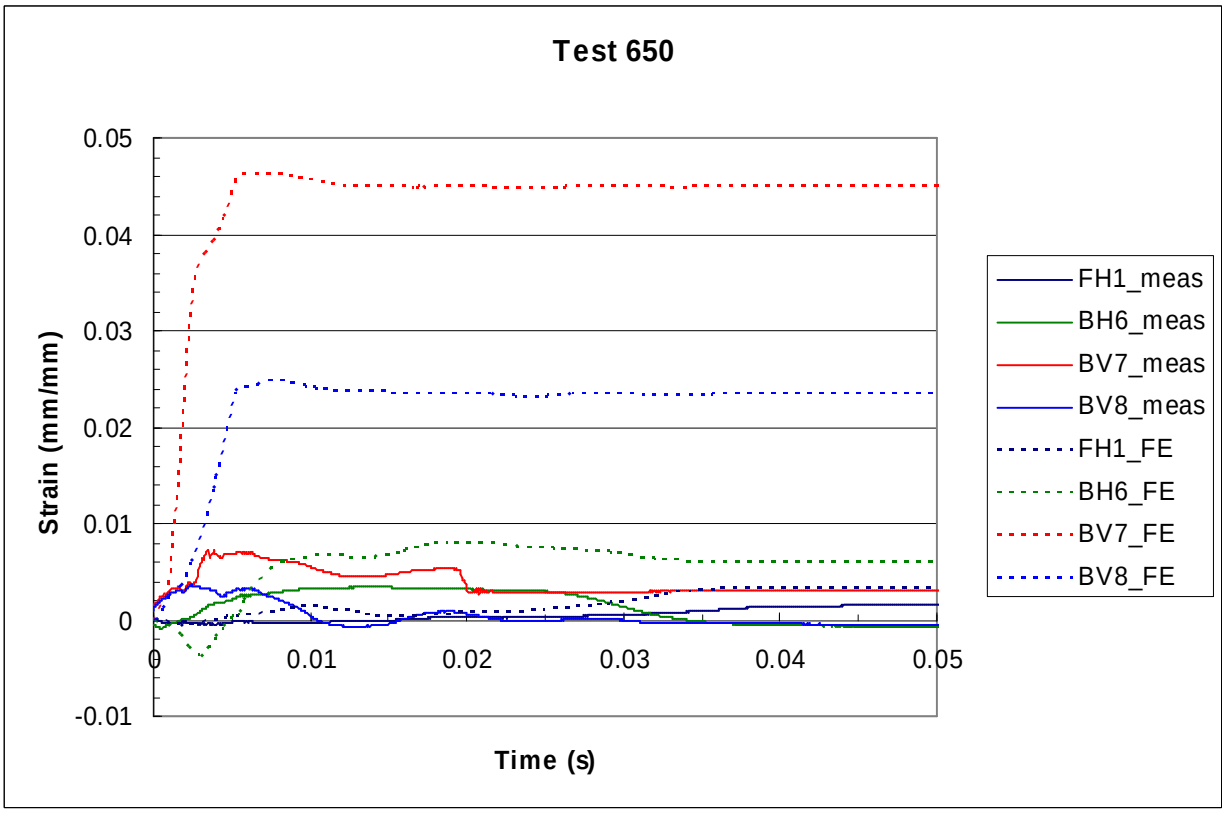

Figure 101. Measured and calculated strain in the reinforcement at FH1, BH6 and BV8 in Test 650.

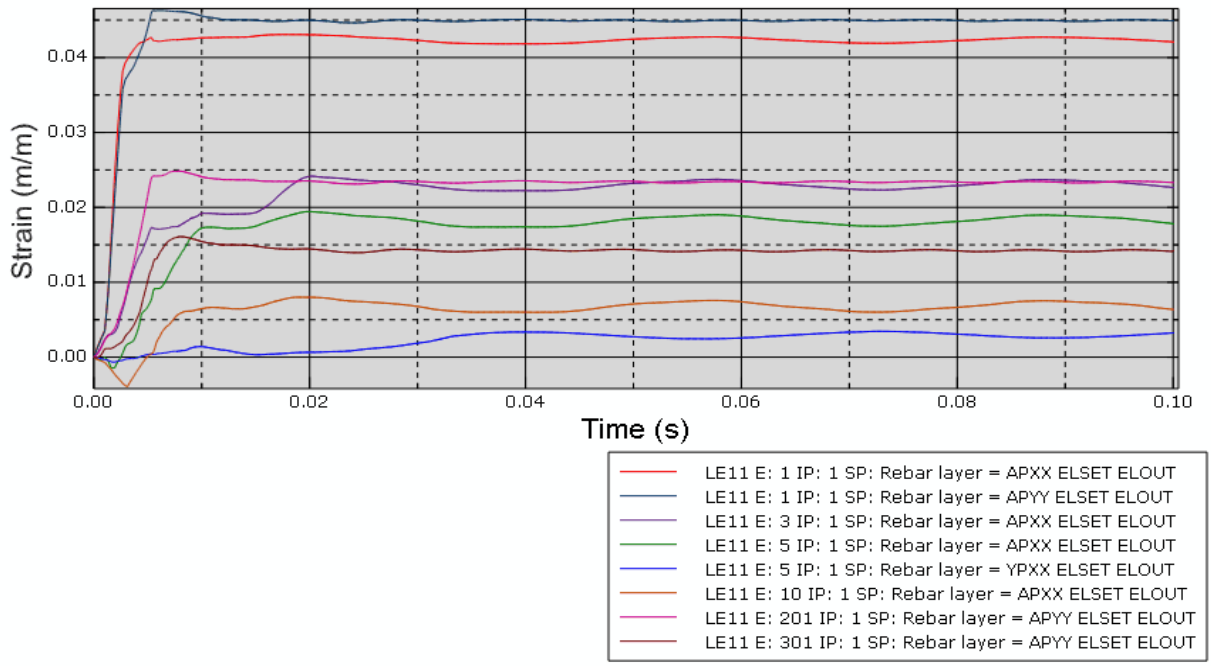

Figure 102. Calculated strains in rebars as a function of time in Test 650.

The front surface of the wall after the test is shown in Figure 103 and a part of the back surface is depicted in Figure 104. A quarter section of the test wall 650 cut at the centre line is shown in Figure 105.

Figure 103. The front side of the wall after Test 650.

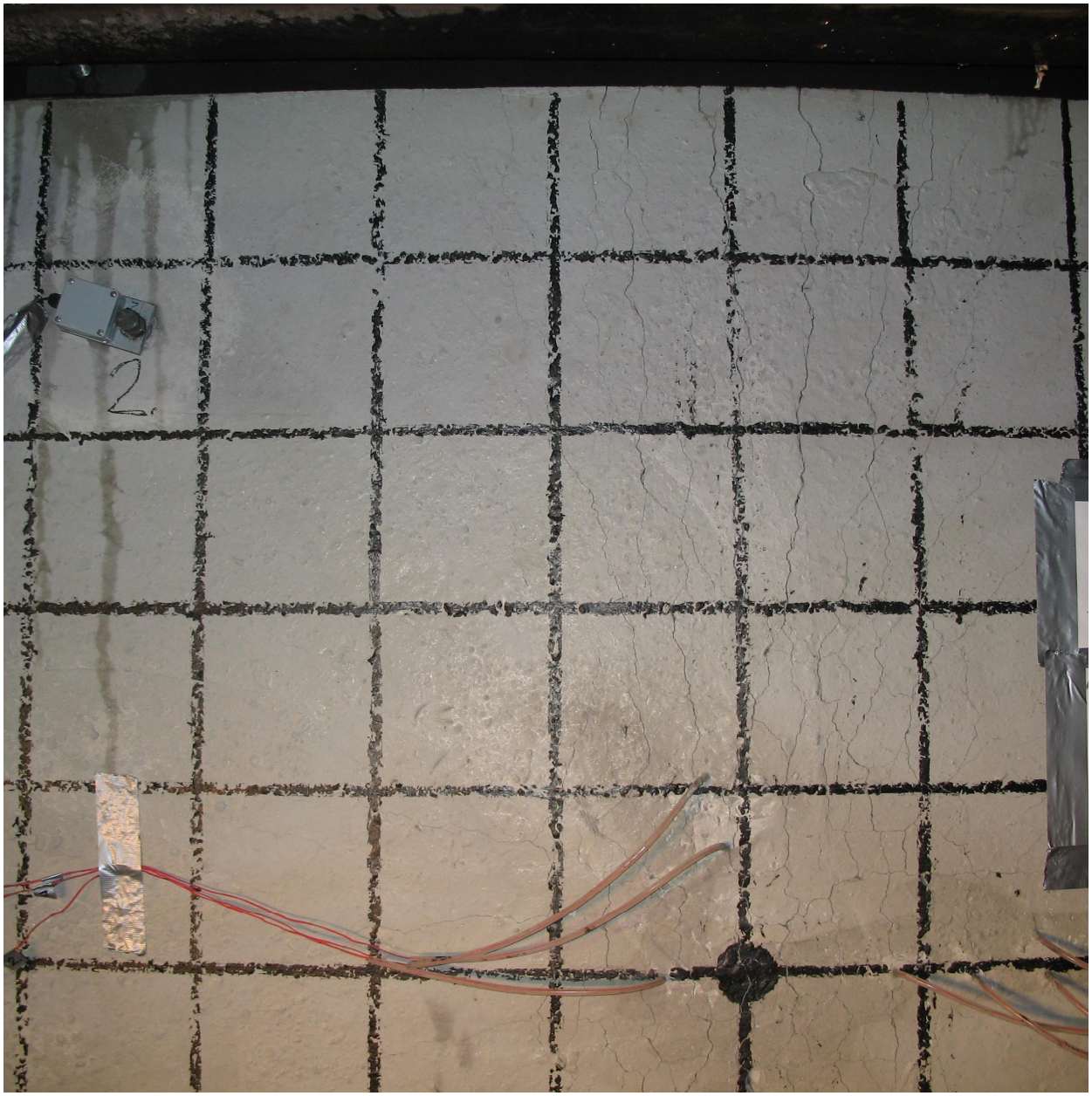

Figure 104. The back side of the wall after Test 650.

Figure 105. Quarter section of the test wall 650 cut at the centre line.

Plastic strain distributions in the horizontal and vertical back surface reinforcement are presented in Figure 106 and in Figure 107. The plastic strain in the vertical reinforcement is higher than in the horizontal back surface reinforcement. This can also be seen in Figure 102, where the curve titled APXX for element E:1 presents the strain value in the horizontal reinforcement and APYY for element E:1 shows the strain as a function of time in the vertical back surface reinforcement.

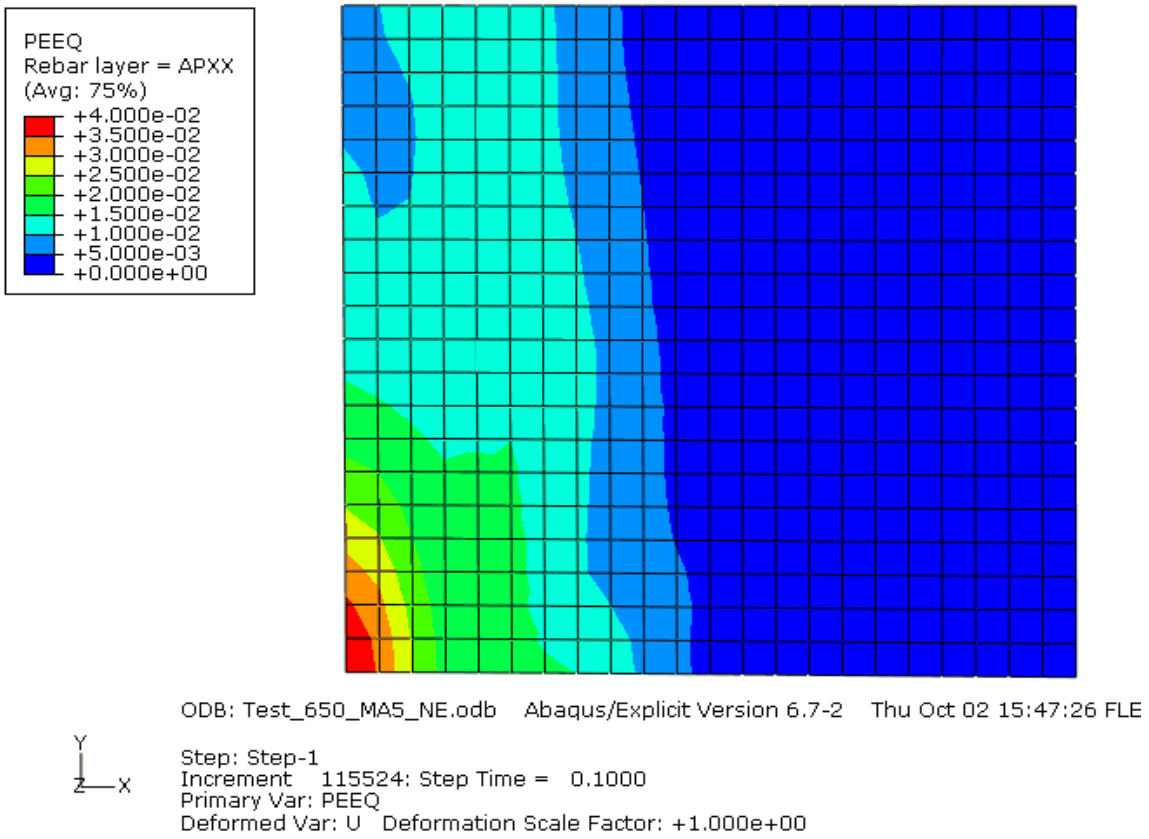

Figure 106. Plastic strain distribution in horizontal back surface reinforcement in Test 650.

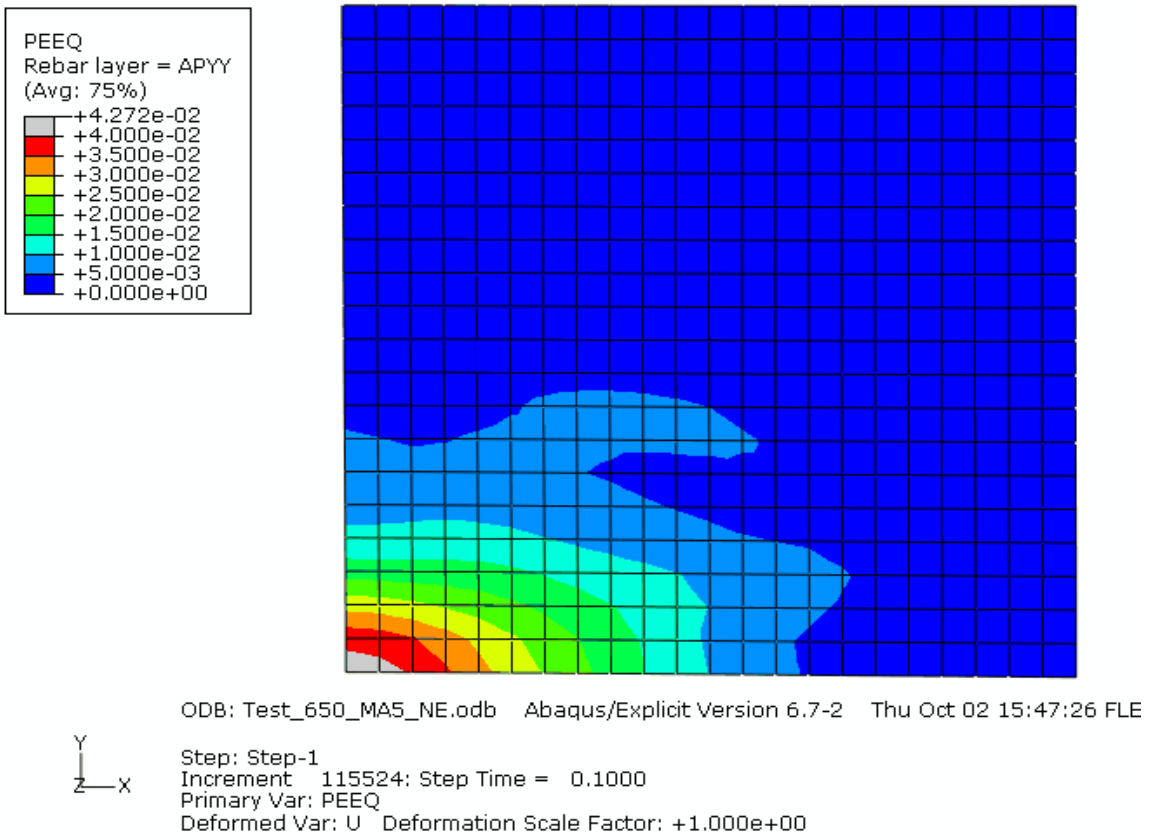

Figure 107. Plastic strain distribution in vertical back surface reinforcement in Test 650.

4.9 Comparison of some test and analysis results

In this chapter, some results of the one-way 15 cm thick slab tests and corresponding analyses with different methods are summarised and compared with each other.

The measured and the corresponding calculated wall deflections in Tests 642, 644 and 673 are shown in Figure 108, Figure 109 and in Figure 110, respectively. It can be seen that the maximum deflection value can be calculated accurately. The vibration of the damaged wall was not predicted that well. The frequency of the oscillation is nearly the same for both Abaqus models, approximately 36 Hz for the model without the frame ("Abaqus shell", dark blue lines) and approximately 34 Hz for the model with the frame ("Abaqus shell+beam", red lines). The corresponding measured frequency (thick cyan line) is approximately 20 Hz. The two-degrees-of-freedom model ("TDOF", dotted brown line) behaves very similarly to the Abaqus model without the supporting structure. The results are either from the centre of the wall ("Dmax") or from the displacement sensor location D1 (see Figure 37 or Figure 81). LS-DYNA gives somewhat different kinds of results.

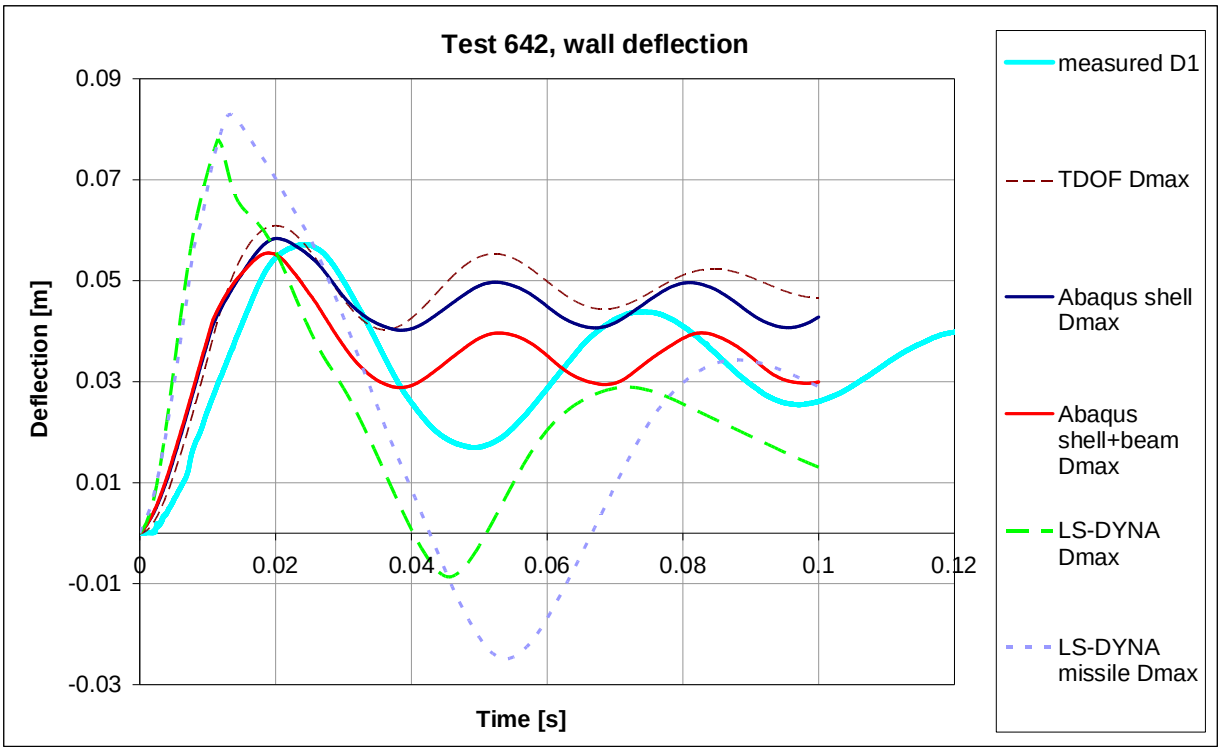

Figure 108. Measured and corresponding calculated wall deflections in Test 642.

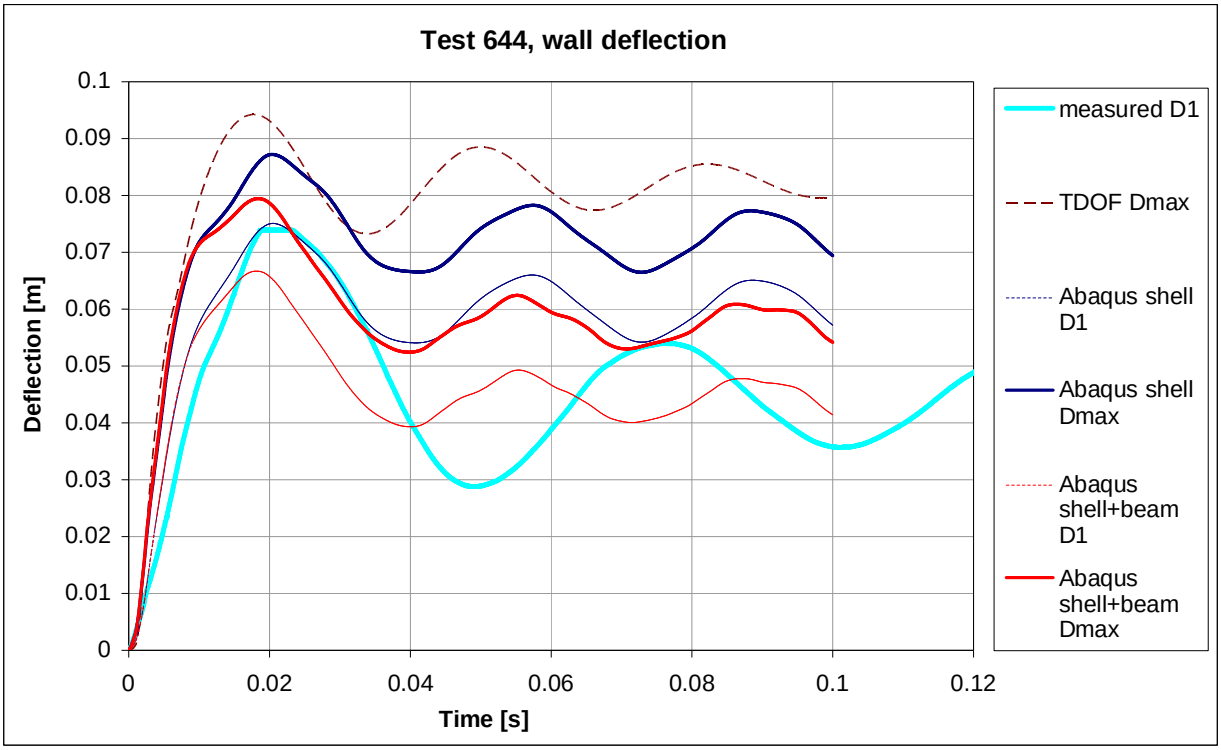

Figure 109. Measured and corresponding calculated wall deflections in Test 644.

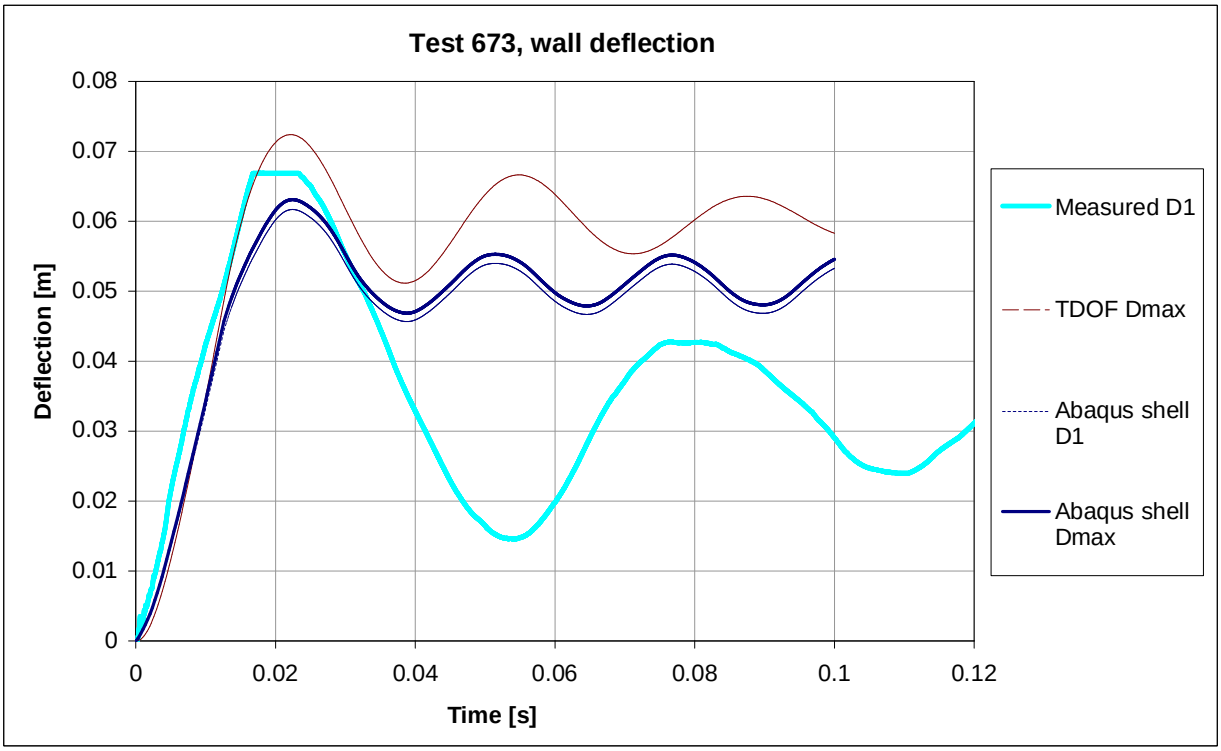

Figure 110. Measured and corresponding calculated wall deflections in Test 673.

Figure 111 shows the load time function ("load") according to the Riera method, and used in simulations, the reaction force measured from the back pipes ("back pipes") and the calculated reaction at the end of the back pipes ("Abaqus shell+beam") for both tests. As can be seen, the missile filled with water (blue curves) has a much higher force peak than the empty one (red curves). Respectively, the measured reaction force has also slightly higher peak values, but the forces are clearly evened out within the distance the stress wave travels through the wall and its supporting structure. The calculated reaction force corresponds relatively well to the measured one in case of Test 642, but in case of Test 644 simulation, the impact seems to hit a resonance point and the reaction force starts to strongly vibrate. However, there has not been any clear sign of water hammer effect with the water filled missiles.

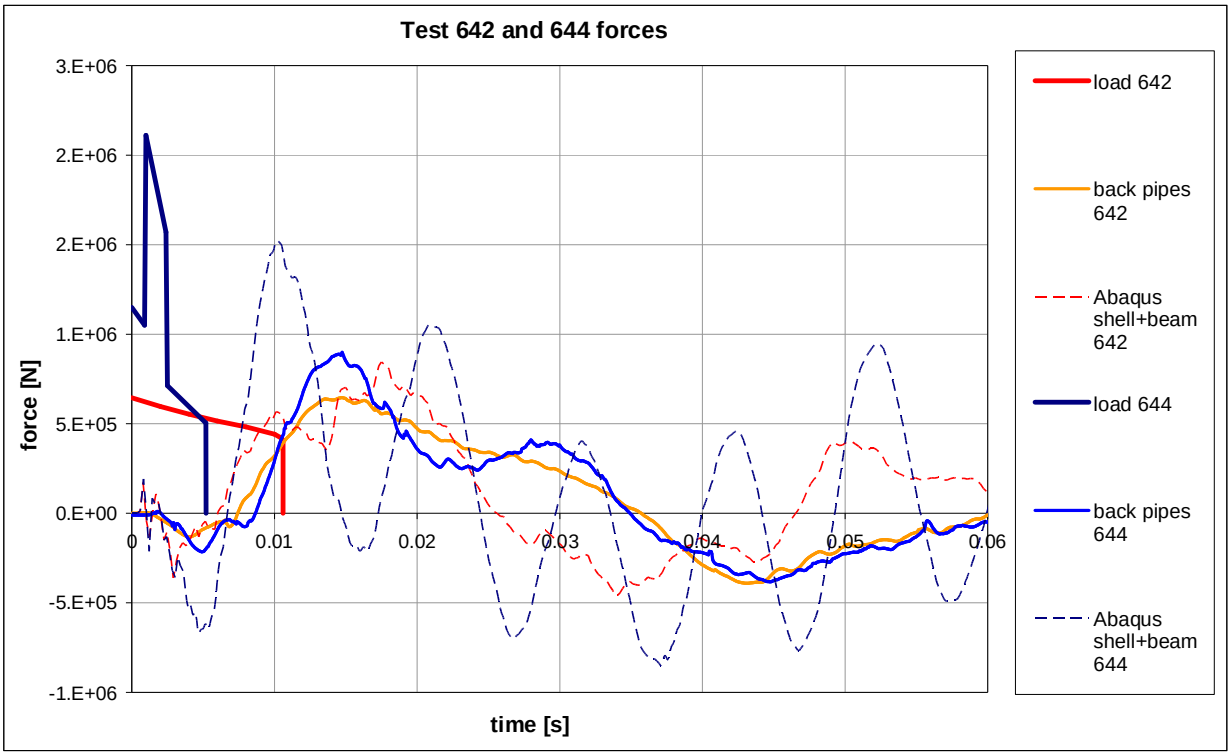

Figure 111. The load time function (load), the measured reaction force in the back pipes forces (back pipes) and the calculated reaction at the end of the back pipes (Abaqus shell+beam).

The main analysis results are collected in Table 8. The impulse in Test 642 was higher but the calculated maximum displacement was considerably smaller than the corresponding results obtained in the wet missile Tests 644 and 650. This is in agreement also with the experimental findings. This is due to the fact that the aluminium missile behaves more like a deformable missile. Besides the contained water, also the rather stiff steel rail below the water missile affects the impact load.

According to the calculations, the maximum strain, by a clear margin, occurred in the horizontal reinforcement in Test 642. This is due to the fact that the wall loaded by the deformable empty missile behaves like a wide bending beam. In tests where the water missile was used, the calculated strain values in the vertical back surface reinforcement were nearly as high as in the horizontal back surface reinforcement.

The displacement due to bending was quite well calculated using finite element shell models for Tests 663 and 673. Especially, the results calculated by assuming the tensile strength to decrease down to zero after cracking were quite close to the experimental finding. This

assumption did not considerably affect the results calculated for Tests 642, 644 and 650. This is believed to be due to the fact that tensile cracking was in these tests less extensive than in Tests 663 and 673.

Results presented in Table 8 for simplified method are calculated by assuming a non-diagonal damping matrix. Structural behaviour of the impact loaded walls could be rather well predicted with the simplified method when the more consistent non-diagonal damping matrix was used. It should be noted that in the original CEB method (CEB, 1998) the damping is assumed to be diagonal and by this assumption also the damper of the cone is assumed to be fixed to the ground. More correct assumption would be to fix the damping element of the cone to the wall.

It should be noted that there were some uncertainties in defining the loading function for the numerical analyses. Due to some uncertainties in measurement recording, measured force-time functions were not available. When calculating the loading with the Riera method, the crushing force dominates the force-time function. The collapse mechanism of the aluminium pipe was not clearly of folding type but in some cases also unstable tearing occurred. Also the contribution of the steel rails below the water missiles causes uncertainties in predicting the loading.

Table 8. Summary of experimental and numerical results.

Test number	**642 (DRY)**	**663(DRY)**	**673(DRY)**	**644(WET)**	**650(WET)**
Velocity (m/s)	109	129	127	105	105
Impulse (Ns)	5630	6230	6400	5344.5	5292
Collapse mode	bend	bend	bend	bend	bend
D1 (m)	0.057	0.07	0.07	0.075	0.08
Calculated results					
FE **D1 (m)** **Dmax (m)** **Strain (%)**	 0.058 3.2	 0.058 3.0	 0.062 0.064 3.0	 0.075 0.087 4.6	 0.073 0.084 4.3
FE f_{ctk_zero} **D1 (m)** **Dmax (m)**	 0.059	 0.063 0.067	 0.068 0.07	 0.075 0.087	 0.076 0.086
Simplified Dmax (m)	0.061	0.069	0.072	0.09… 0.12	

5 General study on numerical simulation of prestressed concrete walls

This chapter deals with the numerical modelling of prestressed concrete walls. Prestressed concrete is a method for overcoming the concrete's natural weakness in tension. It can be used to produce beams, floors or bridges with a longer span than is practical with ordinary reinforced concrete. Prestressing tendons (generally of high tensile steel cable or rods) are used to provide a clamping load which produces a compressive stress that offsets the tensile stress that the concrete compression member would otherwise experience due to a bending load.

Prestressing is usually done internally inside the concrete cross-section and can be accomplished in three ways: (1) pre-tensioned concrete, and (2) bonded or (3) unbonded post-tensioned concrete (Nawy, 1989) (Nilson, 1987).

1. Pre-tensioned concrete is cast around already tensioned tendons. This method produces a good bond between the tendon and concrete.

2. Bonded post-tensioned concrete is the descriptive term for a method of applying compression after pouring concrete and the curing process (in situ). The concrete is cast around a plastic, steel or aluminium curved duct, to follow the area where otherwise tension would occur in the concrete element. A set of tendons are fished through the duct and the concrete is poured. Once the concrete has hardened, the tendons are tensioned by hydraulic jacks that react against the concrete member itself. When the tendons have stretched sufficiently, according to the design specifications, they are wedged in position and maintain tension after the jacks are removed, transferring pressure to the concrete. The duct is then grouted to protect the tendons from corrosion.

3. Unbonded post-tensioned concrete differs from bonded post-tensioning by providing each individual cable permanent freedom of movement relative to the concrete. To achieve this, each individual tendon is coated with grease (generally lithium based) and covered by a plastic sheathing formed in an extrusion process. The transfer of tension to the concrete is achieved by the steel cable acting against steel anchors embedded in the perimeter of the slab. The main disadvantage over bonded post-tensioning is the fact that a cable can destress itself and burst out of the slab if damaged.

External prestressing is defined as prestress introduced by the high strength cable, which is placed outside the cross section and attached to the beam at some deviator points along the beam. This usually makes the analysis of a beam more complicated. One analysis type for external prestressing is proposed by Diep and Umehara (Diep, 2002).

All these three ways of accomplishing prestressing can be numerically simulated with finite element method, although the second way is clearly the easiest one in that respect. In case of the first method, in principal, the hardening of the concrete and the interaction between the concrete and tendons that is changing during the hardening process should be modelled, and that is very complicated. In case of the third method, the concrete and the tendons have to be modelled as completely separate parts and the contact between the tendons and the duct (or the concrete) should be defined. In case of the second method, if the case is static and the displacements remain relatively small, there is a perfect bond with virtually no slip of the

tendons. The tendons can then be modelled as rigidly fixed to the concrete, their nodes sharing the same degrees of freedom with the nearest nodes of concrete elements.

There are many ways of simulating the prestressing with finite element method depending on the prestressing type (described above) and also the FE model (especially the dimensionality) and element type. The model can be in one, two or three dimensions. The element type of the concrete itself can either be solid or structural shell (or continuum shell) or even beam element in some simple cases. The tendons can be modelled as beam/truss elements, as a membrane or as an element property (smeared layers inside element sets).

The bond between steel bars and concrete is an important part of the reinforced concrete mechanical system. Due to its significance for practical design, bond has been investigated by many researchers and technical committees, e.g. (FIB2000, 2000). This effort has resulted in numerous empirical formulas and complex code provisions for bar anchoring length and reinforcement detailing. This knowledge is mainly utilized in practical design, but it can also serve as a basis for constitutive models in numerical analysis. Despite this, bond slip is typically neglected and a perfect connection between concrete and reinforcement bars is assumed in most numerical nonlinear analyses of reinforced concrete structures in engineering practice (Jendele, 2006).

Although this approach is usually appropriate, there are cases in which the effect of bond slip cannot be neglected. Currently, various methods to account for this phenomenon exist. Recently, a number of researchers proposed sophisticated bond models that are based on detailed three-dimensional analysis of the interaction between concrete and bars. The common characteristic of those approaches is that they use 3D models of concrete and reinforcement with two-dimensional interfaces between them. Such a theory was chosen, e.g. by Lundgren (Lundgren, 1999), who developed an interface bond model based on plasticity theory with fully three-dimensional features.

The advantage of these approaches is that the interfacial behaviour can be described using established material modelling methods, e.g. plasticity. Debonding as well as dilatancy and other bond characteristics can be accurately modelled as well. However, for practical analysis of reinforced concrete structures, this approach is not very appealing, because it requires extremely large computational capacity. In addition, the development of appropriate finite element meshes is not straightforward, as it is not supported by existing automatic mesh generation tools.

In bond behaviour, two sources of slip and consequently two models, can be recognized (FIB2000, 2000): slip due to damage in concrete adjacent to bars exhibited by cracking and crushing, and slip of the interface between steel bar and surrounding concrete. The former model deals with the behaviour of a solid in relatively larger volume of material, while the later model considers a fictitious interface layer. In the study of Jendele and Cervenka, an interface model of slip was added to the existing set of material models (Jendele, 2006). The developed model was implemented in FEM package ATENA (Cervenka Consl., 2002). The formulation for embedded bar element was extended in a way that it includes a bond element. The system includes three types of finite elements: concrete continuum element (2D or 3D), bar truss element (constant strain) and bond element (constant slip). A new degree of freedom was introduced, which represents the bond slip. It is the difference between concrete and bar displacements on the element boundary.

Generally, the same modelling procedures as are used for the normal reinforcement bars can be used for prestressing tendons in finite element method. The most common way in Abaqus

program is to employ the smeared rebar approach in which the calculation of reinforcement stresses is separated from the calculation of concrete stresses, and the two components are smeared together according to their relative cross-sectional areas to form the total element stress. In Abaqus this is done using keywords

*REBAR LAYER (the preferred option)

or

*REBAR (the older option)

The prestress is applied using keyword

*INITIAL CONDITIONS, TYPE=STRESS, REBAR

and defining the elements on which the prestress will be applied and the prestress value on the data line. When performing an Abaqus/Standard analysis, some iteration will usually be needed in this case to establish a self-equilibrating stress state in the rebar and concrete.

Another and a more realistic way is to model each prestressing tendon with truss or beam elements. The most suitable element type depends on the tendon type, loading case (displacement magnitude) and how the tendon is connected to the surrounding structure. Usually truss elements are sufficient, since the bending stiffness of the bars is not essential and usually almost negligible. In case of bonded post-tensioned tendons, it is adequate to embed the truss elements throughout their whole length within the concrete elements. One way is to let those elements share exactly the same nodes. In that case, the tendons have to follow the concrete element mesh (or usually vice versa, since the tendon position is likely to be more important). In that case, both shell and solid volume elements can be used for the concrete. Another almost similar but conveniently a more automatic way is supported by Abaqus.

Keyword

* EMBEDDED ELEMENT

is used to specify an element or a group of elements that lie embedded in a group of “host” elements in a model. Abaqus searches for the geometric relationships between nodes of the embedded elements and the host elements. If a node of an embedded element lies within a host element, the translational degrees of freedom at the node are eliminated and the node becomes an “embedded node.” The translational degrees of freedom of the embedded node are constrained to the interpolated values of the corresponding degrees of freedom of the host element. Embedded elements are allowed to have rotational degrees of freedom, but these rotations are not constrained by the embedding. Multiple embedded element definitions are allowed. The host elements have to be of solid volume type (2D or 3D).

There are also other ways of connecting the truss elements to the structure such as defining linear multi-point constraints in the form of an equation by keyword

*EQUATION

or imposing mesh tie constraints by keyword

*TIE

The contact between two between two bodies both in normal and tangential direction is usually defined by different types contact formulations between the element surfaces. However, that is

not possible with string-type geometries such as parts meshed with truss elements and the preferred method is to use contact elements. Abaqus/Standard offers a variety of contact elements that can be used when contact between two bodies cannot be simulated with the surface-based contact approach. Gap contact elements can, for example, be used to model an inextensible cable that supports only tensile loads. Slide line contact elements can, for example, be used to model threaded connectors. The contact is necessary to take into account when the post-tensioning cable is unbonded but runs through the structure in a way that it pushes the duct wall and deforms the shape of the concrete structure such as in case of normal unbonded post-tensioning of a bridge or cylindrical containments. This type of contact is also necessary in bonded post-tensioning if there is significant amount of slipping of the tendons.

The prestress can be applied to the truss elements in the same manner than to the smeared rebars using keyword

```
*INITIAL CONDITIONS, TYPE=STRESS, REBAR
```

(Abaqus, 2007).

5.1 Modelling of Dywidag prestressing

The components of the DYWIDAG Bar System have been used worldwide since 1965. The system provides a simple, rugged method of efficiently applying prestress force to a wide variety of structural applications including post-tensioned concrete as well as rock and soil anchor systems. The DYWIDAG Bar System is primarily used for grouted construction. In addition, they are sometimes used as external tendons with various types of corrosion protection. In IMPACT project, 250 mm thick reinforced concrete walls were shot with relatively hard missiles. Some of those walls had shear reinforcement and some were prestressed with Dywidag bars. The public tests are listed in Table 9. The impact velocity of the missile was approximately 100 m/s in all those tests.

DYWIDAG threadbars are stressed using compact lightweight hydraulic jacks. In most cases handled by one man, the jack fits over a pull rod designed to thread over the threadbar protruding from the anchor nut. The jack nose contains a socket wrench and ratchet device which allow the nut to be tightened as the threadbar elongates.

Grouting completes the installation process for post-tensioned concrete construction. The grout is important in protecting the steel from corrosion and contributes significantly to the ultimate strength of the structure. However, in the tests of IMPACT project the grouting is not used and the Dywidag bars are left to freely move inside the ducts (DSI America, 2008).

Dywidag type of prestressing is modelled with a simple test model both as a bonded and as an unbonded case. Table 10 shows the bar properties found in the manufacturer's website (DSI UK, 2008). Figure 112 shows the stress-strain curve derived from that information and used in the simulations. Young's Modulus is 205 GPa for the Dywidag bars and 35 GPa for the concrete in these simulations.

Table 9. Tests with 250 mm concrete walls.

Test code and number	Dywidag bars	Shear reinforcement
A1 (678)	**none**	**no**
AT (699)		**yes (T-bars)**
B1 (685)	**compression in concrete 5 MPa after post-tensioning**	**no**
BT (700)		**yes (T-bars)**
C1 (690)	**compression in concrete 10 MPa after post-tensioning**	**no**
CT (701)		**yes (T-bars)**

Table 10. Dywidag steel properties (DSI UK, 2008).

Nominal Diameter	Steel Grade	Ultimate Strength f_{pu}	0.10 % (a) Proof Strength	70 % (b) Ultimate Strength	50% Ultimate Strength	Cross Sectional Area	Diameter over Threads	Thread Pitch	Bar Weight
mm	N/mm^2	kN	kN	kN	kN	mm^2	mm	>mm	kg/m
15	900/1100	195	159	136	98	177	17	10	1.44
20	900/1100	345	283	241	173	314	23	10	2.56
26.5	**950/1050**	**579**	**523**	**405**	**290**	**551**	**30**	**13**	**4.48**
32	950/1050	844	764	591	422	804	36	16	6.53
36	950/1050	1069	967	748	535	1018	40	18	8.27
40	950/1050	1320	1194	924	660	1257	45	20	10.21
47	950/1050	1822	1648	1275	911	1735	52	21	14.1

(a) 0.1% Proof Stress also referred to, in general terms, as Yield Strength - T_y.

(b) For geotechnical applications 75% f_{pu} may be used for proof testing.

Modulus of Elasticity: E = 205,000 N/mm^2 ± 5%.

Stock Lengths: 15mm diameter bars, 6.0m; 20mm - 47mm diameter bars, 12.0m. Tolerances ± 100mm.

All bar diameters can be cut to length to suit customer requirements.

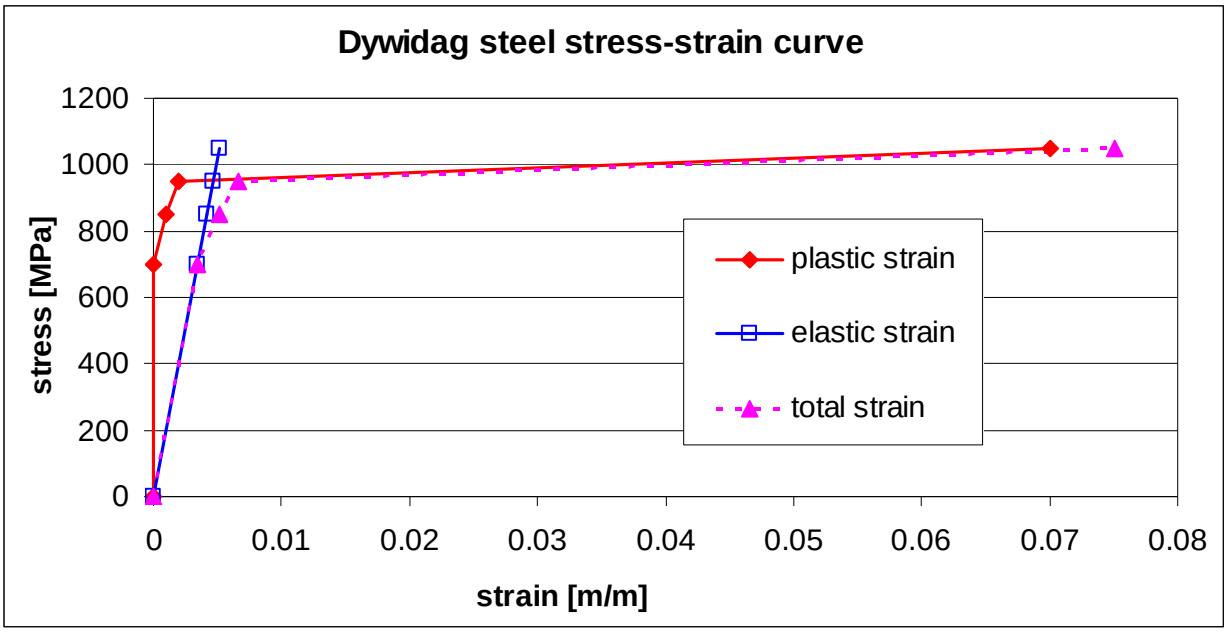

Figure 112. Dywidag steel stress-strain curve.

The used FE models represent the prestressed IMPACT test wall. First a shell element model with 484 elements is used. There is 9 integration points through the thickness (0.25 m) of the wall. The Dywidag bars and normal longitudinal reinforcement are defined in the same manner under the same keyword:

```
*Rebar Layer
dywidag-x,    0.0005515,  0.18,  0.,    dywidag,  0.,   1
dywidag-y,    0.0005515,  0.18,  0.,    dywidag,  90.,  1
rebar-yx,     7.854e-05,  0.09,  0.1,   rebar,    0.,   1
rebar-yy,     7.854e-05,  0.09,  0.09,  rebar,    90.,  1
rebar-ax,     7.854e-05,  0.09,  -0.1,  rebar,    0.,   1
rebar-ay,     7.854e-05,  0.09,  -0.09, rebar,    90.,  1
```

In this way, there is a perfect bond between the bars and the concrete. First a static case was studied. It consisted of two steps that both lasted 1 second. The model can be seen in Figure 113. Initially, the Dywidag bars were stressed to 900 MPa of tension. It corresponds to 496 kN tensile force in the tendon. Figure 114 shows horizontal stress in concrete and longitudinal stress in reinforcement bars near the centre of the slab. Figure 115 shows the equivalent plastic strain in reinforcement bars near the centre of the slab.

During the first step, the bars relaxed from 900 MPa to approximately 780 MPa and part of the force was taken by concrete which got compressive stresses (negative values) of approximately 9 MPa by magnitude. In the legend, light blue curve (SPOS) represents concrete stress near the front surface and the red curve (SNEG) represents concrete stress near the rear surface. In fact, Figure 113 shows how von Mises stress in the middle concrete layer is 9.26 MPa throughout the wall after the first step. The normal reinforcement gets approximately 50 MPa compressive stresses.

During the second step, an even pressure to the whole front surface was ramped up to 1.5 MPa. The static limit load is approximately 1 MPa for this wall and the purpose was to have some plastic strain in the reinforcement. Geometric nonlinearity was taken into account in the analysis. Stresses in front surface rebars increased to 200 MPa of compression. Stresses in rear surface rebars turned to tensile up to 300 MPa. The yield point is 535 MPa. Front surface

concrete stresses returned to zero while rear surface stresses increased to 40 MPa of compression. Dywidag stresses stayed first steadily in 780 MPa but began to increase when the deformation of the slab moved the Dywidag bars off the neutral axis of the slab. Figure 115 shows how the Dywidag bars yield during both steps (though only very slightly), but the normal reinforcement bars still stay elastic.

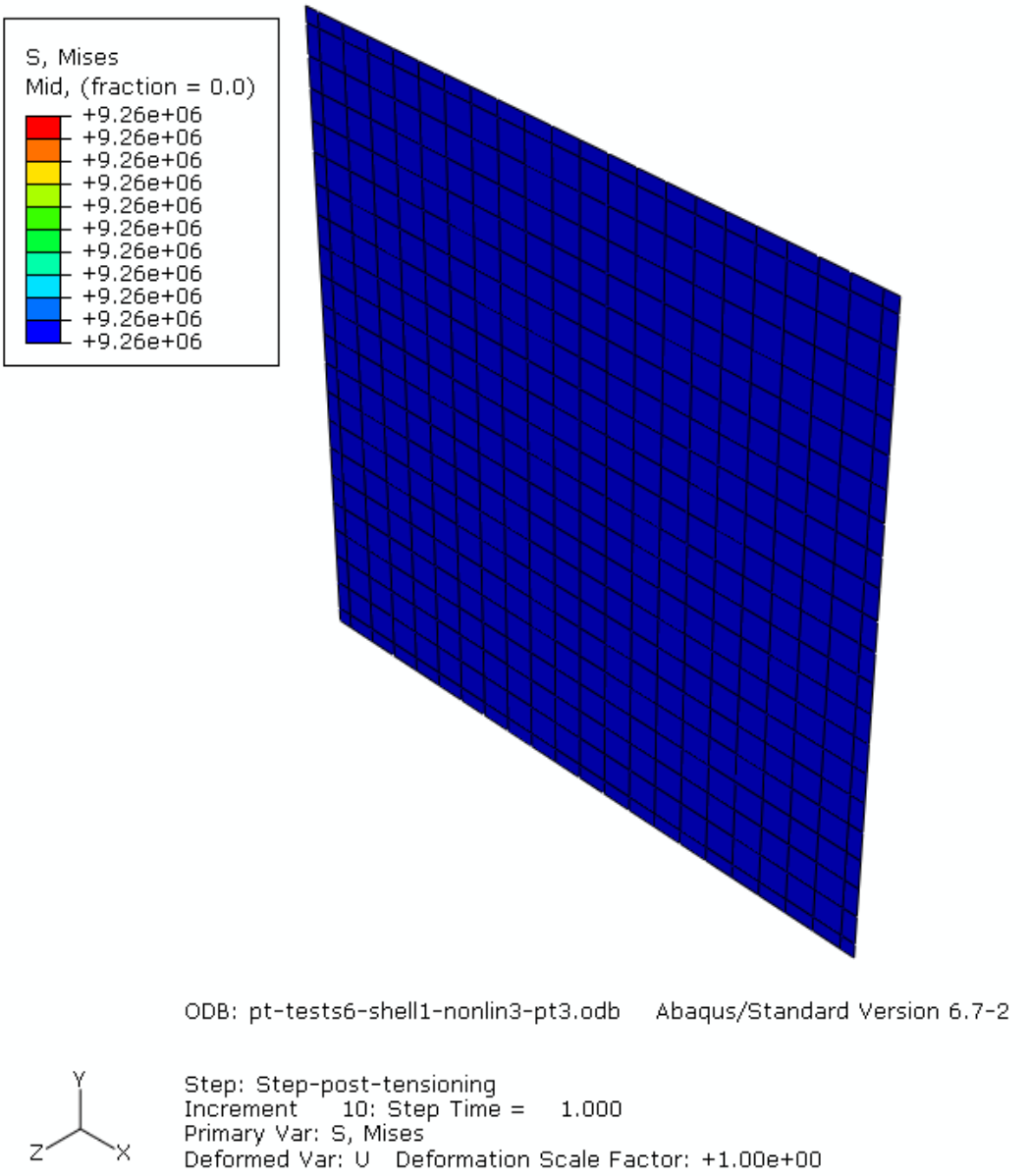

Figure 113. Von Mises stresses in the middle layer of the slab (9.26 MPa everywhere).

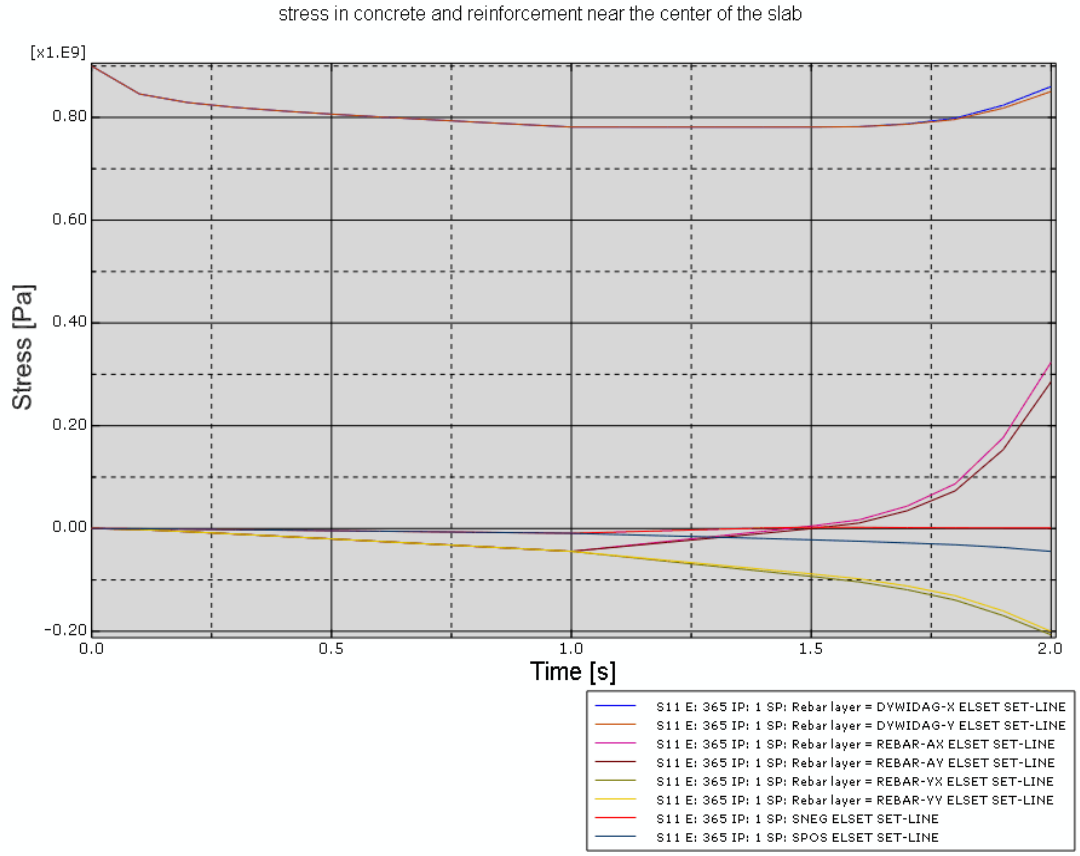

Figure 114. Stress in concrete and reinforcement near the centre of the slab.

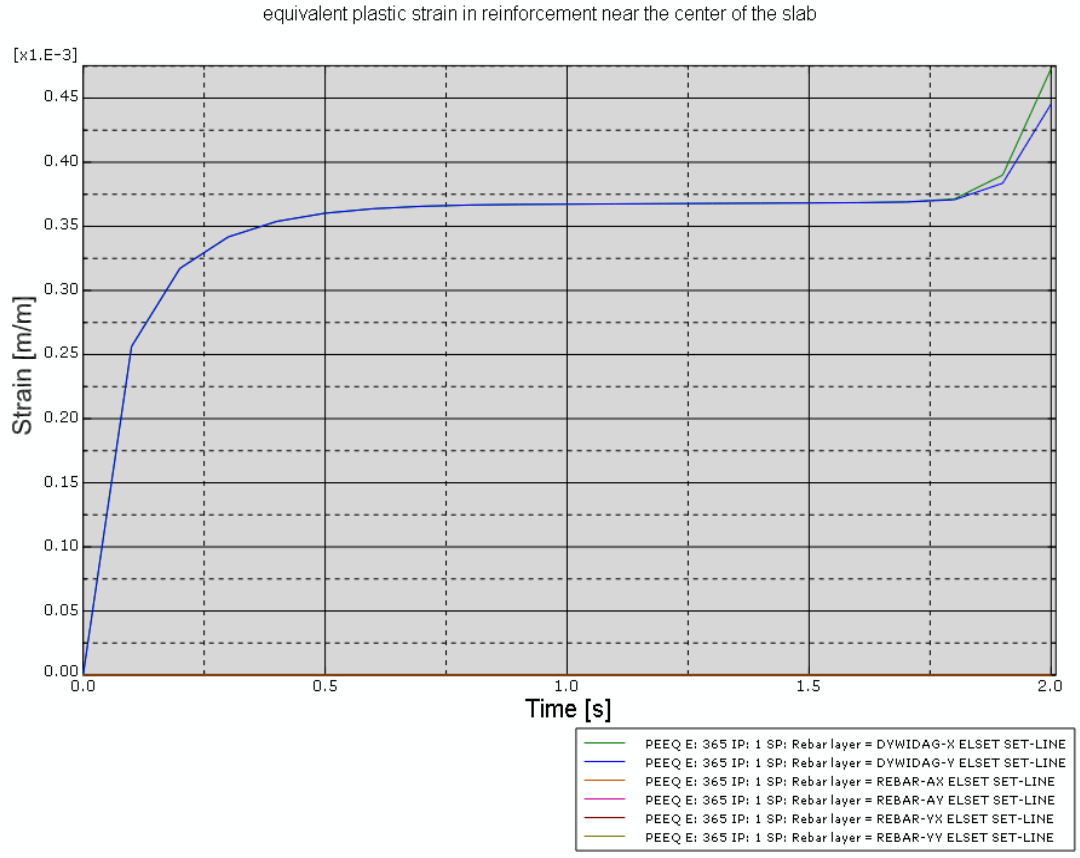

Figure 115. Equivalent plastic strain in reinforcement near the centre of the slab.

Next, a dynamic case was studied with the same shell element model using Abaqus/Explicit. A hard missile with a mass of 47 kg impacted the wall centre with a velocity of 60 m/s. The missile impact is applied as a point load to the middle node of the wall. Figure 116 shows the force time function which is a slightly modified Riera curve with a theoretically correct momentum (2820 Ns). Three different wall types are compared with each other. Either there are no Dywidag bars or if there are bars, they are stressed to 900 MPa or left unstressed.

Figure 117 shows the mid point deflection of the wall right after the impact. Also cases where Dywidags were not included (dotted line) or they were included but no stress was applied (continuous blue line) were analysed. According to this study, the Dywidag bars with significant tension (continuous magenta line) reduce the wall deflection by half. However, it should be noted that this model takes only the bending mode into account while ignoring the punching mode and the Dywidags are fully bonded although in the test they were unbonded. The Dywidags bars with no tension also reduce the bending deflection even though they initially lie in the neutral axis, since after the wall has deformed sufficiently the Dywidag bars take part of the load.

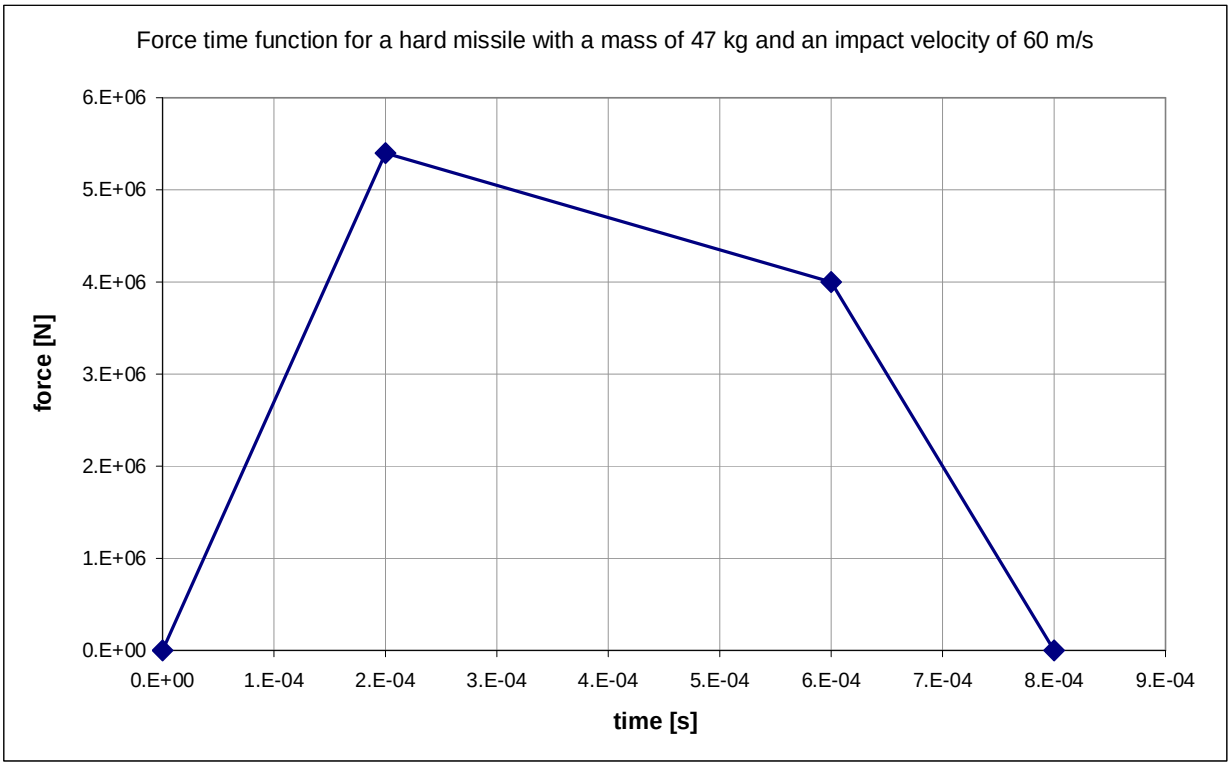

Figure 116. Force time function for a hard missile.

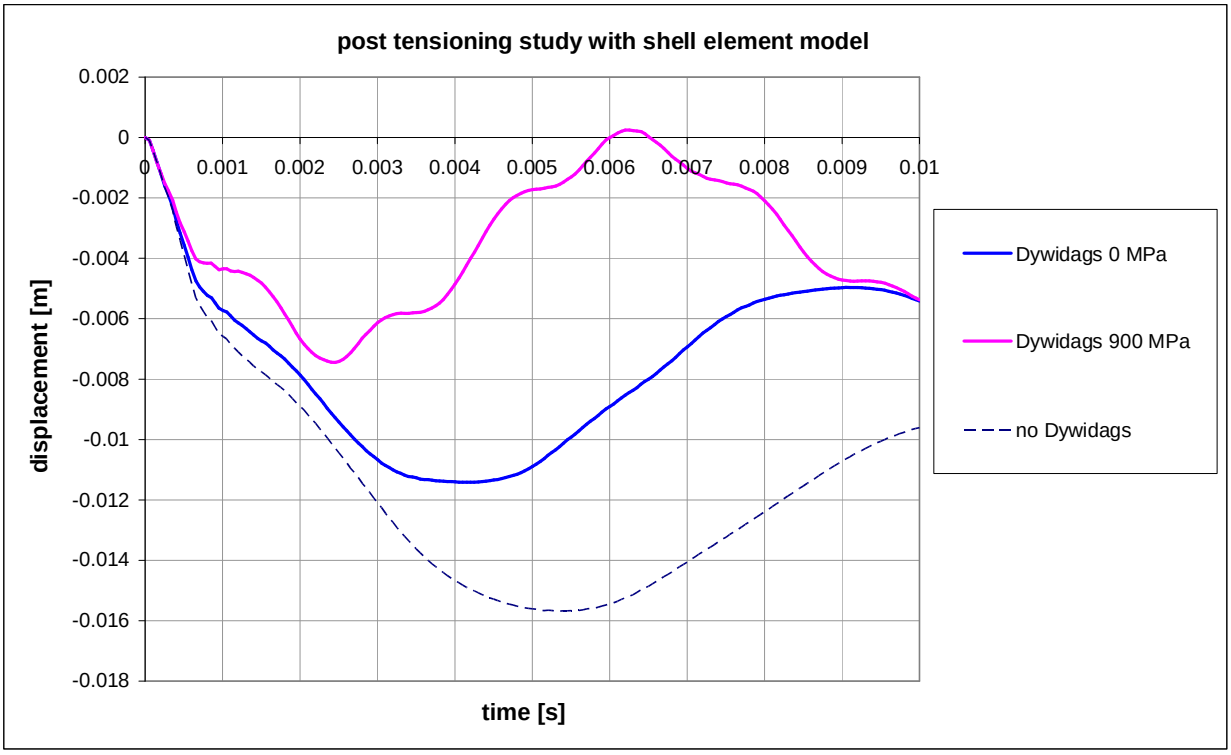

Figure 117. Centre node displacement (wall deflection)

Next, prestressing modelling was studied with a 3D solid element model. This time only one tendon was assumed. It is the lowermost tendon used in the tests located 0.24 m from the bottom edge of the wall and in the centre of the cross-section. Figure 118 shows the solid element model for prestressing study. On the left, the tendon can be seen inside the transparent wall. On the right, the deformed wall element mesh is shown (in case of an unbonded tendon) where the deformations are scaled up by a factor of 1 000 for illustrational purposes.

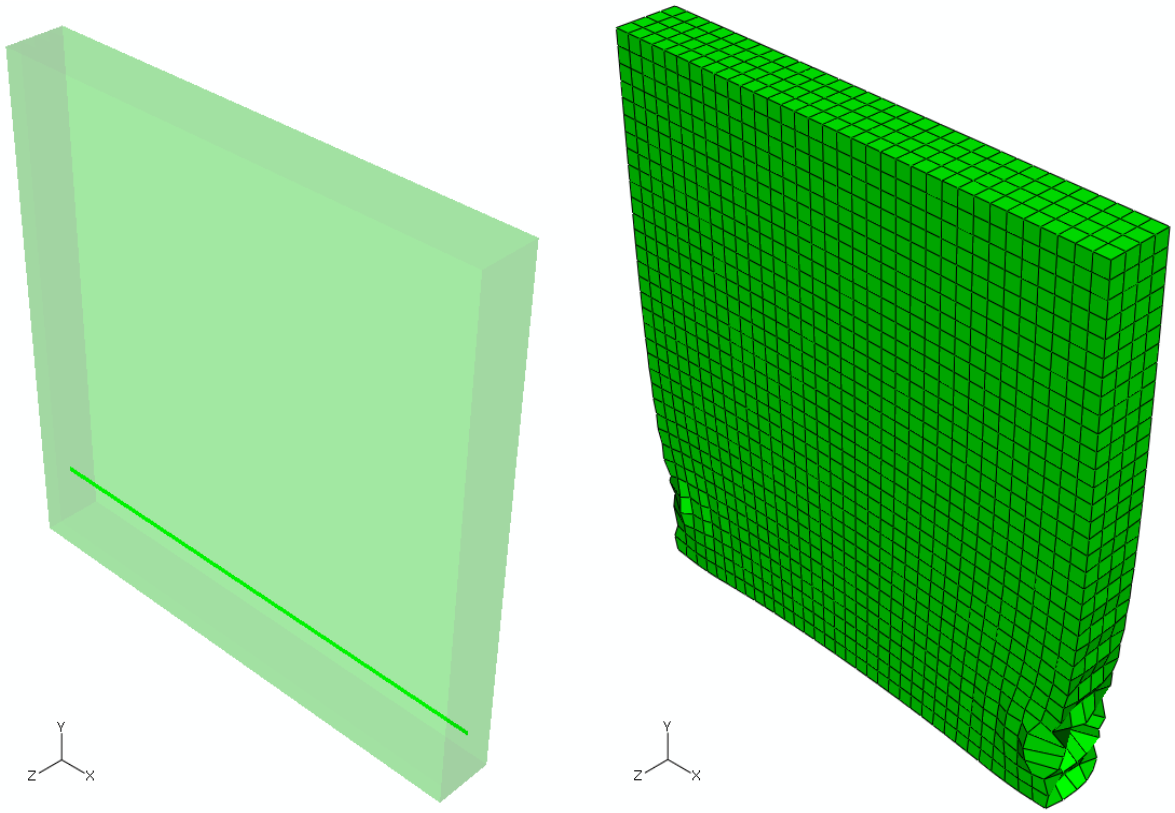

Figure 118. Solid element model for prestressing study. On the left, transparent wall and the tendon. On the right, deformed wall element mesh.

There were 4624 solid elements with 8 nodes (C3D8R) for the wall and 34 truss elements (T3D2) for the tendon. Two static cases were studied where tension in the tendon was ramped up linearly to 900 MPa. In the first case, the tendon is embedded inside the wall and is thus perfectly bonded. In the second case, it is fixed with multi-point constraints to nine concrete nodes from both ends and left otherwise free and unbonded. Figure 119 shows the tendon stress in both cases. The first case (bonded tendon) is on the left, the second case (unbonded tendon) is on the right. In the first case, the stress is approximately 800 MPa in the centre and decreases near zero at both ends. In the second case, the tendon stress is 900 MPa throughout its length. Figure 120 shows the horizontal stresses in the concrete surface. The deformations are multiplied by factor of thousand for illustrative purposes. The tendon pulls the concrete to compression between 2 MPa and 4 MPa in both cases, but in the second case there are some additional peaks of compressive stress.

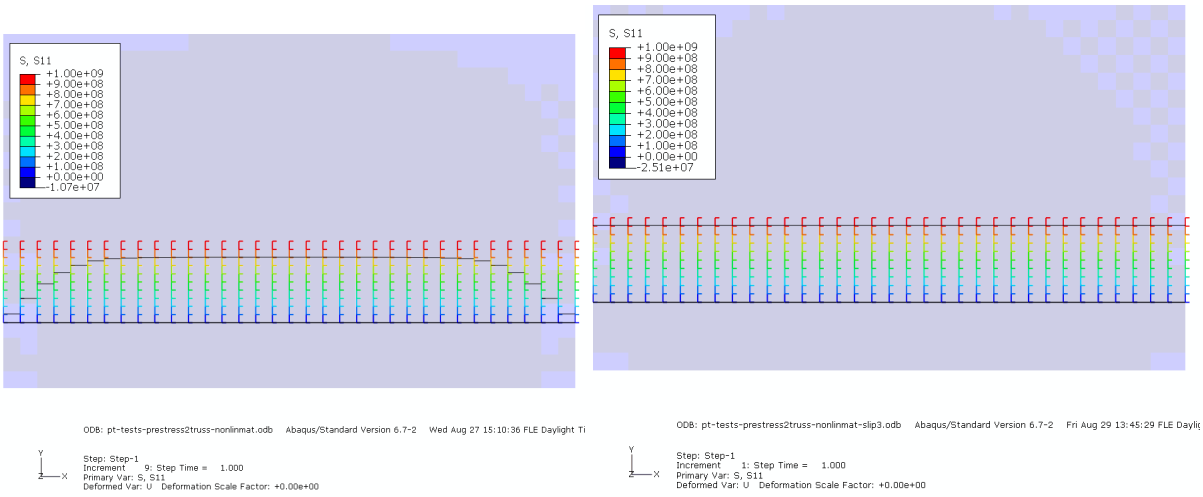

Figure 119. Tendon stress in both cases (bonded on the left, unbonded on the right).

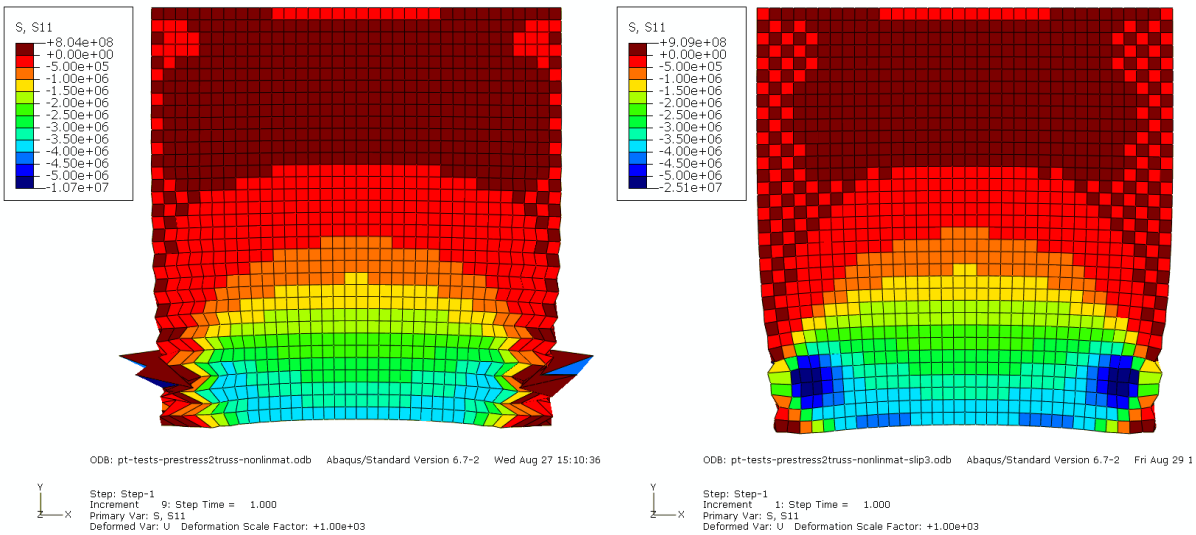

Figure 120. Horizontal concrete surface stress in both cases (bonded on the left, unbonded on the right).

6 Summary and conclusions

The IMPACT facility has been developed starting from 2003 and has reached now a mature status where well repeatable tests can be conducted and broad range of dynamic data acquired reliably. Most important measurements are the force-time function of impact (including effects of liquid, possibly contained in the missile) and for walls dynamic displacement (at selected locations) and strains in wall reinforcement. The first phase of the international test campaign has now been completed.

Simplified models that are valuable when judging the reliability of both the test results and the more extensive numerical simulations are studied. Bending or shear failure of a reinforced concrete slab subjected to a projectile impact can be very simply modelled with a two mass system (TDOF). The two mass system is, however, sensitive to the assumed angle of shear failure cone and 3D finite element solutions are needed for comparison. Experimental findings can be used in defining the shear angle for different kind of slabs. Also the determination of proper damping requires carefully conducted experiments.

Based on these studies it can be concluded that these simple four-node shell element models where the transverse nonlinear shear deformation is not considered are capable for calculating the deflection behaviour of a reinforced concrete wall loaded by a deformable missile. The simplified method and shell element model without the frame somewhat overestimated the permanent deflection. The frequency of the calculated bending vibration after impact was higher than the one recorded during the test. The model with the frame predicted similarly the vibration behaviour for the damaged wall although estimated the permanent deflection reasonably well.

Even though the impulse is slightly higher in the dry missile test, the maximum deflection is clearly smaller than the one in the wet missile test in accordance both to the measurements and calculations. According to the calculations with the shell element model the maximum strain, by a clear margin, occurred in the horizontal reinforcement in the dry missile test. This is due to the fact that the wall loaded by the deformable empty missile behaves like a wide bending beam. In tests where the water missile was used, the calculated strain values in the vertical back surface reinforcement were nearly as high as in the horizontal back surface reinforcement. This is due to the fact that the missile filled with water has a much higher maximum peak value in the load time function at least according to the Riera method.

Some preliminary calculations were carried out also using LS-DYNA code. The maximum deflection was somewhat overestimated and the permanent deflection was underestimated. However, the model was able to simulate the frequency of the global bending mode of the damaged wall reasonably well. In some LS-DYNA analyses, also the missile and its impact behaviour was included. Different breaking mechanisms, both tearing and folding, were managed to get in the simulations. The missile behaved in a similar way both in the tests and in the corresponding simulations. The contact force between the missile and the wall was close to the one given by the Riera method that has been used in the simulations without missile.

The prestressing of reinforced concrete walls and especially its numerical modelling was studied on a general level. Prestressing can be accomplished in at least three different ways and the easiest one to model is so-called bonded post-tensioned concrete, which is the descriptive term for a method of applying compression after pouring concrete and the curing process (in

situ). The bond between steel bars and concrete is an important part of the reinforced concrete mechanical system. An easy way considering the modelling is to assume that there is a perfect bond and neglect the bond slip. The slip can be modelled for instance by introducing separate relatively simple bond elements or by very sophisticated interface models based on plasticity theory.

The possibilities offered by Abaqus finite element code were studied. The Dywidag type of pre-stressing was modelled by three-dimensional shell and solid element models. Both static and dynamic cases were solved and the models behaved in a realistic way and according to theory. The bond slip was not included in the simulations. The models are ready to be improved and used for more complicated cases such as for simulations of IMPACT project tests with Dywidag prestressing.

References

Abaqus Theory Manual, Version 6.7, SIMULIA, Dassault Systemes, 2007.

ASCE, 1980. "Structural Analysis and Design of Nuclear Power Plant Facilities". ASCE 0-87262-238-X. ASCE, 1980, 571 p.

Biggs, J.M., (1964), Introduction to Structural Dynamics. McGraw Hill, 1964.

Calonius, K., Tuomala, M., Hakola, I., Saarenheimo, A., Hostikka, S., Silde, A. and Lastunen, A. IMPACT Tests: Test Facilities and Application Methods, Part 1. VTT Research Report. VTT-R-00731-08. 2008.

CEB Bulletin d'Information no. 187. 1988. Concrete Structures under Impact and Impulsive Loading.

Cervenka Consl., 2002. Atena user's manual, Part 1–7, 2000-2002. Prague: Cervenka Consl.

Diep, B. K., 2002. Non-linear analysis of externally prestressed concrete beams. Electronic Journal of Structural Engineering, 2 (2002).

DSI America (Dywidag-Systems International), 2008. Website: http://www.dsiamerica.com/

DSI UK, 2008. Website:
http://www.dywidag-systems.com/uk/products/prestressing-steel-threadbar/technical-data.html

FIB2000, 2000. Bond of reinforcement in concrete state-of-art report task group Bond models. FIB Bulletin, 2000;10.

Hallquist, J.O., (2006) LS-DYNA Theory Manual, Livermore Software Technology Corporation, March 2006.

Jendele L., Cervenka J. Finite element modelling of reinforcement with bond. Computers & Structures, Volume 84, Issue 28, November 2006, Pages 1780-1791.

Jones, N. (1989), Structural Impact. Cambridge University Press, 1989.

Jowett J. and Kinsella K. (1989), Soft missile perforation analysis of small and large scale concrete slabs. Structures under Shock and Impact, Elsevier 1989, pp.121-132, Bulson P.S. (ed.).

Kuutti, J., 2007. Design of Projectile for Impact testing. Master Thesis Helsinki University of Technology, 2007.

Lastunen, A., Hakola, I., Calonius, K., Järvinen, E. and Hyvärinen, J., 2007. Impact Test Facility. SMiRT-19 Conference. August 2007, Toronto, Canada.

LS-DYNA Keyword User's Manual, Version 970, April 2003, Livermore Software Technology Corporation.

LS-DYNA keyword user's manual, Version 971, Volume II, Material Models, Livermore Software Technology Corporation, May 2007.

Lundgren K., 1999. Three-dimensional modelling of bond in reinforced concrete. Ph.D. Thesis, Department of Civil Engineering, Chalmers University of Technology, 1999.

Nawy, Edward G., 1989. Prestressed Concrete. Prentice Hall. ISBN 0136983758.

Nilson, Arthur H., 1987. Design of Prestressed Concrete. John Wiley & Sons. ISBN 0471830720.

Riera, J.D. (1968), On the stress analysis of structures subjected to aircraft impact forces. Nuclear Engineering and Design, Vol 8 (1968) pp. 415-426.

Saarenheimo, A., Tuomala, M., Calonius, K., Lastunen, A., Hyvärinen, J. and Myllymäki, J. Numerical Studies on Impact Loaded Reinforced Concrete Walls. SMiRT-19 Conference. August 2007, Toronto, Canada.

Saarenheimo, A., Hakola, I., Kärnä, T., Hyvärinen, J. and Tuomala, M. Numerical and experimental studies on impact loaded concrete structures in Icone-14 2006 Miami (Florida, USA).

Suomen Betoniyhdistys, 2004. Betoninormit 2004, BY50.

Wang, T. and Hsu, T. 2001. Nonlinear Finite Element analysis of concrete structures using new constitutive models. Computers & Structures vol. 79, 2001, pp. 2781-2791.